



HAL
open science

Nanostructures de titanate de Baryum : modélisation, simulations numériques et étude expérimentale.

Gentien Thorner

► To cite this version:

Gentien Thorner. Nanostructures de titanate de Baryum : modélisation, simulations numériques et étude expérimentale.. Autre. Université Paris Saclay (COMUE), 2016. Français. NNT : 2016SACLC093 . tel-01427275

HAL Id: tel-01427275

<https://theses.hal.science/tel-01427275>

Submitted on 5 Jan 2017

HAL is a multi-disciplinary open access archive for the deposit and dissemination of scientific research documents, whether they are published or not. The documents may come from teaching and research institutions in France or abroad, or from public or private research centers.

L'archive ouverte pluridisciplinaire **HAL**, est destinée au dépôt et à la diffusion de documents scientifiques de niveau recherche, publiés ou non, émanant des établissements d'enseignement et de recherche français ou étrangers, des laboratoires publics ou privés.

NNT : 2016SACL093

THÈSE DE DOCTORAT
DE
L'UNIVERSITÉ PARIS-SACLAY
PRÉPARÉE À
"CENTRALESUPÉLEC"

ECOLE DOCTORALE N° (573)

Interfaces : approches interdisciplinaires, fondements, applications et innovation

Physique

Par

Monsieur Gentien Thorner

**BARIUM TITANATE NANOSTRUCTURES:
modeling, numerical simulations and experiments**

Thèse présentée et soutenue à Châtenay-Malabry, le 28 novembre 2016:

Composition du Jury :

Philippe Papet	Professeur, Université de Montpellier	Président
Laurent Bellaïche	Professeur, Université d'Arkansas	Rapporteur
Gregory Geneste	Ingénieur de Recherche, CEA	Rapporteur
Christine Bogicevic	Ingénieur de Recherche, CentraleSupélec	Examinatrice
Jean-Michel Kiat	Directeur de Recherche, CentraleSupélec	Directeur de thèse

Remerciements

À un moment relativement crucial d'une thèse, quelques pensées iraient tout d'abord vers son directeur Jean-Michel Kiat pour un soutien indéfectible pendant une période s'étalant d'un premier contact lors d'un stage de recherche en deux mille dix jusqu'à la soutenance en deux mille seize. Les rapporteurs qu'ont été le professeur Laurent Bellaïche et le docteur Grégory Geneste méritent une profonde gratitude pour avoir accepté de r  aliser ce travail au m  me titre que le professeur Philippe Papet qui a bien voulu pr  sider le jury.

Au sein du laboratoire, la talentueuse encadrante de la partie chimie Christine Bogicevic et sa collaboratrice Fabienne Karolak ont toutes deux   t   d'une aide significative. Sans vouloir pr  tendre atteindre une quelconque exhaustivit  , le directeur de l'unit   Guilhem Dezanneau m  rite un remerciement pour sa gestion du laboratoire, de m  me que le professeur Igor Kornev pour la fourniture des codes de simulations de Monte-Carlo accompagn  e de pr  cieuses recommandations quant    leur utilisation. Une mission d'enseignement relativement ambitieuse fut propos  e par l'inventif professeur Jean-Michel Gillet.

C  toyer les chercheurs de l'axe de recherche ferro  lectriques dont Brahim Dkhil, Pierre-Eymeric Janolin et Ingrid Canero permit de recevoir leurs conseils avis  s et de partager leur bonne humeur communicative. Retrouver en salle de d  tente les professeurs Michel Jouan et Pierre Becker, Nicolas Guiblin, Camille Exare et Sandrine Geiger, ainsi que Thierry Martin, Gilles Boemare et Xavier Bril   tait toujours un moment agr  able. Des clich  s de Microscopie   lectronique respectivement    Balayage et    Transmission n'auraient pu   tre pris sans la patience de Fran  oise Garnier et Paul Haghi-Ashtiani. Les t  ches administratives furent conduites aux c  t  s des tr  s efficaces Christine Vin  e-Jacqu  n et Pascale Salvini tandis que plusieurs articles furent fournis par Claire Roussel. Mention doit   tre faite de l'aide significative apport  e par Suzanne Thuron et Catherine Lhopital au niveau de l'  cole doctorale.

Impossible d'oublier tous les doctorants crois  s pendant ces ann  es pass  es au sein du laboratoire mais difficile d'en dresser une liste compl  te: que Micka  l, Sergei, Yousra, Romain, Charlotte, Anastasia, Bertrand, Charles, Fabien, Cintia, D  sir  e, Halyna, Xiaofei et Yang soient, entre autres, remerci  s pour de bons moments pass  s en commun.   tre associ      l'encadrement du parcours Centrale Recherche de Jordan fut un plaisir et permit d'avancer plus rapidement sur une mod  lisation de cubes creux.

Hors du laboratoire, je tiens    remercier Julien pour un conseil de template facilitant la r  daction.

Quelques mots ne sauraient d  crire toute la gratitude d  e    chaque membre d'une famille ayant su porter assistance chaque fois que cela semblait n  cessaire. Que m  re, p  re, grand-m  re, grand-p  re, s  ur, oncle et tante, cousin, cousine et oubli  s de cette trop courte liste en soient tous remerci  s.

Contents

Remerciements	3
1 About numerical simulations of ferroelectrics	15
1.1 Mathematical reminders	15
1.1.1 Taylor expansion	16
1.1.2 About tensors	16
1.2 Ferroelectric crystals	18
1.2.1 A history of ferroelectricity	18
1.2.2 Introduction to bulk crystals and perovskites	19
1.3 Second principles simulations of ferroelectrics	29
1.3.1 Ab initio methods	29
1.3.2 Effective Hamiltonian construction	31
1.3.3 Boundary conditions	35
1.3.4 About order parameters evidenced in ferroics numerical simulations	41
1.4 Conclusion	48
2 Syntheses of Barium Titanate nanospheres, nanocubes and nanotori	51
2.1 Syntheses and characterization	52
2.1.1 Solvothermal methods	52
2.1.2 Electron Microscopy	53
2.1.3 X-Ray diffraction	53
2.2 Synthesis steps	54
2.2.1 Precursor syntheses	54
2.2.2 Ion-exchange	56
2.3 Conclusion	63
3 Morphogenesis mechanisms	65
3.1 Nanospheres	65
3.2 Nanotori	66
3.3 Nanospheres and nanotori	71
3.4 Nanocubes	73
3.5 Conclusion	76
4 Towards more complex order parameters in inhomogeneous materials	79
4.1 Description of charge distributions	79
4.1.1 Multipolar expansion	80
4.1.2 Rearranging into sets of terms stable versus rotations	81
4.2 Electrostatic interaction in inhomogeneous background permittivity	83
4.2.1 Inhomogeneous permittivity without periodic boundary conditions	84
4.2.2 Inhomogeneous permittivity with periodic boundary conditions	85
4.3 Conclusion	86

5	Hollow nanocubes	87
5.1	General Barium Titanate simulations	88
5.1.1	First-principles derived original parameters	88
5.1.2	Monte-Carlo evolution	89
5.1.3	Hollow dot	90
5.2	Simulations under extreme boundary conditions	91
5.2.1	First-principles derived parameters	91
5.2.2	Case of a solid cube under short-circuit boundary condition	92
5.2.3	Case of a solid cube under open-circuit boundary condition	95
5.2.4	Case of a hollow cube under short-circuit boundary condition	98
5.2.5	Case of a hollow cube under open-circuit boundary condition	101
5.3	Simulations around a critical depolarizing field	103
5.3.1	Case of a solid cube	103
5.3.2	Case of hollow cubes	105
5.4	Conclusion	106
6	Nanotori	109
6.1	Considered shapes	109
6.1.1	Torus construction	110
6.1.2	Electrical boundary conditions	111
6.1.3	Local polarization representation	111
6.2	Geometry-dependent transitions	111
6.2.1	Torus having small minor to major radius ratio	112
6.2.2	Torus having close minor and major radius	114
6.2.3	Intermediate major to minor torus radius ratio	116
6.3	Beyond toroidal moment	118
6.3.1	Another charge moment	118
6.3.2	Geometry-dependent temperature behavior	120
6.3.3	Electric field cycling	122
6.4	Conclusion	124
	Conclusion and prospects	125
7	Summary in french	131
	Bibliography	137

“It is nice to know that the computer understands the problem. But I would like to understand it too.”

Eugene Wigner

À ma mère ...

General introduction

ENERGY separates animals from mankind since the latter was able to release heat by igniting fires and effectively rearranging chemical bonds of reagents into stabler products. Electricity triggered an industrial revolution due to the possibility of separating power plants from energy consumption sites. In materials, conductivity is the physical quantity that varies the most, ranging from perfect band insulators to superconductors. Interest in insulating materials storing electrical energy is at least twofold and requirements of one application could seem contradictory with those of the other and lead to different materials choice. Releasing energy rapidly without wearing out leads to materials aiming at providing better batteries provided that enough charge per unit of surface circulates at sufficiently high a voltage per unit of thickness. For this, a subclass of materials called ferroelectrics does not necessarily compete with solid electrolytes. As a matter of fact, these ferroelectrics (materials that possess a spontaneous lattice polarization reversible by an applied electric field) can indeed form capacitors but the electrical energy stored per unit volume lies several order of magnitude below that of a battery: as charge displacement exclusively comes from lattice polarization, charge carriers only move by distances that are greatly smaller than lattice size. On the other hand, electrically switching an electric or magnetic order parameter [1] between several easily distinguishable stable states through convenient excitations paves a way towards future memory devices. A preferred switching method between stable states at operating temperature requires switching few charges at as little a voltage per unit thickness as possible in order to reduce writing energy and ferroelectrics seem to be materials of choice to fulfill such a requirement. As small a footprint as possible on an integrated circuit is another aim of such a capacitor designed to function as a memory bit, which triggers an interest into nanostructures.

Pyroelectricity, also known as temperature-related buildup of electric charge, observation may be traced back to Ancient Greece. Conversely, charge variation on stressing a material, to be called latter piezoelectric properties, went unnoticed until the end of the nineteenth century. Ferroelectricity and its associated multiple stable states that can be reached through applied electric fields was evidenced in the decades after but only in exotic materials. Barium Titanate (BaTiO_3 thereafter called BTO), a ternary oxide including a transition metal and an alkaline-earth one can be produced with several atomic organizations: an amorphous form, in which atomic positions do not follow a periodic pattern was even obtained in the early eighties. BTO crystalline form was obtained earlier, in the mid-twentieth century, and has been the focus of much more attention since it has become a textbook example of mechanisms leading to ferroelectricity. Atomic positions in such a crystal belonging to a class called perovskite can be slightly altered at a very little energetic cost. An ill-defined ground state could be viewed as a reason why this material undergoes

numerous structural phase transitions including a ferroelectric one.

Overall shape of a material sometimes also interplays with its structure under stringent conditions: ferroelectricity in bulk materials was thought to vanish in particles whose dimension was as small as billionths of a meter due to the increased surface to volume ratio giving more importance to the electric depolarization field generated at the interface between a polarized material and an external medium that does not necessarily bring compensating surface charges. Ferroelectricity in cubic samples having reduced dimension may persist on a local scale but form yet-to-be-detected vertices [2] that prevent polarization from having a component perpendicular to the interface of a material with vacuum. Cubes are not necessarily the only shape of interest and this work will show that an increasingly complex topology of nanometric dots leads to a variety of local polarization patterns that are more difficult to sort and relatively hard to predict. An experimental feedback lead into considering counterintuitive geometries such as hollow cubes and even shapes that are not necessarily simply connected such as a torus. Making a hole in ferroelectric material or dealing with toric particles and studying an interplay between as-obtained shapes and local polarization vector field thus constitutes the core of this thesis. On starting from a high temperature disordered phase in the absence of external excitation, cooling leads to self-organization and appearance of simulated counterintuitive polarization patterns. Relevant quantities called order parameters have to be found to describe transitions from disordered to ordered states. Moreover, external excitations were numerically applied in order to reach additional states and order parameter reversals were observed.

After this general introduction, the first chapter will only deal with results retrieved from literature whereas next chapters will focus on elements obtained in the course of this work. A brief reminder of Taylor expansion and tensor components will be provided at the beginning of first chapter and it will be followed by an introduction to ferroelectric crystals. First chapter will then contain a description of second-principles methods that were used throughout this document to numerically predict polarization patterns. It will remind the reader about how a perovskite material structural instability in bulk is modeled in an *ab initio*-derived framework with an expression of energy as a function of distortions. Successful prediction of bulk transitions sequence will be recalled and a set of parameters will be adopted for the rest of the manuscript. Specific attention will be paid to boundary conditions and their effect on simulation results. The possibility of forming polarization vortices will be stressed and several exotic polarization patterns will be reviewed. This will be the scope of the two last chapters. To justify our interest in exotic shapes, an experimental section will come before numerical results. Second chapter will introduce a preferentially used soft chemistry technique yielding ternary oxides such as Barium Titanate : a so-called solvothermal method. Third chapter will then be dedicated to morphogenesis mechanisms and toy models that justify a variety of object shapes. A short fourth chapter will be split in two parts. It will begin with an overview of techniques that allow an accurate description of a distribution of charge. It will focus on moments of polarization that Laplace equation solving techniques often neglect, regrouping terms obtained by using the symmetry considerations of first chapter. This

scheme includes terms that complement multipolar expansion and can produce new order parameters that can help on trying to describe exotic polarization orderings. Fourth chapter will close with steps towards modeling a material with inhomogeneous permittivity. Fifth chapter will concentrate on modeling of nanometric cubes and remind that simulation results already obtained on solid nanocubes were apparently disproved by experiments. This fifth chapter will thus be dedicated to a slightly more peculiar geometry that keeps a cubic external appearance but adds a cubic hole at the center of the simulated dot. Strikingly similar features will be evidenced and a toroidal moment will be computed again as it remained the preferred order parameter. A more exotic experimentally obtained geometry will then be studied. A brief introduction to numerical approximations used to simulate nanometric tori will be provided and various results obtained on computing a so-called hypertoroidal moment will be presented in the sixth chapter. A last chapter will provide a general conclusion to this work.

As a summary, ferroelectric material exceptional shapes were experimentally obtained. Numerical simulations gave insight in spontaneous polarization organization inside similarly-shaped particles: homogeneous polarization is only the most simple order that can arise and local polarization states can be more complex in the experimentally synthesized particles.

Chapter 1

About numerical simulations of ferroelectrics

Contents

1.1 Mathematical reminders	15
1.1.1 Taylor expansion	16
1.1.2 About tensors	16
1.2 Ferroelectric crystals	18
1.2.1 A history of ferroelectricity	18
1.2.2 Introduction to bulk crystals and perovskites	19
1.3 Second principles simulations of ferroelectrics	29
1.3.1 Ab initio methods	29
1.3.2 Effective Hamiltonian construction	31
1.3.3 Boundary conditions	35
1.3.4 About order parameters evidenced in ferroics numerical simulations	41
1.4 Conclusion	48

FROM the discovery of Rochelle salt to the preparation of ferroelectric nanoparticles, microscopic understanding of polar lattice distortions in crystals has come a long way. In this chapter, a rapid preliminary will first introduce Taylor expansion and tensor invariants but the focus will then move on to a historical perspective on ferroelectricity simulation. Details about boundary conditions will then be provided and chapter will close with several exotic microscopic patterns that were observed in literature.

1.1 Mathematical reminders

The expression of a function as a series of its derivatives will be used throughout this manuscript. Moreover, the general concept of tensor and transformation laws provides a framework to deal with any physical quantity related to a coordinate system.

1.1.1 Taylor expansion

By writing $\underbrace{\partial \cdots \partial}_n f(a)$ the derivatives of a derivable function f of a single variable x at point a , its expression as a series gives equation 1.1.

$$f(x - a) = \sum_{n=0}^{\infty} \frac{(-1)^n}{n!} (x - a)^n \underbrace{\partial \cdots \partial}_n f(a) \quad (1.1)$$

Such an expression is the most simple case and subsequent uses of Taylor expansion will deal with distributions instead of functions. Moreover, even if the general expression is similar, instead of one variable, one will use triplets of variables representing spatial coordinates.

1.1.2 About tensors

In a given basis, a tensor of order n can be described as a multidimensional (of order n) array of coefficients that is equipped with a transformation law that describes the change of tensor components under a change of the set of coordinates. A particular type of basis change is rotation and the group of matrices that describe the new components of a vector as a function of the old ones in three-dimensional space is called $SO(3)$. As a result, the new components of any vector after rotation are linear combinations of the old components multiplied by the corresponding coefficients such as in equation 1.2.

$$T'_j = \sum_j R_{ij} T_j \quad (1.2)$$

In the case of a tensor that has order n higher than one the transformation law has to be applied on each of the n indexes of the tensor as in equation 1.3.

$$T'_{abc \cdots m} = \sum_{\alpha\beta\gamma \cdots \nu} R_{a\alpha} R_{b\beta} R_{c\gamma} \cdots R_{m\nu} T_{\alpha\beta\gamma \cdots \nu} \quad (1.3)$$

For any tensor order, the 3^n tensor components can be regrouped into sets of linear combinations that are stable under any operation of $SO(3)$ *i.e.* after transformation, each element of the set can be expressed as a linear combination of the others. For a tensor T that has rank one, the set is composed of the three components in equation 1.4 due to the definition of the rotation.

$$\begin{aligned} T_1 \\ T_2 \\ T_3 \end{aligned} \quad (1.4)$$

Without normalization, the set of tensor invariants for the nine components of a tensor T that has rank two is made of three parts that are reproduced from reference [3] in equations 1.5, 1.6 and 1.7.

$$T_{11} + T_{22} + T_{33} \quad (1.5)$$

$$\begin{aligned}
& T_{23} - T_{32} \\
& T_{31} - T_{13} \\
& T_{12} - T_{21}
\end{aligned} \tag{1.6}$$

$$\begin{aligned}
& T_{11} + T_{22} - 2T_{33} \\
& T_{11} - T_{22} \\
& T_{23} + T_{32} \\
& T_{31} + T_{13} \\
& T_{12} + T_{21}
\end{aligned} \tag{1.7}$$

Similarly, the set of tensor invariants for the twenty-seven components of a tensor T that has rank three is made of seven parts that are reproduced in equations 1.8, 1.9, 1.10, 1.11, 1.12, 1.13 and 1.14.

$$(T_{231} - T_{321}) + (T_{312} - T_{132}) + (T_{123} - T_{213}) \tag{1.8}$$

$$\begin{aligned}
& (T_{313} - T_{133}) - (T_{122} - T_{212}) \\
& (T_{121} - T_{211}) - (T_{233} - T_{323}) \\
& (T_{232} - T_{322}) - (T_{311} - T_{131})
\end{aligned} \tag{1.9}$$

$$\begin{aligned}
& (T_{231} - T_{321}) + (T_{312} - T_{132}) - 2(T_{123} - T_{213}) \\
& (T_{231} - T_{321}) - (T_{312} - T_{132}) \\
& (T_{313} - T_{133}) + (T_{122} - T_{212}) \\
& (T_{121} - T_{211}) + (T_{233} - T_{323}) \\
& (T_{232} - T_{322}) + (T_{311} - T_{131})
\end{aligned} \tag{1.10}$$

$$\begin{aligned}
& (T_{313} + T_{133}) + (T_{122} + T_{212}) - 2(T_{221} + T_{331}) \\
& (T_{121} + T_{211}) + (T_{233} + T_{323}) - 2(T_{112} + T_{332}) \\
& (T_{232} + T_{322}) + (T_{311} + T_{131}) - 2(T_{113} + T_{223})
\end{aligned} \tag{1.11}$$

$$\begin{aligned}
& (T_{231} + T_{321}) + (T_{312} + T_{132}) - 2(T_{123} + T_{213}) \\
& (T_{231} + T_{321}) - (T_{312} + T_{132}) \\
& (T_{313} + T_{133}) - (T_{122} + T_{212}) - 2(T_{331} - T_{221}) \\
& (T_{121} + T_{211}) - (T_{233} + T_{323}) - 2(T_{112} - T_{332}) \\
& (T_{232} + T_{322}) - (T_{311} + T_{131}) - 2(T_{223} - T_{113})
\end{aligned} \tag{1.12}$$

$$\begin{aligned}
& (T_{313} + T_{133}) + (T_{122} + T_{212}) + (T_{331} + T_{221}) + 3T_{111} \\
& (T_{121} + T_{211}) + (T_{233} + T_{323}) + (T_{112} + T_{332}) + 3T_{222} \\
& (T_{232} + T_{322}) + (T_{311} + T_{131}) + (T_{223} + T_{113}) + 3T_{333}
\end{aligned} \tag{1.13}$$

$$\begin{aligned}
& (T_{231} - T_{321}) + (T_{312} - T_{132}) - (T_{123} - T_{213}) \\
& (T_{313} + T_{133}) + (T_{122} + T_{212}) + (T_{331} + T_{221}) - 2T_{111} \\
& (T_{121} + T_{211}) + (T_{233} + T_{323}) + (T_{112} + T_{332}) - 2T_{222} \\
& (T_{232} + T_{322}) + (T_{311} + T_{131}) + (T_{223} + T_{113}) - 2T_{333} \\
& (T_{313} + T_{133}) + (T_{122} + T_{212}) + (T_{331} - T_{221}) \\
& (T_{121} + T_{211}) + (T_{233} + T_{323}) + (T_{112} - T_{332}) \\
& (T_{232} + T_{322}) + (T_{311} + T_{131}) + (T_{223} - T_{113})
\end{aligned} \tag{1.14}$$

1.2 Ferroelectric crystals

Ferroelectricity has been understood through in a process that took place over several centuries. A history of ferroelectricity will be provided first and will be followed by a reminder about crystallography and perovskites. The concept of transition will then be discussed in the framework of Landau theory.

1.2.1 A history of ferroelectricity

Even though pyroelectricity, also known as temperature-related buildup of electric charge, observation occurred in the antiquity, the name was only coined by Sir David Brewster in 1824. He did so by studying a material that was called Rochelle salt $\text{NaKC}_4\text{H}_4\text{O}_6 \cdot 8\text{H}_2\text{O}$ after it was produced for its purgative medicinal properties by Elie Seignette, an apothecary in La Rochelle, France [4]. Conversely, surface charge change that occurs on stressing a material, to be called later piezoelectric properties, went unnoticed until the end of the nineteenth century, to be fully documented in 1882 by Curie brothers. The dielectric constant measured by Pockels as a function of temperature evidenced anomalies with unusually large values in 1893. A systematic analogy between magnetic properties of ferromagnetics and dielectric properties of Rochelle salt was performed by Valasek between 1921 and 1924 and he was able to experimentally draw hysteresis cycles. As Seignette salt has 112 atoms in its unit cell, linking ferroelectricity to structural changes was not very obvious with this material and microscopic mechanisms remained unknown. Moreover, an intrinsic instability of this material against dehydration complicated experimental studies and made it very difficult to design actual devices using it.

The ferroelectric properties of a simpler crystal structure called potassium dihydrogen phosphate KH_2PO_4 and having higher stability were discovered in 1935 by Busch and Scherer. As this material and Seignette salt shared the particularity of having numerous hydrogen bonds, it was erroneously thought to be a necessary feature of a material exhibiting ferroelectricity in the several models that were built by Slater in 1941 to account for ferroelectricity.

At the same time, a new class of materials ABX_3 called perovskites was discovered. A perovskite oxide ABO_3 called Barium Titanate (BaTiO_3 thereafter called BTO) being a ternary oxide

including a transition metal and an alkaline-earth one received particular attention due to it being a textbook example of mechanisms leading to ferroelectricity. Even though a non-ferroelectric amorphous form was also obtained in the early eighties, the crystalline form of BTO under study was a ferroelectric that for the first time had only 5 atoms per unit cells with a simple structure, no hydrogen bonds and no piezoelectric properties in the high temperature phase.

1.2.2 Introduction to bulk crystals and perovskites

Crystal bonding types

Among solid materials, crystals of different types exist depending on the structural arrangement of the nuclei and the type of bonds between them. Crystallization spontaneously gives rise to this state of matter as a means of striking a balance between attractive forces that exert on the nuclei and short-range repulsion due to their core electronic clouds. The following four types of crystals are known to exist.

Molecular crystals Like Rochelle salt, the building blocks of these solids are charge-neutral molecules that interact through Van der Waals forces. Depending on whether these molecules are polar or not, they respectively interact with each other through Keesom or London forces. As this interaction is weak, molecular crystals usually have very low melting points and are often unstable at room temperature. Moreover, their electrical conductivity is generally very low.

Metallic crystals Most solids made of a single element located below the Bore-Polonium diagonal of the periodic table are known as metals. In such materials, the most energetic valence electrons are shared between all the nuclei of the lattice, immersing a uniformly positively charged lattice in a negatively charged electron cloud. Sharing of electrons makes very high values of conductivity possible and the energy gained in the process leads to solids having high melting points.

Covalent crystals Solids composed of elements that have very comparable electronegativities such as quartz, that contains Silicon and Oxygen, tend to form structures inside which the most energetic valence electrons establish bonds between neighboring atoms. The direction of these bonds dictates the spatial relative positioning of the nuclei and resulting crystal structures can be complex, as in the case of diamond. Due to the strength of covalent bonding, melting temperature of covalent crystals tend to be very high. Moreover, as it was stated that the electrons are not delocalized through the entire crystal, conductivity tends to be low.

Ionic crystals In the limiting case in which an element constituting a crystal has much larger electronegativity than another, it is as if total electron transfer had occurred and the resulting solid can be treated as being made of ions. This results into a strong Coulombic interaction leading to close packed structures that melts at high temperatures. Electrons remain strongly pinned to the

ions so conductivity is in general low. Examples of such ionic crystals include perovskites such as BTO.

Yet, the distinction between covalent and ionic crystals has rather to be viewed as a continuum: the more the electronegativities are different, the more ionic is the binding between atoms. The class of crystals we will study can also be considered as an intermediate between ionic and covalent crystals.

Crystal structure types

From a geometrical point of view, a crystal can be defined as a periodic (except for quasi-crystals) spatial arrangement of atoms constituting a solid and we will focus on three-dimensional ones. As a consequence, the resulting construct has translational symmetry and contains a minimum pattern called primitive cell that can generate the entire solid through translations along any multiples of the basis vectors (the resulting set of point coordinates being called a lattice).

Nuclei coordinates in the primitive cell are transformed by any change of basis (one example being those induced by a rotation such as described in equation 1.2). However, among all the possible operations that keep distances constant (called isometries) and leave at least one point fixed (the origin), only a subset leave the primitive cell invariant by giving to any nuclei in the cell the coordinates of a similar nuclei. Due to the definition of this subset, combination of two of these operations from this subset will also leave the primitive cell invariant and preserve the origin. As there is an identity operation that consists of leaving all nuclei position unchanged, these operations form a group and can be classified as such. Apart from identity, there are four possible types of symmetry elements in such a group: reflection, rotation, inversion and rotoinversion.

There is an infinity of groups constituted of such elements. However, for the entire crystal, any translation operation between points of the lattice does not preserve the origin but also belongs to the group of symmetry elements that leave the global crystal structure invariant. The fact that the resulting combination of punctual symmetry operations and translations must also be a group imposes a crystallographic restriction to the allowed point groups for the primitive cell of a crystal. Only axes that have order 1,2,3,4 or 6 are possible and the elements of the punctual symmetry group of the primitive cell must thus be one among only 32 possible ones, that can be sorted into seven crystal families. The constraint of paving the entire space with a lattice whose points are linear combinations of the basis vectors only allows for fourteen types of lattices, that can be sorted into the same seven crystal families. These Bravais lattices that have characteristic lengths a, b, c and characteristic angles α, β, γ , are depicted in figure 1.1 in which, for convenience, some of these Bravais lattices contain several lattice points and are thus depicted by unit cells that can be several times larger than the primitive cell. On combining translations with rotations and mirror planes, it appears that a crystal structure can be invariant under combinations of operations that leave no point in space invariant called screw axes or glide planes. As a result, the total number of possible crystallographic space groups is 230 [5].

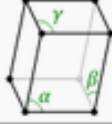
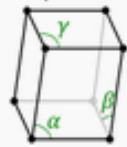
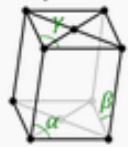
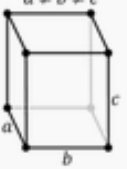
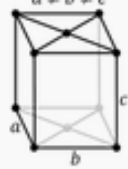
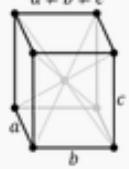
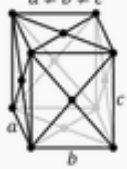
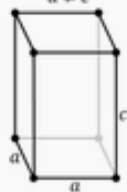
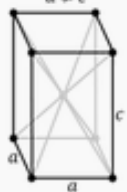
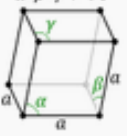
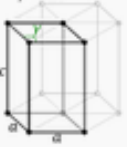
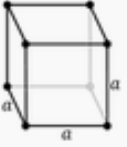
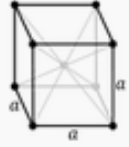
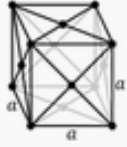
		Lattice types				
		P	Base	Base	I	F
Lattice systems	Triclinic	aP $\alpha, \beta, \gamma \neq 90^\circ$ 				
	Monoclinic	mP $\beta \neq 90^\circ$ $\alpha, \gamma = 90^\circ$ 		mC $\beta \neq 90^\circ$ $\alpha, \gamma = 90^\circ$ 		
	Orthorhombic	oP $a \neq b \neq c$ 	oC $a \neq b \neq c$ 	ol $a \neq b \neq c$ 	oF $a \neq b \neq c$ 	
	Tetragonal	tP $a \neq c$ 		tI $a \neq c$ 		
	Rhombohedral	hR or rP $\alpha = \beta = \gamma \neq 90^\circ$ 				
	Hexagonal	hP $\gamma = 120^\circ$ 				
	Cubic	cP (pcc) 		cI (bcc) 		cF (fcc) 

FIGURE 1.1: Fourteen types of Bravais lattice.

Properties related to ionic polarization can be determined by which of the thirty-two point groups of symmetry the primitive cell belongs to. Eleven groups possess an inversion symmetry and among the remaining twenty-one, only twenty are piezoelectric. Among these twenty groups containing piezoelectric materials, ten can also allow pyroelectricity and ferroelectrics materials are found among those ten groups.

About perovskite structure

Crystalline perovskite oxides having overall chemical formula ABO_3 were named after Russian mineralogist Lev Perovski; the name was originally attributed to the first material of this class to be discovered in 1839, which was Calcium Titanate $CaTiO_3$. It was then generalized to any range of possible A and B cations, provided that the crystal arrangement remained the same. The most symmetrical cubic structure is displayed in the left part of figure 1.2. It is made of a lattice of oxygen anions forming octahedra the center of which is the site of cation B. Sites in between oxygen octahedra are called cuboctahedra and host the A cation. The point group symmetry of

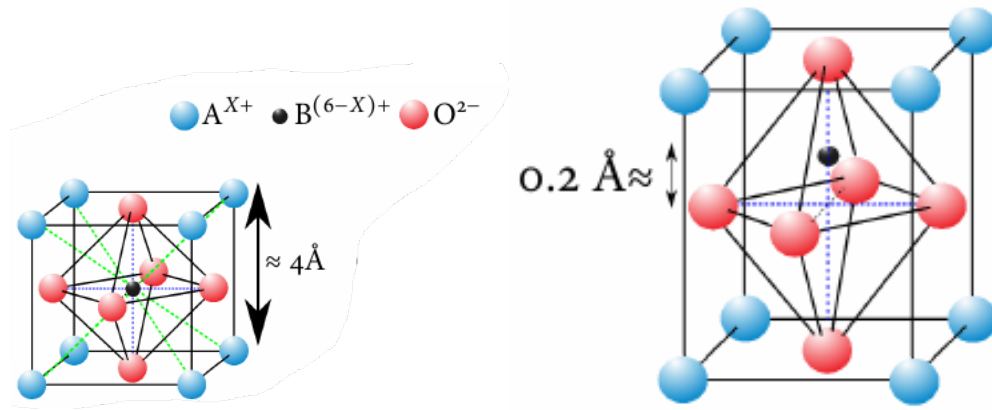


FIGURE 1.2: High temperature cubic structure of a perovskite (left) and distorted cubic structure of a perovskite leading to a tetragonal state (right).

this primitive cell is octahedral and they are evenly spaced on a primitive Bravais cubic lattice. As a result, space group of this structure is $Pm\bar{3}m$. Computing a so-called Goldschmidt tolerance factor with A, B and O respective ionic radii rad_A , rad_B and rad_O is equivalent to assuming that ions resemble hard spheres that are closely packed for a unitary value of equation 1.15.

$$\frac{rad_A + rad_O}{\sqrt{2}(rad_B + rad_O)} \quad (1.15)$$

BTO value of this factor being smaller than one, structural distortions at low temperatures and a non-cubic ground state is expected: atomic positions in such a crystal can be slightly altered at a very little energetic cost. This ill-defined ground state represents a reason why this material undergoes numerous structural phase transitions including a ferroelectric one. The various distortions around this high temperature highly symmetrical state leads to Bravais lattice changes

from a crystal family to another as well as point group changes. The sequence of ferroelectric phase transitions that will then be described including relative motion of central cation and elongation represents only one class of all possible distortions, others including rotation of oxygen octahedra and Jahn-Teller distortion of these octahedra. Transition from a titanium-centered crystalline unit cell to one of six off-centered possibilities gives rise to a microscopic dipole moment for each cell, as the barycenter of positive charges no longer corresponds with the center of oxygen anions octahedra that is represented in the right part of figure 1.2. The point symmetry group becomes ditetragonal pyramidal, a subgroup of octahedral, and the Bravais lattice becomes primitive tetragonal, leading to classification of this space group as $P4mm$. Spontaneous polarization is along one of the six equivalent $[100]$ directions.

Experimental observation of bulk BTO structure on further cooling from a tetragonal state evidenced two other structural phase transitions corresponding to the onset of a distortion in a direction perpendicular to existing crystal structure change. Experimentally detected transition temperatures and obtained primitive cell shapes are reported in figure 1.3. During a second tran-

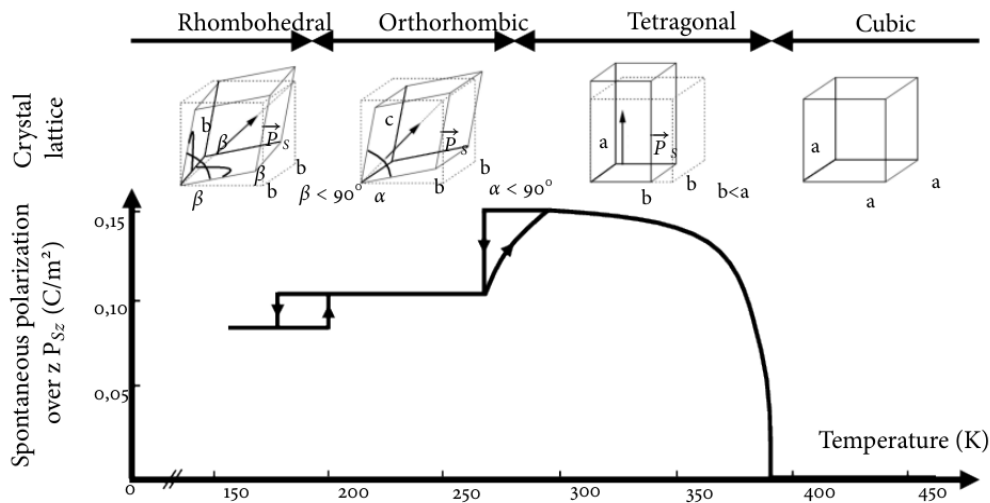


FIGURE 1.3: BTO sequence of phase transitions on cooling starting from a high temperature cubic state.

sition from the tetragonal state, Bravais lattice becomes primitive orthorhombic with point space group orthorhombic-pyramidal: $Amm2$. Polarization is then along one of the twelve equivalent $[110]$ direction. Last transition yields a primitive rhombohedral Bravais lattice and ditrigonal-pyramidal space group written: $R3m$. Polarization then aligns on one of the eight equivalent $[111]$ directions.

Properties of ferroelectric bulk

An ideal planar capacitor made of a perfectly insulating BTO bulk slab having thickness d along unit vector \hat{e}_z that could be thought of as being sandwiched between electrodes having surface S leads to a voltage drop U and lets a charge Q flow through it. Corresponding electric field intensity

E and displacement magnitude D along $\hat{\mathbf{e}}_z$ respectively come from equation 1.16 and 1.17.

$$E = \frac{U}{d} \quad (1.16)$$

$$D = \frac{Q}{S} \quad (1.17)$$

This electric displacement is made of two contributions, one that is related to electric field through the dielectric constant of vacuum representing the contribution of external free charges and a polarization one representing the contribution of bound charges inside the dielectric, as stated in equation 1.18.

$$D = \varepsilon_0 E + P \quad (1.18)$$

It follows that $D = \varepsilon_0 E$ for a slab of vacuum and, in an attempt to write a similar relation between electric field and electric displacement in dielectric media, one defines relative permittivity and susceptibility in equation 1.19.

$$\varepsilon_r = \frac{1}{\varepsilon_0} \frac{dD}{dE}_{E=0} = 1 + \frac{1}{\varepsilon_0} \frac{dP}{dE}_{E=0} = 1 + \chi_r \quad (1.19)$$

After considering the case of a mostly linear material whose electric displacement is triggered by an external electric field $D \approx \varepsilon_r E$, one can now focus on the case of a slab of material having a stable spontaneous polarization P_s . There are two limiting cases: metal plates can be shorted and thus cancel any electric field E. Equation 1.18 leads to $D=P_s$. On the other hand, if no free charges are allowed to flow from one plate to the other, which is called open-circuit boundary conditions, there cannot be any electric displacement D. Equation 1.18 gives a value of the electric field that then builds up and is called depolarization field $E_{dep} = -\frac{P_s}{\varepsilon_0}$. From a microscopic point of view, each dipole in the medium has dipole moment proportional to the local field it feels and this defines a coefficient called polarizability α . By computing the electric field in a sphere located inside a homogeneously polarized medium, the local field can be approximated by an expression called Lorentz field $E_{local} = E + \frac{P}{3\varepsilon_0}$. By calling N the number of dipoles per unit volume and assuming they all have the same polarizability, one can write the Clausius-Mossotti equation 1.20.

$$\frac{\varepsilon_r - 1}{\varepsilon_r + 2} = \frac{1}{3\varepsilon_0} N \alpha \quad (1.20)$$

For $N\alpha \approx 3\varepsilon_0$, there is a divergence of relative permittivity called the polarization catastrophe: even in the absence of electric field, a polarization can arise. The cubic structure at very high temperature gives rise to a linear electrical behavior as shown in the left part of figure 1.4. Cooling gives rise to higher permittivities at low electric fields and appearance of dielectric saturations depicted in the middle of figure 1.4. Further cooling then leads to a maximum of dielectric permittivity at low field shown in red in the right part of figure 1.4 at an equivalent of a Curie transition temperature in ferromagnets. The electrical behavior below a transition from cubic to ferroelectric

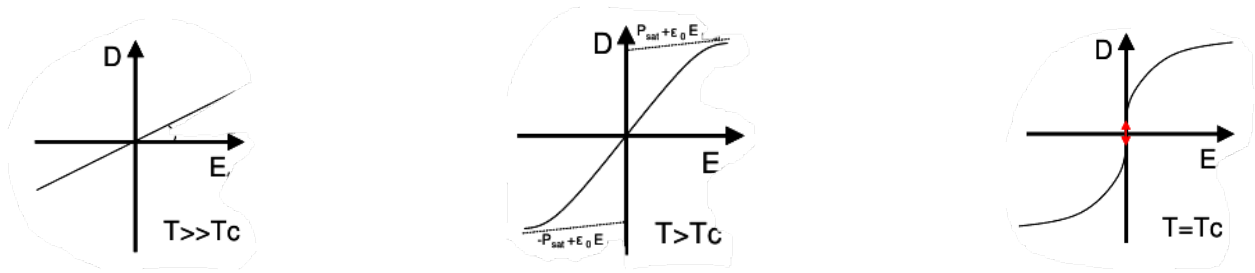


FIGURE 1.4: Typical ferroelectric material dielectric response at very high (left), moderate (middle) and Curie temperatures in paraelectric phase.

phase becomes hysteretic. New quantities such as spontaneous remnant polarization under an absence of externally applied electric field P_r arise. The coercive electric field E_c required to reverse such a polarization is lower than theoretically expected for bulk material (*cf.* dotted lines in figure 1.5) due to nucleation and growth of domains taking place instead of homogeneous switching.

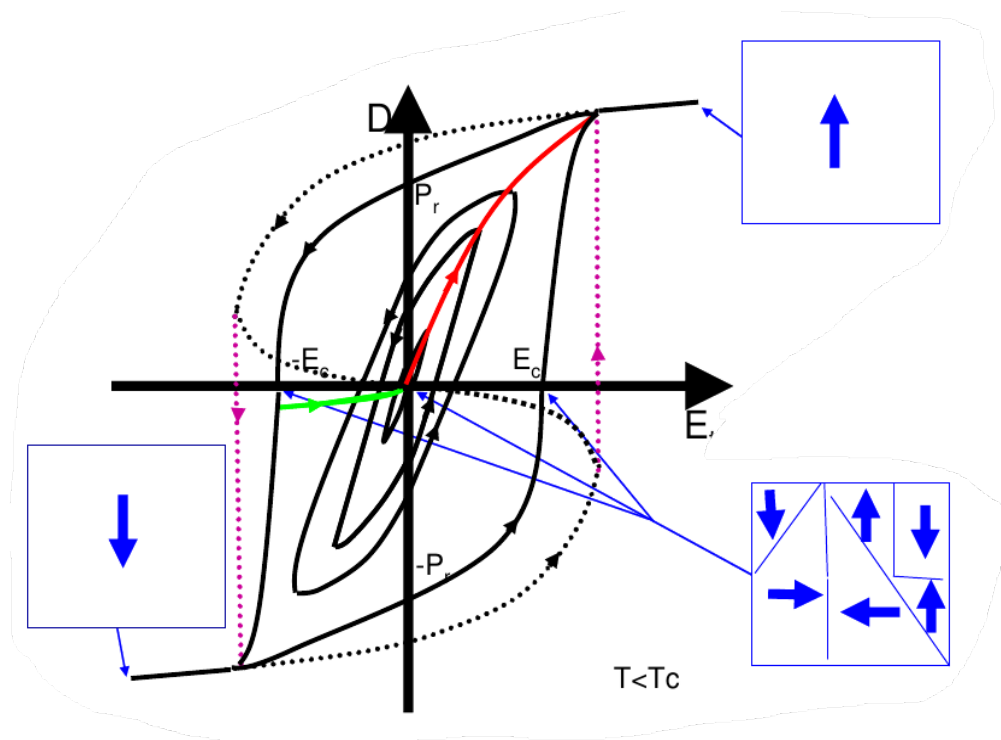


FIGURE 1.5: Below transition temperature from cubic to ferroelectric tetragonal state in bulk, more complex dielectric response exhibiting hysteretic behavior.

About the description of phase transitions with free energy

Very near the temperature of a structural change that leads to a lowering of symmetry, a convenient framework to describe the contribution to total energy that destabilizes the highly symmetric phase was designed by Lev Landau in 1937. It assumes that this free energy can be expressed as a polynomial of an order parameter. This quantity usually becomes finite at temperatures below

that of the transition so that the thermodynamically stable phase is no longer the most symmetric one. The polynomial itself can be viewed as a Taylor expansion that is valid only for very small values of the order parameter, that has several coefficients required to be null by symmetry and others that can be fitted on experimental data. Landau theory is a phenomenological theory and, as such, it will never predict a phase transition temperature in a system without experimental input as a first-principles-derived method can do it: Landau theory can be viewed as a conceptual intermediary between microscopic models and macroscopic observations. As the concept of symmetry breaking, this theory is very general. One of its prediction is the value of a critical exponent in the inverse power law of distance to critical temperature for some response functions, and similar values have been reported in various physical systems.

At thermal equilibrium, the most stable configuration is not the one that minimizes energy U but the one that minimizes the free energy F of equation 1.21.

$$F = U - TS \quad (1.21)$$

In equation 1.21, U stands for energy, T for temperature and S for entropy. First application of Landau theory in ferroelectrics is due to Devonshire and consists of an expansion of the even terms of polarization order parameter up to sixth power. The unidimensionnal case then gives equation 1.22, in which E stands for electric field and A , B and C are experimentally determined parameters.

$$F = \frac{A}{2}(T - T_0)P^2 + \frac{B}{4}P^4 + \frac{C}{6}P^6 - EP \quad (1.22)$$

Minimizing this free energy with respect to the polarization order parameter cancels its derivative with regard to P and leads to equation 1.23.

$$E = A(T - T_0)P + BP^3 + CP^5 \quad (1.23)$$

This equation allows computation of the counterintuitive hysteresis curves in dotted lines in figure 1.5. The dielectric susceptibility then writes as in equation 1.24 and exhibits an anomaly and follows a Curie law corresponding to proportionality to the inverse of distance to transition temperature.

$$\chi = \frac{1}{\varepsilon_0 \left(\frac{dE}{dP}\right)_{P=0}} \propto \frac{1}{T - T_0} \quad (1.24)$$

If coefficient B is positive, the transition is said to be of second order and its main features are depicted in figure 1.6 In the absence of an externally applied electric field, the expression of spontaneous polarization is reproduced in equation 1.25.

$$P = \sqrt{\frac{A}{B}(T_0 - T)} \quad (1.25)$$

In the case of negative B , the transition occurs with significant differences. A thermal hysteresis appears so that the transition occurs below T_0 on cooling and above T_0 on heating. Moreover,

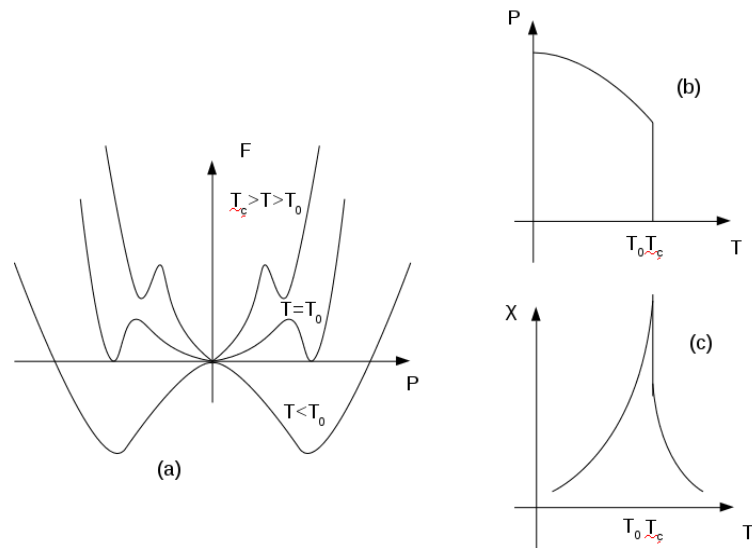


FIGURE 1.6: Free energy (a) next to order parameter (b) and susceptibility evolution as a function of temperature for a second order phase transition.

the order parameter and the susceptibility undergo a discontinuity at the transition. The general features of a first order phase transition are reproduced in figure 1.7. Landau theory considers

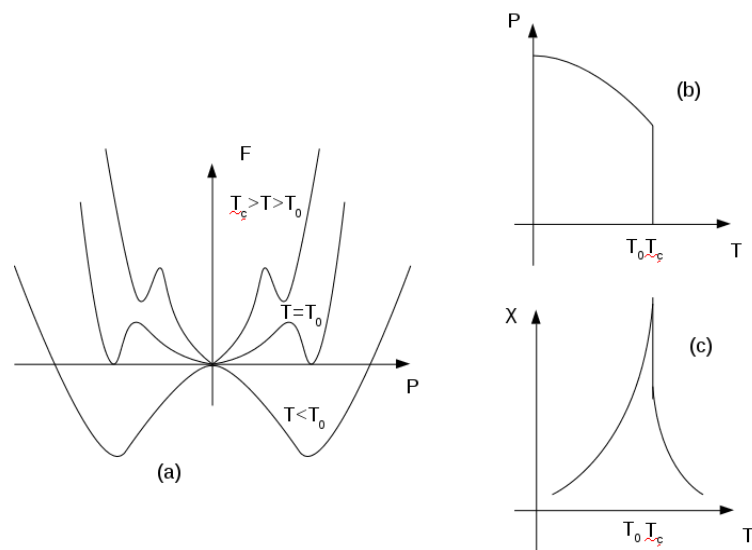


FIGURE 1.7: Free energy (a) next to order parameter (b) and susceptibility evolution as a function of temperature for a second order phase transition.

the material as single-crystalline and homogeneously polarized. Other theories, called Landau-Ginzburg, can include a spatially varying order parameter and an energy penalty corresponding to the square of the gradient. By rewriting the free energy with three directions for the order parameter and by including the strain degrees of freedom, not only the paraelectric to ferroelectric

transition but most features of the entire sequence of phase transitions (including other permittivity peaks during subsequent phase transitions to orthorhombic then rhombohedral phases as depicted in figure 1.3) could be reproduced on minimizing the free energy of equation 1.26 [6] that has coefficients fitted on experimentally measured transition temperatures.

$$\begin{aligned}
f_{LD}(\vec{P}, T) = & \alpha_0(T - T_c) (P_x^2 + P_y^2 + P_z^2) + \alpha_{11} (P_x^4 + P_y^4 + P_z^4) + \alpha_{12} (P_x^2 P_y^2 + P_y^2 P_z^2 + P_x^2 P_z^2) \\
& + \alpha_{111} (P_x^6 + P_y^6 + P_z^6) + \alpha_{112} [P_x^4 (P_y^2 + P_z^2) + P_y^4 (P_x^2 + P_z^2) + P_z^4 (P_x^2 + P_y^2)] \\
& + \alpha_{123} P_x^2 P_y^2 P_z^2 + \alpha_{1111} (P_x^8 + P_y^8 + P_z^8) \\
& + \alpha_{1112} [P_x^6 (P_y^2 + P_z^2) + P_y^6 (P_x^2 + P_z^2) + P_z^6 (P_x^2 + P_y^2)] \\
& + \alpha_{1122} (P_x^4 P_y^4 + P_y^4 P_z^4 + P_x^4 P_z^4) \\
& + \alpha_{1123} (P_x^4 P_y^2 P_z^2 + P_y^4 P_x^2 P_z^2 + P_z^4 P_x^2 P_y^2) \\
& - \frac{S_{11}}{2} (\sigma_1^2 + \sigma_2^2 + \sigma_3^2) - S_{12} (\sigma_1 \sigma_2 + \sigma_2 \sigma_3 + \sigma_1 \sigma_3) \\
& - \frac{S_{44}}{2} (\sigma_4^2 + \sigma_5^2 + \sigma_6^2) - Q_{11} (\sigma_1 P_x^2 + \sigma_2 P_y^2 + \sigma_3 P_z^2) \\
& - Q_{12} [\sigma_1 (P_y^2 + P_z^2) + \sigma_2 (P_x^2 + P_z^2) + \sigma_3 (P_x^2 + P_y^2)] \\
& - Q_{44} (P_2 P_3 \sigma_4 + P_1 P_3 \sigma_5 + P_2 P_1 \sigma_6)
\end{aligned} \tag{1.26}$$

Most of the work consisting of predicting material responses in terms of lattice constant, electric polarization, latent heat and various electroelastic susceptibilities under variations of electric field, stress and temperature can then be performed through minimizations.

Another distinction can be made depending on the microscopic mechanisms underlying the transition from a nonpolar high temperature state to a polar low-temperature one. If the establishment of a polarization involves the creation of dipoles through displacement of an ionic sublattice with regard to the rest of the crystal and if these dipoles vanish in the nonpolar configuration, the transition is called displacive. Another type of transition in which dipoles are still present in the nonpolar phase but global polarization disappears due to random orientation of these dipoles is called an order-disorder transition. In figure 1.8, the order-disorder nonpolar phase is shown on the left, the displacive nonpolar phase is shown in the middle and the polar phase is shown on the right. Yet, as Landau theory remains a phenomenological one, a complete framework en-

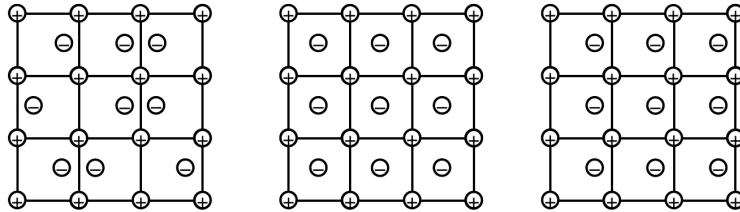


FIGURE 1.8: Order-disorder high (left) and low (middle) temperature configurations. Right is the high-temperature configuration for a displacive transition

abling computation of properties with as little experimental input as possible remained more or less missing.

1.3 Second principles simulations of ferroelectrics

Understanding of physical mechanisms enabling structural phase transitions on cooling ferroelectric perovskites tremendously benefited from studies performed in the late nineties by Vanderbilt *et al.* [7]. Ab initio values of polarization were obtained by avoiding computation of ill-defined quantities and an expansion of energy as a function of relevant atomic position degrees of freedom enabled construction of a so-called effective Hamiltonian. First principles techniques involved in computation of parameters will be presented first. A presentation of degrees of freedom and associated energy terms contained in effective Hamiltonian will be given afterwards. The role of boundary conditions will then be stressed. Section will conclude with a review of literature about exotic ordering of individual dipole moments.

1.3.1 Ab initio methods

As little experimental input as possible mean numerical simulations that only require chemical formula and atomic numbers of involved elements. Quantum-mechanical nature of electrons involved in chemical bonds between ionic constituents of a crystal imposes a scheme of simulation that properly deals with associated degrees of freedom. Density functional theory is a quantum computational method that allows an in principle exact study of electronic structure. It is among the most used computational methods in condensed matter physics and quantum chemistry thanks to its ability to describe systems containing a few atoms to several hundreds of them.

A many-body problem

Considering N electrons and an associated number of nuclei leads to a very hardly tractable interacting particles problem. A major simplification emerges from a quite large difference in mass between electrons and nuclei. Born-Oppenheimer approximation consists of decoupling electronic and atomic motions. A purely electronic problem then has to be solved at fixed atomic positions. Dealing directly with complex electronic wavefunctions requires manipulation of quantities that depend on a tensor product of as many three-dimensional spaces as there are electrons in so-called Hartree-Fock methods. Even though Pauli principle of wavefunction antisymmetry under indistinguishable electrons exchange can readily be enforced by computing Slater determinants, determination of electronic ground state energies and derived properties vastly gain at merely dealing with functionals of a quantity that is defined in a three-dimensional space *i.e.* electron density [8]. In other terms, computations in classical Hartree-Fock electronic structure methods are built upon a multielectronic wavefunction depending on $3N$ variables. On the contrary, electronic density only depends on three variables and is a quantity that can be more easily dealt with mathematically and conceptually. The difficulty lies in reformulating a quantum N -body problem into a one-body problem that has electronic density as a parameter, the main idea of DFT being that any average value of an observable such as energy only depends on the sole electronic density of the fundamental state. Yet, actually expressing a Hamiltonian keeps proving challenging : it

includes a kinetic energy term, an electrostatic energy of repelling nuclei and an electron-electron interaction term.

Coping with interacting electrons

The Kohn-Sham Ansatz [9] represents a common way of dealing with a fictitious system of non-interacting electrons in an effective potential that gives the same value of total energy as that of interacting electrons in the real potential [10]. Such a transformation introduces an effective potential that cannot be expressed without electron density and thus requires self-consistent solving methods. It is however necessary since the kinetic energy of an interacting electron gas is unknown whereas that of noninteracting electrons in a potential can be computed. Atomic positions being written as \mathbf{R}_κ and electronic wavefunctions ψ_k , total energy can be split as in equation 1.27.

$$E_{\text{total}}(\mathbf{R}_\kappa, \psi_k) = E_{\text{ion-ion}}(\mathbf{R}_\kappa) + E_{\text{ion-electron}}(\mathbf{R}_\kappa, \psi_k) \quad (1.27)$$

Ionic-ionic electrostatic interactions is computed by summing Coulombic interaction potentials. Ionic-electronic term is computed by summing eigenvalues obtained through solving Schrödinger-like Kohn-Sham equations for noninteracting electron wavefunctions with a kinetic energy term and an effective external Sham potential that comprises three terms. First term is an external potential created by nuclei, secondly comes a Hartree term representing a classical Coulomb interaction energy between a density of charge created by electrons and an electron and third term is an exchange-correlation term regrouping all the non-classical part of electron-electron interaction 1.28. Kohn-Sham equations are solved by fictitious orbitals whose square modulus add into the original system electron density

$$\left\{ \begin{array}{l} n(\mathbf{r}) = \sum_k \psi_k^*(\mathbf{r}) \psi_k(\mathbf{r}) \\ \left(\nabla^2 + v_{\text{ext}}(\mathbf{r}) + \frac{1}{2} \int \frac{n(\mathbf{r}')}{|\mathbf{r}-\mathbf{r}'|} d\mathbf{r}' + \frac{\delta E_{\text{XC}}[n(\mathbf{r})]}{\delta n(\mathbf{r})} \right) \psi_k(\mathbf{r}) = \epsilon_k \psi_k(\mathbf{r}) \\ E_{\text{ion-electron}}(\mathbf{R}_\kappa, \psi_k) = \sum_k \epsilon_k \end{array} \right. \quad (1.28)$$

An approximation is required to derive an expression of exchange-correlation density functional, that was left unknown in the derivation. As this exchange-correlation density functional depends on the resulting density, solving methods have to be self-consistent. A common development is the so-called Local Density Approximation (LDA) that assumes exchange-correlation energy can be computed as a function, rather than a functional, of density.

Energy differentiation

Computation of total energy through minimizations of an electronic contribution provides information about a large range of properties. Forces exerted on atoms can be computed as derivatives with regard to displacements and a ground state structure at zero temperature cancels all of them.

Quantities that can be expressed as energy derivatives are obtained after computation of energy differences between configurations on applying a perturbation.

1.3.2 Effective Hamiltonian construction

First principles methods provide a convenient way to compute any property of a given material with as little experimental input as possible. As it is a method describing a ground state, finite temperature behavior does not naturally emerge from it. Describing structural complexity and a sequence of phase transitions taking place in perovskites requires another approach. A first part presents a reformulation of this problem, second and third part deal with a separate treatment of short range and long-range interaction between distorted cubic unit cells of the lattice. Last part deals with actually extracting physical properties at a finite temperature from knowledge of the Hamiltonian of the system.

Energy expansion

The highly symmetrical reference state of a perovskite could be taken as cubic.

Phonon local modes as degrees of freedom Atomic displacements with regard to a cubic phase mainly come from two phonon branches that lead to six degrees of freedom per site. A five atom cell yields a total of fifteen degrees of freedom. Only dealing with modes represented in figure 1.9 provides a quite convenient representation of atomic displacements leading to structural phase transitions.

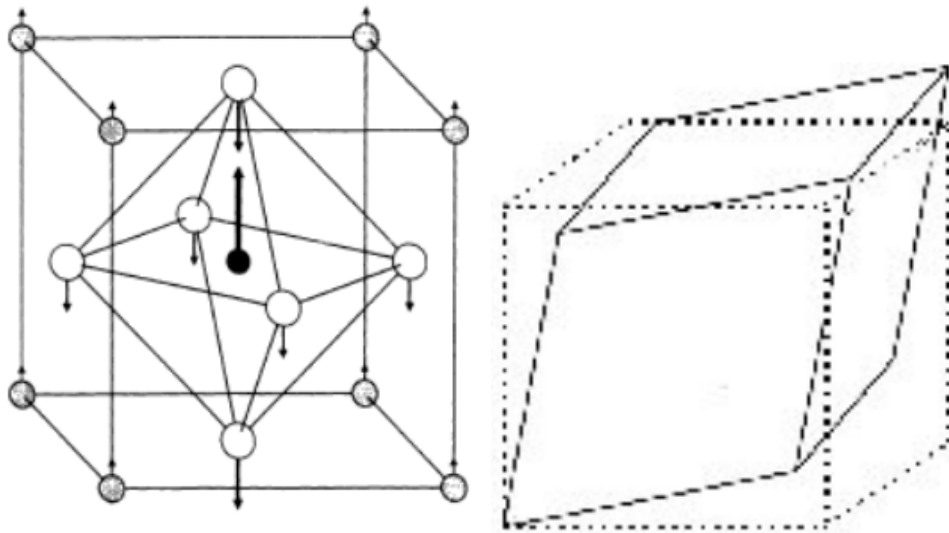


FIGURE 1.9: Relevant local atomic displacements associated to structural transitions.
Figure reprinted from Zhong *et al.*, [7].

Computation of on-site energy Distorting a crystal five-atom cell gives rise to an energy penalty. Computing an energy cost associated to any value of local modes requires a Taylor expansion around the cubic structure [7]. Coefficients of this expansion being energy derivatives, they are derived from first principles calculations. Total energy comprises five terms, as stated in equation 1.29.

$$E^{\text{total}} = E^{\text{self}}(\{\mathbf{u}\}) + E^{\text{dpl}}(\{\mathbf{u}\}) + E^{\text{short}}(\{\mathbf{u}\}) + E^{\text{elas}}(\{\eta_l\}) + E^{\text{int}}(\{\mathbf{u}\}, \{\eta_l\}) \quad (1.29)$$

An expansion up to at least fourth order has to be included in the first term (1.30) describing local on-site energy cost of distortion so as to compensate a possible instability generated by the second-order term and add a crystalline anisotropy term favoring polarization along easy axes.

$$E^{\text{self}}(\{\mathbf{u}\}) = \sum_i \left(\kappa_2 |\mathbf{u}_i|^2 + \alpha |\mathbf{u}_i|^4 + \gamma (u_{ix}^2 u_{iy}^2 + u_{iy}^2 u_{iz}^2 + u_{iz}^2 u_{ix}^2) \right) \quad (1.30)$$

Long range interactions

Point-like local dipoles associated to polar distortions give rise to electrostatic interaction. An effective charge computed by summing respective contributions of five atoms with respect to their displacement relates local mode with a point-like local dipole $\mathbf{d}_i = Z^* \mathbf{u}_i$. A classical Coulombic dipole-dipole interaction term then writes as in equation 1.31.

$$E^{\text{dpl}}(\{\mathbf{u}\}) = \frac{Z^{*2}}{\varepsilon_\infty} \sum_{i < j} \left(\frac{\mathbf{u}_i \cdot \mathbf{u}_j}{|\mathbf{R}_i - \mathbf{R}_j|^3} - \frac{3((\mathbf{R}_i - \mathbf{R}_j) \cdot \mathbf{u}_i)((\mathbf{R}_i - \mathbf{R}_j) \cdot \mathbf{u}_j)}{|\mathbf{R}_i - \mathbf{R}_j|^5} \right) \quad (1.31)$$

Notation \mathbf{R}_i represents position of cell i , with displacements due to inhomogeneous strain being neglected. Boundary conditions leading to existence of copies of dipoles located in the simulation cell have a decisive role on such an interaction that decays very slowly with distance.

Short range interactions

Remaining interactions represent terms decaying rapidly with distance. Inclusion of each contribution to total energy of effective Hamiltonian was needed to reproduce an experimentally observed sequence of structural transitions that only emerged from a delicate balance between all five interaction terms.

Nearest neighbors interaction Only taking into account a dipole-dipole term is a poor approximation of an energy landscape and fails at describing covalent interaction between neighboring local modes. Interactions up to third nearest neighbors taking into account a cubic reference state symmetry write as in equations 1.32 and 1.33.

$$E^{\text{short}}(\{\mathbf{u}\}) = \frac{1}{2} \sum_{i \neq j} \sum_{\alpha\beta} J_{ij,\alpha\beta} u_{i\alpha} u_{j\beta} \quad (1.32)$$

$$\left\{ \begin{array}{l} \text{First NN: } J_{ij,\alpha\beta} = \left(j_1 + (j_2 - j_1) \left| \hat{R}_{ij,\alpha} \right| \right) \delta_{\alpha\beta}, \\ \text{second NN: } J_{ij,\alpha\beta} = \left(j_4 + \sqrt{2} (j_3 - j_4) \left| \hat{R}_{ij,\alpha} \right| \right) \delta_{\alpha\beta} + 2j_5 \hat{R}_{ij,\alpha} \hat{R}_{ij,\beta} (1 - \delta_{\alpha\beta}), \\ \text{third NN: } J_{ij,\alpha\beta} = j_6 \delta_{\alpha\beta} + 2j_7 \hat{R}_{ij,\alpha} \hat{R}_{ij,\beta} (1 - \delta_{\alpha\beta}). \end{array} \right. \quad (1.33)$$

An intersite unitary vector $\hat{R}_{ij,\alpha} = \frac{(\mathbf{R}_i - \mathbf{R}_j)_\alpha}{|\mathbf{R}_i - \mathbf{R}_j|}$ was used in equation 1.33.

Inhomogeneous strain Local strain being approximated by displacements of cell corners $\mathbf{v}(\mathbf{R}_i)$ as in figure 1.9, independent cubic material elastic constants being expressed as B_{11} , B_{12} and B_{44} , elastic energy is split into a unique homogeneous strain term for simulated N cells reproduced in equation 1.34 and an inhomogeneous strain one (1.35). The distinction arises from the fact that inhomogeneous strain is defined by differences in displacement of unit cell corner between nearest neighbouring cells: for cells lying on the simulation supercell surfaces, the values of inhomogeneous strain on the site located on the opposite surface of the simulation supercell is taken into account. As a result, the difference in displacement from one surface to another always vanishes and homogeneous strain is not accounted for by equation 1.35.

$$E_H^{elas}(\{\eta_{H,l}\}) = \frac{N}{2} B_{11} \left(\eta_{H,1}^2 + \eta_{H,2}^2 + \eta_{H,3}^2 \right) + N B_{12} (\eta_{H,1} \eta_{H,2} + \eta_{H,2} \eta_{H,3} + \eta_{H,3} \eta_{H,1}) + \frac{N}{2} B_{44} \left(\eta_{H,4}^2 + \eta_{H,5}^2 + \eta_{H,6}^2 \right). \quad (1.34)$$

$$E_I^{elas} = \sum_i \left\{ \frac{B_{11}}{4} [v_x(\mathbf{R}_i) - v_x(\mathbf{R}_i \pm a\hat{\mathbf{x}})]^2 + \frac{B_{12}}{8} [v_x(\mathbf{R}_i) - v_x(\mathbf{R}_i \pm a\hat{\mathbf{x}})] [v_y(\mathbf{R}_i) - v_y(\mathbf{R}_i \pm a\hat{\mathbf{y}})] + \frac{B_{44}}{8} [v_x(\mathbf{R}_i) - v_x(\mathbf{R}_i \pm a\hat{\mathbf{y}})] [v_y(\mathbf{R}_i) - v_y(\mathbf{R}_i \pm a\hat{\mathbf{x}})] + \text{cyclic permutations} \right\}. \quad (1.35)$$

$A \pm$ sign stands for multiple terms that are summed.

Stress-strain interaction Order two elastic deformation tensor and order one local mode interaction are expressed in a most general form described in equation 1.36.

$$E^{\text{int}}(\{\mathbf{u}\}, \{\eta_l\}) = \frac{1}{2} \sum_i \sum_{l\alpha\beta} B_{l\alpha\beta} \eta_l(\mathbf{R}_i) u_\alpha(\mathbf{R}_i) u_\beta(\mathbf{R}_i). \quad (1.36)$$

Cubic symmetry allows only fifteen finite terms that depend on three independent coupling constants (1.37).

$$\begin{aligned} B_{1xx} &= B_{2yy} = B_{3zz}, \\ B_{1yy} &= B_{1zz} = B_{2xx} = B_{2zz} = B_{3xx} = B_{3yy}, \\ B_{4yz} &= B_{4zy} = B_{5xz} = B_{5zx} = B_{6xy} = B_{6yx}. \end{aligned} \quad (1.37)$$

Simulation techniques

Once an expression of energy as a function of a set of variables has been obtained, its global minimum represents the system state at zero temperature. To infer the behavior at finite temperature,

two types of numerical simulations can be performed.

Molecular dynamics Through derivation of the expression of energy as a function of each degree of freedom, forces can be obtained. Provided that effective masses are known, the second law of Newton relates accelerations to forces and actual trajectories can be computed. The kinetic energy in each degree of freedom is proportional to Boltzmann constant times temperature. As a result, a simulation at fixed temperature can be performed only if a numerical thermostat is devised and the dynamics of the system allows it to come to equilibrium with this thermostat.

Monte-Carlo Metropolis methods Another type of simulation does not attempt to reproduce the system dynamics at all but nevertheless allows to compute its properties on thermal equilibrium at a given temperature T . Statistical physics allows to derive the average of any physical observable quantity by dividing the integral over any possible state of a system of its probability (*i.e.* the exponential of its energy divided by Boltzmann constant times temperature) times the observable value by a normalization factor called the partition function. Each degree of freedom giving rise to an integral, the integral over all possible states is enormous and direct computation of the numerator or of the denominator is untractable. However, even though each part cannot be evaluated individually, a Monte-Carlo method can provide access to the observable average that represents the ratio of the two quantities. The name Monte-Carlo derives from the random sampling of the multidimensional integral and the exact method was devised by Metropolis *et al.* in 1953 [11]. It consists of several steps.

1. The system is in its original configuration
2. A trial displacement is generated, possibly leading to a new configuration
3. Energy difference between possible new configuration and original configuration is computed
4. If the energy difference is negative which means the new state has lower energy than original state, the trial displacement is immediately accepted and the system takes the new configuration.
5. If the energy difference is positive, a random number comprised between zero and one is generated.
6. The exponential of this energy difference divided by the Boltzmann constant times temperature is computed.
7. If the random number is smaller than the abovementioned quantity, the attempted move is rejected and the system stays in its original state.
8. If the random number is greater than the abovementioned quantity, the attempted move is accepted and the system changes to the new state.

9. Repeat all the previous steps until the desired number of Monte-Carlo steps is achieved

The acceptance of configuration depending on a random number corresponds to importance sampling: averaging a physical quantity over Monte-Carlo steps gives the equilibrium value of the quantity at the simulated temperature. In more detail, the particular implementation of Metropolis algorithm with the effective Hamiltonian that has just been described involves trial moves on local polar mode and local inhomogeneous strain of each site followed by acceptance or rejection of the move. Once a Monte-Carlo iteration has been performed on each site, a homogeneous strain trial move is attempted. The whole sequence of operations is called a Monte-Carlo sweep and the loop then continues.

In this section, a general introduction to concepts of ferroelectricity has been provided first and concepts as spontaneous structural transition at a critical temperature were presented. A rapid introduction to first principles computations came afterwards to justify that properties of a fundamental ground state of electron wavefunctions and nuclei positional degrees of freedom can be retrieved. In an attempt to model the energetics of structural distortions, an expansion of energy as a function of local modes amplitude and spatial repartition was reproduced from the literature. Some interactions are long-ranged and some short-ranged interaction also affect sites located on the borders of simulation cell. The expression of energy is then used in Monte-Carlo simulations to extract values of physical quantities at a given temperature. However, formulas dealing with nearest neighbors of edge sites or dipoles lying out of simulation cells require a proper definition of boundary conditions. This will be the focus of next subsection.

1.3.3 Boundary conditions

Edges of simulation cells can have a special status. Numerical techniques aiming at reproducing bulk behaviors usually tend to use periodic boundary conditions. The special case of isolated nanometric particles is studied by trying to avoid presence of any periodic copies. Intermixing between these two extreme situations can also be considered. Parameters describing strain and other ones for polar local mode are not necessarily simulated with the same boundary conditions. Electrical dipole-dipole interaction being long-ranged, it induces non-negligible different features between the two cases. A case that does not exhibit electrical periodic boundary conditions will be presented first and a so-called Ewald method aiming at dealing with an infinite number of dipole copies will be discussed afterwards.

Isolated ferroelectric nanoparticles

Presence of surfaces makes it complex to set boundary conditions for isolated dots and the long-ranged electrostatic interaction part needs particular care: ferroelectric nanoparticle surfaces can give rise to the notion of depolarizing field.

Spontaneous polarization screening A variety of exotic orderings in polarization configurations including vortices arise in simulated patterns due to the energetic cost of homogeneous polarization in the absence of any free charges compensating polarization-generated electric field. Such a total absence of compensation is readily taken into account by restricting the summation in equation (1.31) to sites located inside the simulation supercell. However, only taking into account the dipoles of a homogeneously polarized material gives rise to an electric field intensity computed in equation 1.38 along polarization direction that ultimately prevents any homogeneous polarization from building up and leads to exotic polarization patterns.

$$E_{\text{dep}} = -\frac{P}{\varepsilon_0} \quad (1.38)$$

Experimental quest of such complex simulated polarization patterns was hindered by several mechanisms leading to a diminution of magnitude of this electric field. Free charges having a value opposite to those of bound charges tended to come at the surfaces and compensate the depolarizing field. As a consequence, the resulting depolarizing field was smaller and a screening coefficient β was then defined (1.39).

$$E_{\text{dep}} = (1 - \beta) \frac{P}{\varepsilon_0} \quad (1.39)$$

A material nanoslab inserted in a planar capacitor feels a full depolarizing electric field in the case of non-connected plates. This is the reason why the $\beta = 0$ case is called Open-Circuit. As an example, lines indicate the borders of a 4x4 dipole plane in figure 1.10.

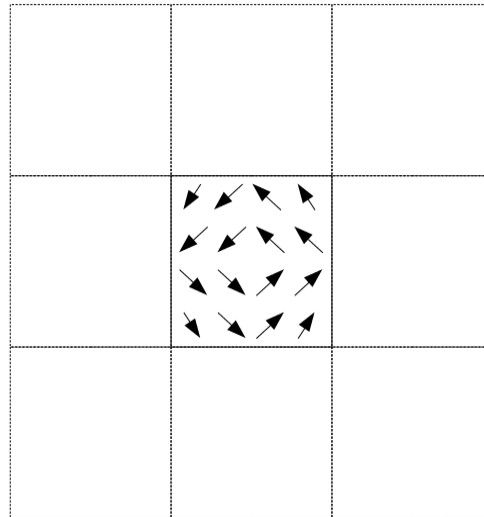


FIGURE 1.10: Isolated planar array of 4x4 dipoles boxed in a square representing an example of Open Circuit boundary conditions.

By construction, periodic boundary conditions applied on dipole charge sources imply electric potential is also periodic *i. e.* it has the same value at the borders of simulated cell and no average electric field can be experienced between these borders. A material nanoslab inserted between

shorted plates is said to be under Short-Circuit boundary conditions as represented for another 4x4 dipole plane in figure 1.11. The difficulties of extending the summation in equation (1.31) to an

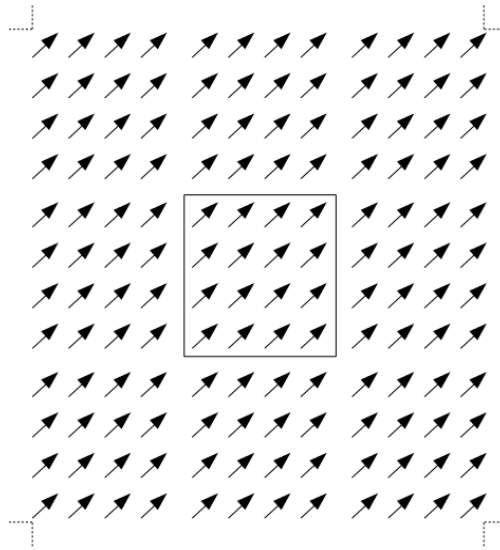


FIGURE 1.11: Planar array of 4x4 dipoles boxed in a square and surrounded by copies of itself representing an example of Short Circuit boundary conditions.

infinite number of copies will be dealt with in the periodic construct case. Mechanisms screening electric field do not necessarily need coating by shorted conductive planes. Free charges circulation between material edges may arise due to finite conductivity in bulk. Dissociation of surrounding medium molecular adsorbates has comparable, yet less efficient effects.

Short-range interactions In the model that has been described, there are several terms including equations 1.32 and (1.35) that are computed as differences between the respective values of polarization and cell corner displacement in considered cell and those in neighbouring cells. If the simulation aims at reproducing the bulk, the values at sites located on the opposite surface of simulation supercell can be used. However, for an isolated dot, the effects of dipoles located on one surface must not influence those located on the other surface of the dot. Therefore, as computing contributions to energy on surfaces requires values at points located immediately next to simulated supercell, a boundary condition for strain and local mode had to be chosen. This lead to surrounding the cube with an external layer of sites in which polar local mode and inhomogeneous strain is set to zero. Through this technique, periodic boundary condition on computing inhomogeneous strain and nearest neighbor dipole-dipole interaction energy term was kept but interaction between opposite surfaces was suppressed. Computation of homogeneous strain was left unchanged.

Periodic constructs

Simulating features of the bulk case requires extremely large simulation supercells due to the negligible effect of surface terminations caused by the small ratio of atomic sites located on the edges

with regard to their total number. Periodic boundary conditions is a convenient workaround but imposing them requires special care when dealing with long-ranged interactions.

Electrostatic interaction More details on electrostatic interaction computation will now be provided to explain how results are changed. The initial approximation in Born effective charge computation which is that charge distributions created by crystal polar distortions can be approximated with point-like dipoles is assumed again. Moreover, neglecting dipole-dipole distance variations with homogeneous and inhomogeneous strain as being of higher order and taking advantage of linearity of electrostatics equations allows again to rewrite the electrostatic energy term (1.40).

$$E^{\text{dpl}} = \sum_{ij,\alpha\beta} Q_{ij,\alpha\beta} u_{i,\alpha} u_{j,\beta} \quad (1.40)$$

However, computation of coefficients $Q_{ij,\alpha\beta}$ with dipole-dipole interaction energy expression of equation 1.31 and periodic boundary conditions lead to an alternating serie that cannot be truncated without a significant loss in accuracy. But equation 1.31 itself was computed from the definition of electrostatic energy: opposite of dipole moment at site i times electric field created on site i by all other dipoles located at any site $j \neq i$, the electric field created at site i by a dipole located at site j being itself the opposite of the gradient of the potential $V_j(\mathbf{r} - \mathbf{R}_j)$ that verifies Poisson equation 1.41.

$$-\frac{\epsilon_\infty}{4\pi} \Delta V_j(\mathbf{r} - \mathbf{R}_j) = Z^* \mathbf{u}_j \cdot \nabla \delta(\mathbf{r} - \mathbf{R}_j) \quad (1.41)$$

The Green's function of Laplace equation which means a function that solves $\Delta G(\mathbf{r}, \mathbf{R}_j) = \delta(\mathbf{r} - \mathbf{R}_j)$ being $G(\mathbf{r}, \mathbf{R}_j) = -\frac{1}{4\pi} \frac{1}{|\mathbf{r} - \mathbf{R}_j|}$, one can reobtain the contribution of interaction between dipole i and field created by dipole j to equation 1.31 by writing 1.42.

$$\begin{aligned} -Z^* \mathbf{u}_i \cdot \mathbf{E}_j &= \frac{Z^{*2}}{\epsilon_\infty} \mathbf{u}_i \cdot \nabla \left(\mathbf{u}_j \cdot \nabla \frac{1}{|\mathbf{r} - \mathbf{R}_j|} \right)_{\mathbf{r}=\mathbf{R}_i} \\ &= \frac{Z^{*2}}{\epsilon_\infty} \mathbf{u}_i \cdot \nabla \left(\frac{\mathbf{u}_j \cdot (\mathbf{r} - \mathbf{R}_j)}{|\mathbf{r} - \mathbf{R}_j|^3} \right)_{\mathbf{r}=\mathbf{R}_i} \\ &= \frac{Z^{*2}}{\epsilon_\infty} \mathbf{u}_i \cdot \left[\frac{1}{|\mathbf{r} - \mathbf{R}_j|^3} \nabla (\mathbf{u}_j \cdot (\mathbf{r} - \mathbf{R}_j)) + (\mathbf{u}_j \cdot (\mathbf{r} - \mathbf{R}_j)) \nabla \left(\frac{1}{|\mathbf{r} - \mathbf{R}_j|^3} \right) \right]_{\mathbf{r}=\mathbf{R}_i} \\ &= \frac{Z^{*2}}{\epsilon_\infty} \left[\frac{\mathbf{u}_i \cdot \mathbf{u}_j}{|\mathbf{R}_i - \mathbf{R}_j|^3} - 3 \left(\frac{(\mathbf{u}_j \cdot (\mathbf{R}_i - \mathbf{R}_j)) (\mathbf{u}_i \cdot (\mathbf{R}_i - \mathbf{R}_j))}{|\mathbf{R}_i - \mathbf{R}_j|^5} \right) \right] \end{aligned} \quad (1.42)$$

As a consequence, the challenge of periodic boundary conditions is to find an expression providing the electric field created by not only by dipole j but by dipole j and all its periodic copies. The periodicity of a lattice of simulation supercells having volume Ω_c naturally defines a Dirac Comb $\text{III}(\mathbf{r}) = \sum_{\{\mathbf{R}_{\text{supercell}}\}} \delta(\mathbf{r} + \mathbf{R}_{\text{supercell}})$, constituted of an infinite sum of Dirac deltas translated by an integer number of simulation supercells in real space, this lattice giving rise to a lattice of reciprocal vectors $\{\mathbf{G}\}$. The general steps were expected to be the same as for the non-periodic case, including writing the Poisson equation, solving it to obtain electrical potential created by a dipole and its copies, and taking the opposite and deriving with respect to space to obtain electric field. Regarding the writing and solving of Poisson equation, periodicity suggests to do it in Fourier space as functions that are supercell-periodic can be written as a convolution product between

a Dirac comb and a windowed function that has finite values only inside the simulation supercell, the Fourier transform being the product of the reciprocal lattice $\{\mathbf{G}\}$ Dirac comb times the Fourier transform of the windowed function. As a result, Poisson equation directly provides the Fourier coefficients at $\{\mathbf{G}\}$ points of a Fourier series that yields electrical potential. Inverse Fourier transform has to be performed to obtain a quantity defined in real space. However, the convolution of a Dirac comb with a point-like dipole has a Fourier signature that does not decay at high $\|\mathbf{G}\|$. Gaussian charge packets having width proportional to $1/\lambda$ on the one hand and opposite Gaussian charge packets superimposed on point-like dipoles on the other hand at each periodic copy of a site represent the Ewald-Kornfeld split of the right hand side of Poisson equation as represented in figure 1.12. The electrostatic potential created by opposite Gaussian charge packets

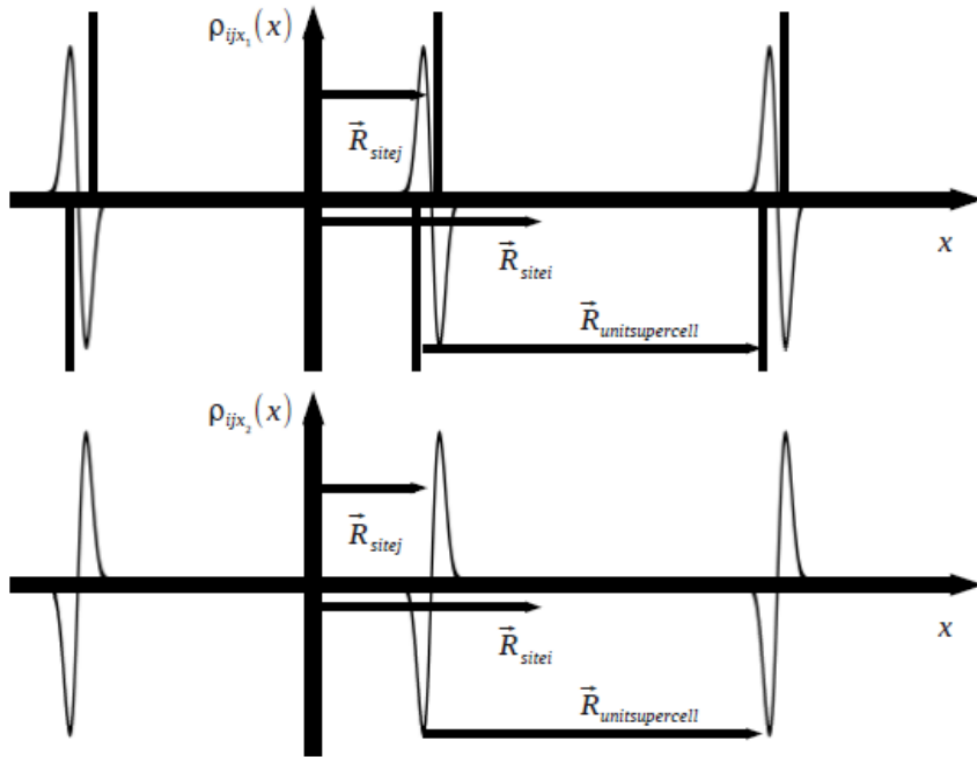


FIGURE 1.12: Charge distributions whose sum gives an array of point-like dipoles.

superimposed on point-like dipoles ρ_{ij1} decays so fast in real space for sufficiently large values of parameter λ that its entire contribution to electric field is neglected. The array of Gaussian charge packets located at \mathbf{R}_j plus any translation by $\{\mathbf{R}_{supercell}\}$ represent, in Fourier space, an electric charge density reproduced in equation 1.43 that decays at high $\|\mathbf{G}\|$.

$$\hat{\rho}_{ij2}(\mathbf{k}) = Z^*(\mathbf{u}_j \cdot \mathbf{ik}) \exp\left(-\mathbf{ik} \cdot \mathbf{R}_j - \frac{|\mathbf{k}|^2}{4\lambda^2}\right) \hat{\Pi}(\mathbf{k}) \quad (1.43)$$

The Poisson equation in Fourier space then provides expression 1.44 for the Fourier coefficients of electric potential created by the dipole at site j and all its copies and one can use gauge freedom to

set $\widehat{V}_j(\mathbf{0})$.

$$-\frac{\varepsilon_\infty}{4\pi} |\mathbf{G}|^2 \widehat{V}_j(\mathbf{G}) = Z^*(\mathbf{u}_j \cdot \mathbf{iG}) \exp\left(-\mathbf{iG} \cdot \mathbf{R}_j - \frac{|\mathbf{G}|^2}{4\lambda^2}\right) \quad (1.44)$$

Potential discrete Fourier transform then leads to discrete Fourier transform of electric field through multiplication by reciprocal lattice vectors. Electrostatic dipole-dipole interaction energy term is then obtained by multiplication by origin shift to site i performed by multiplication with a $\exp(\mathbf{iG} \cdot \mathbf{R}_i)$ prefactor followed by inverse Discrete Fourier Transform and scalar product with opposite of local mode times Born effective charge. Interaction energy then writes as in equation 1.45.

$$E^{\text{dpl-intersite}} = \frac{2Z^{*2}}{\varepsilon_\infty} \frac{\pi}{\Omega_c} \sum_{\mathbf{G} \neq \mathbf{0}} \frac{1}{|\mathbf{G}|^2} \exp\left(-\frac{|\mathbf{G}|^2}{4\lambda^2}\right) \sum_{ij} (\mathbf{G} \cdot \mathbf{u}_i) (\mathbf{G} \cdot \mathbf{u}_j) \cos(\mathbf{G} \cdot \mathbf{R}_{ij}) \quad (1.45)$$

On-site interaction Q_{ii} represents energy of a dipole in the field created by all its replicas except itself. Every time i equals to j , an additional contribution due to the dipole itself has to be subtracted, leading to the three terms of figure 1.13. Taking into account electric field created by an isolated Gaussian charge packet having expression (1.46) at its origin leads to an energy correction reproduced in equation 1.47.

$$\rho_{ii3}(\mathbf{r}) = \nabla \mathcal{N}_\lambda(\mathbf{r}) = \left(\frac{\lambda}{\sqrt{\pi}}\right)^3 \nabla \exp(-\lambda^2 \mathbf{r}^2) \quad (1.46)$$

$$E^{\text{dpl-onsite}} = \frac{2Z^{*2}}{\varepsilon_\infty} \sum_i \left(\frac{\lambda^3}{3\sqrt{\pi}} u_i^2\right) \quad (1.47)$$

An expression for an entire dipole-dipole electrostatic interaction matrix should contain these two parts as in equation 1.48.

$$Q_{ij,\alpha\beta} = \frac{2Z^{*2}}{\varepsilon_\infty} \left[\frac{\pi}{\Omega_c} \sum_{\mathbf{G} \neq \mathbf{0}} \frac{1}{|\mathbf{G}|^2} \exp\left(-\frac{|\mathbf{G}|^2}{4\lambda^2}\right) \cos(\mathbf{G} \cdot \mathbf{R}_{ij}) G_\alpha G_\beta - \frac{\lambda^3}{3\sqrt{\pi}} \delta_{\alpha\beta} \delta_{ij} \right] \quad (1.48)$$

Short-range interactions Periodic boundary condition simplifies short range interactions computation on surfaces. Local strain (1.35) and nearest neighbors interaction (1.33) then take into account respective value of inhomogeneous strain and polar local mode at sites located on the opposite surface.

A reminder about definition of depolarization coefficient was provided first. A description of how an infinite amount of periodic copies of dipoles located in a simulation cell has to be dealt with was provided afterwards. External boundaries were the focus of attention even though simulated shapes sometimes also exhibit internal boundaries. Different shapes lead to various local orderings of polarization and these will be the focus of next subsection.

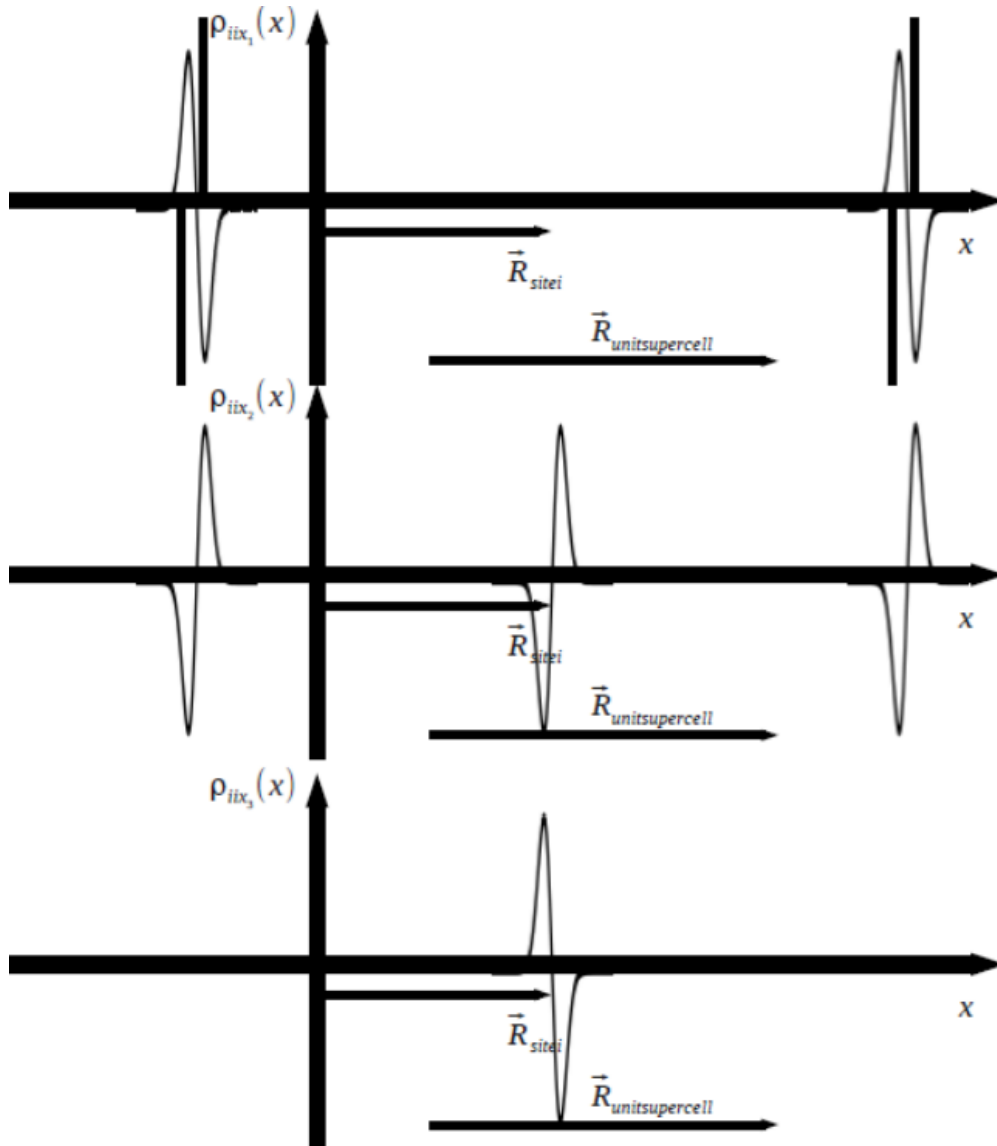


FIGURE 1.13: Charge distributions whose sum gives an array of point-like dipole copies.

1.3.4 About order parameters evidenced in ferroics numerical simulations

The very large number of parameters that can describe a given state of a distribution of dipoles has already been studied through several numerical simulations. Periodic boundary conditions and a simulation cell composed of one type of material simulates the ferroelectric bulk and has been quite successful at reproducing experimental results, namely a transition from one crystal structure to another. This type of crystal structure transition implies that the dipole moment and strain on all sites is on average finite and has a different value before and after the transition. In other situations, a transition between two distinguishable states was observed but the average of \mathbf{p} before and after the transition remained the same: homogeneous polarization no longer represented the order parameter. Another quantity called toroidal moment $\mathbf{r} \times \mathbf{p}$ became, on average,

finite. In the study of hollow nanocubes, this order parameter will be of particular interest. In another geometry, the averages of polarization and toroidal moment before and after the transition remained, on average null. A different quantity called hypertoroidal moment $\mathbf{r} \times \mathbf{r} \times \mathbf{p}$ was shown to be the order parameter. That last quantity will prove helpful in describing the ordering of polarization in nanotori afterwards. Experimental reports did not entirely confirm these simulated patterns. Simulations leading to toroidal moment will be mentioned first, and literature dealing with hypertoroidal moment will be presented afterwards.

On toroidal moments

As soon as boundary conditions no longer feature a perfectly uniform material, homogeneous polarization is not always a preferred ground state. Two ways of breaking translation symmetry were studied in depth featuring (i) truncation of material at the borders of simulation cell and (ii) alloying with another material while keeping periodic boundary conditions [12].

Toroidal moment alone Vortex ordering and absence of homogeneous polarization was observed on removing entirely a periodic boundary condition when simulating a dot of BTO containing $12 \times 12 \times 12$ local dipoles as can be seen in figure 1.14. Temperatures of onset of a so-called toroidal moment were slightly lower than those of onset of homogeneous polarization in bulk materials. However, completely removing periodic boundary conditions in a simulation is equiv-

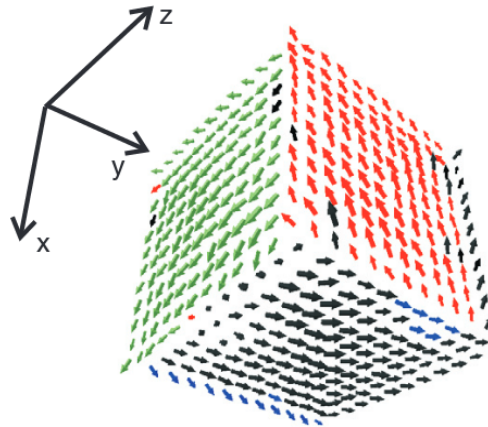


FIGURE 1.14: Vortex pattern formed by local dipoles. Figure reprinted from Prosandeev *et al.*, [12].

alent to setting depolarization coefficient β to zero. As mentioned earlier, this does not necessarily model an isolated ferroelectric as free charges can go through the material due to finite conductivity or dissociation of adsorbates at the surfaces. Aberration corrected High Resolution Transmission Electron Microscopy has been performed by Polking *et al.* [13] on an individual BTO nanocube, individual polar displacements were observed from two perpendicular directions and did correspond to a homogeneous polarization pattern without any vortex, as shown in figure 1.15. Other numerical simulations were performed for a cube in which short range interactions

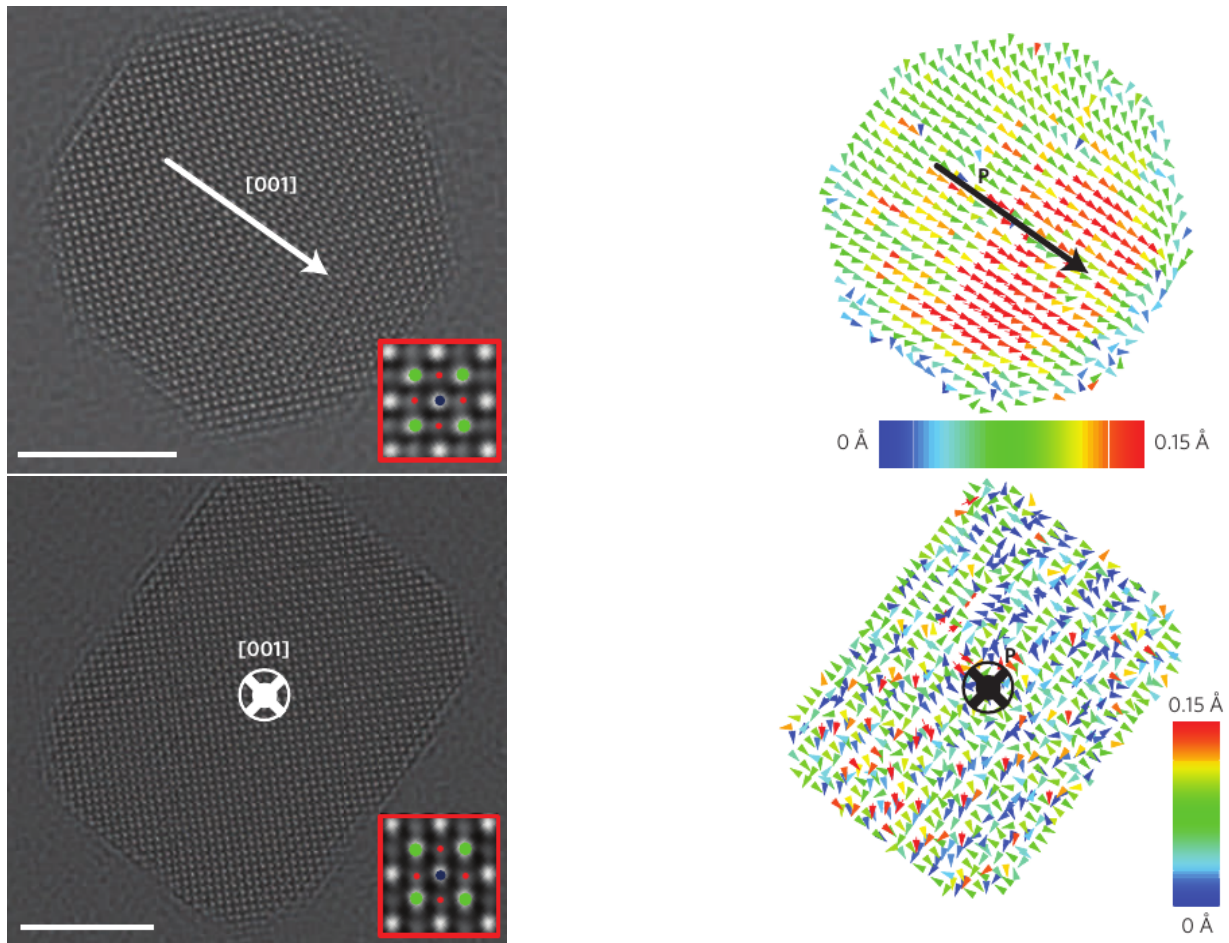


FIGURE 1.15: HRTEM observation (left) and local polarization map (right) of a BTO nanocube, respectively in a $\{100\}$ (top) and $\{001\}$ plane. Figure reprinted from Polking *et al.*, [13].

are again suppressed on the edges through addition of a layer in which inhomogeneous strain and local polarization is cancelled but electrical boundary conditions are computed as in the periodic case to mimic short-circuit boundary conditions ($\beta = 1$). The system then favoured homogeneous polarization at equilibrium [14]. Intermediate values of depolarization coefficient were studied by using linear combinations of the dipole-dipole interaction energy in the $\beta = 0$ and $\beta = 1$ cases as the experimental case is an intermediate between short and open-circuit boundary conditions that is closer to $\beta = 1$ than to $\beta = 0$.

Periodic constructs containing eight BTO $12 \times 12 \times 12$ dots interspaced by another material apparently lead to numerous possibilities including toroidizations of alternated signs presented in figure 1.16, possibly leading to cancellation of overall toroidal moment. Several periodic simulations were also performed in a simulation supercell containing only one BTO dot surrounded by one layer of another material. By increasing the size of the simulated dot, the BTO fraction of the total material was increased. When the permittivity of the interstitial material was also increased, a transition from simulated toroidal moment with no polarization to a homogeneously polarized state with no toroidal moment occurred [15], as shown in figure 1.17. This behavior is very general

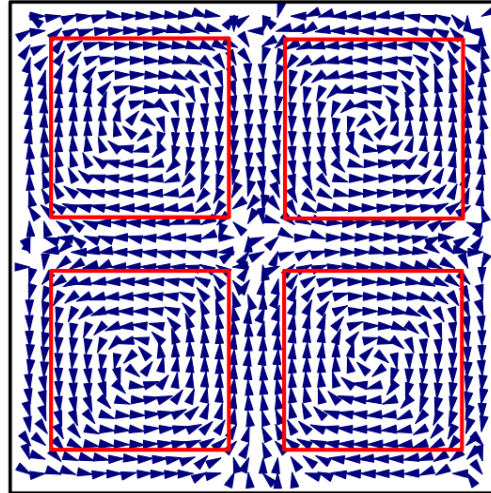


FIGURE 1.16: Cross-section of several vortices of opposite chirality formed by local dipoles in a matrix of BTO dots (circled in red) interspaced by another material. Figure reprinted from Prosandeev *et al.*, [12].

and does not only describe ferroelectrics: due to the diminishing role of interfaces on increasing the grain size, large grains can be homogeneously polarized without an important energy penalty whereas grains smaller than a critical size tend to break into domains, as it was first described for magnetic materials [16]. In ferromagnetic materials, the vortex cores of toroidic domains [17] in

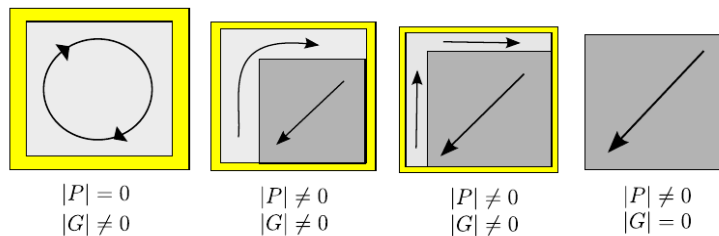


FIGURE 1.17: Polarization configuration with, from left to right, interstitial material decreasing thickness and increasing permittivity. Figure reprinted from Anoufa [15].

isolated particles have been experimentally observed several times [18, 19]. Similarly, macroscopic ferroelectricity seemed to vanish in ceramics made of sufficiently small particles [20]. But as a matter of fact, due to the difficulty at controlling depolarizing field, direct experimental observation of toroidal ordering in ferroelectric material has been reported for the first time very recently and in a composite rather than an isolated particle. The geometry in which vortices were observed is that of ferroelectric planes of PbTiO_3 interspaced by epitaxially grown planes of SrTiO_3 . High Resolution Scanning Transmission Electron Microscopy of a cross-section then allowed to obtain a polar map that is shown in figure 1.18.

Toroidal moment coexisting with homogeneous polarization By creating a matrix in which ferroelectric material has periodic boundary condition along only one direction, a maintained

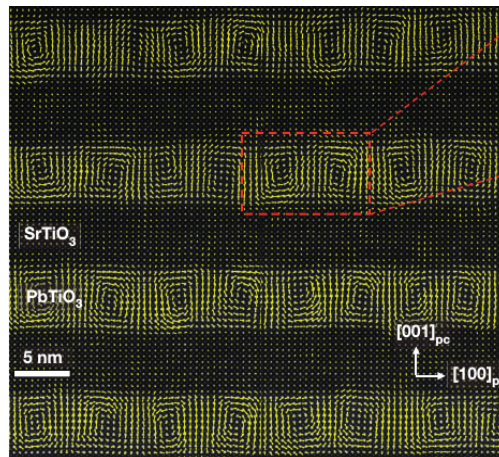


FIGURE 1.18: Experimental local polarization map evidencing vortices in the PbTiO_3 sublattice layers. Figure reprinted from Yadav *et al.* [21].

finite polarization along this direction was observed to be superimposed on a vortex pattern, as sketched in figure 1.19.

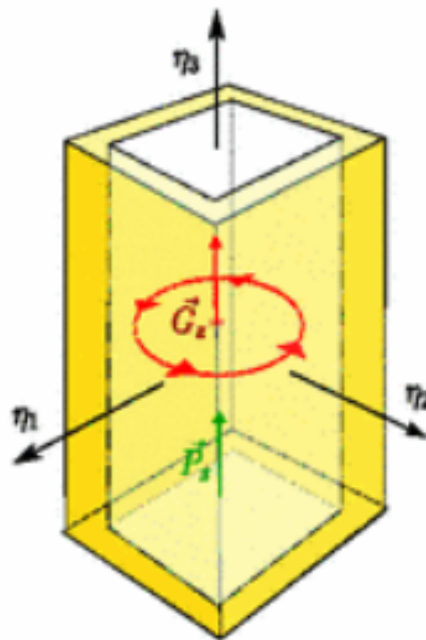


FIGURE 1.19: Scheme of superimposed vortices and homogeneous polarization in a matrix of BTO wires (in white) interspaced by another (yellow) material. Figure reprinted from Anoufa *et al.*, [22].

About hypertoroidal moments

Even though quadrupolar moment was somewhat left aside, a subset of higher order moments involving a double cross-product of position with local polarization received particular attention in numerical simulations of dipole arrays.

Hypertoroidal moment alone Evenly spaced dipoles placed in isolated original shapes that were also called hysterons gave rise to a unique finite order parameter with negligible homogeneous polarization or toroidal moment as can be checked on figure 1.20.

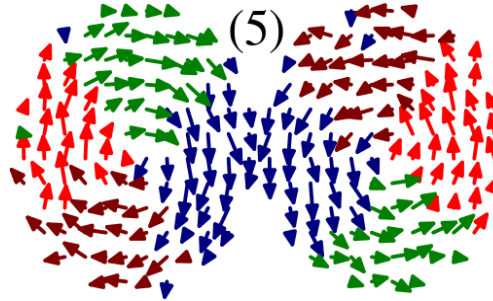


FIGURE 1.20: Cross-section of a dipole pattern present in a hysteron. Figure reprinted from Prosandeev *et al.*, [23].

Hypertoroidal moment coexisting with polarization In a more common cubic shape, homogeneous polarization was shown not to describe subtle features of edgy dipolar pattern that gave rise to so-called flower states during simulations of an intermediate between fully isolated and completely periodic boundary conditions (*cf.* Fig. 1.21).

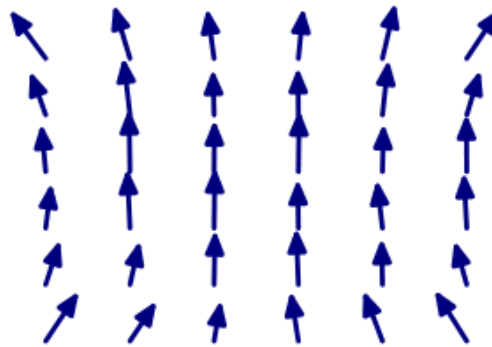


FIGURE 1.21: Cross-section of a dipole pattern present in a dot with neither isolated nor periodic boundary conditions. Figure reprinted from Prosandeev *et al.*, [23].

Parallelepipedic geometries under similar conditions also gave rise to dipole patterns called bubble states, in which total polarization is finite but fails at describing most of the ordering taking place as shown in figure 1.22.

Other types of ordering

In the quest for smaller topological defects, skyrmions recently received much attention.

Magnetic skyrmions Topologically protected chiral magnetic configurations arising due to additional term in magnetic spin-spin interaction (such as the Dzyaloshinskii-Moriya part) lead to

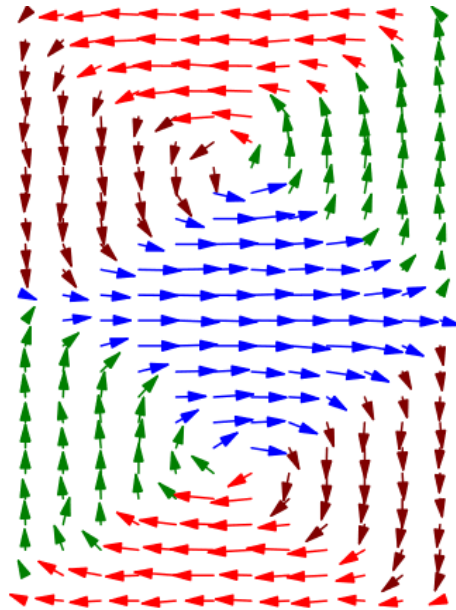


FIGURE 1.22: Cross-section of a dipole pattern present in an elongated dot. Figure reprinted from Prosandeev *et al.*, [23].

two branches of skyrmion research: individual manipulation of isolated skyrmions in ultrathin magnetic layers and observation of signatures coming from existence of skyrmion lattices in bulk materials. In more detail, the two spin configurations of figure 1.23 a and b arise due to the presence of an energy term that writes $-\mathbf{D}_{12} \cdot (\mathbf{S}_1 \times \mathbf{S}_2)$, in which \mathbf{D}_{12} is the Dzyaloshinskii-Moriya interaction vector. Electrons interaction with a skyrmion give rise to a giant effective Hall effect.

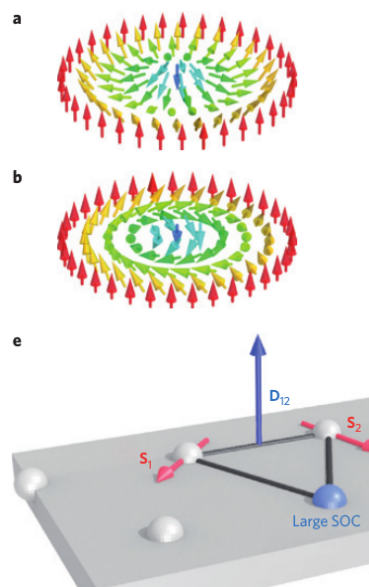


FIGURE 1.23: a and b represent two types of 2D skyrmions in a ferromagnet. e represents the 3-site indirect exchange interaction mechanism. Figure reprinted from Fert *et al.*, [24].

Even though present day hard disk drives have high densities of information per unit surface, they require complex and fragile mechanical parts and solid-state devices having comparable or higher bit densities are desired (ferroelectric bits represent an alternative for this aspect [25]). Racetrack memories inside which up and down magnetic domains are moved by a spin current represent an alternative, but critical currents inducing motions are high and defects represent a serious problem. Manipulating isolated skyrmion has the advantage of dealing with particles that have extremely small size, measuring in nanometers, and low depinning currents.

Skyrmions in ferroelectrics Lack of a vector product term in interaction energy between electric dipoles does not favour apparition of skyrmion in ferroelectrics. Yet, a geometry in which an array of wires of ferroelectric material is inserted into a matrix was submitted to a sequence of cooling steps followed by application of homogenous electric field. Depending on the intensity of applied electric field, a skyrmionic configuration was reached [26]. The ordering of local dipole moments is reproduced in figure 1.24 and is geometrically identical to the spin configuration described in magnetic skyrmions. Even though composition modulation makes displacements of

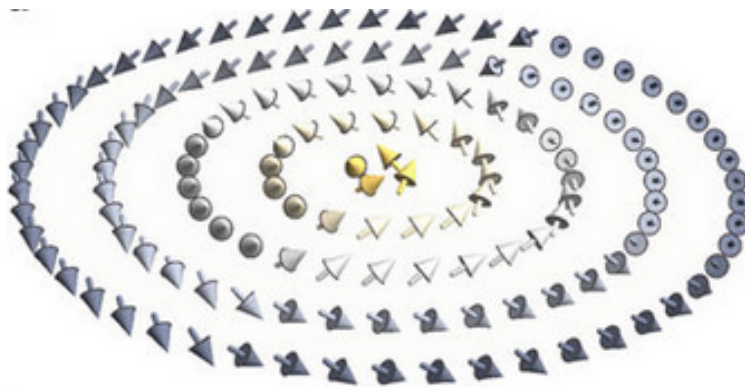


FIGURE 1.24: Local polarization field configuration at a simulated temperature of 15 K. Figure reprinted from Nahas *et al.*, [26].

these skyrmions unlikely and insulating nature of materials does not allow observation of ferroelectric skyrmions effect on free charge carriers, such an observation in composites represents a significant milestone.

1.4 Conclusion

A first section of this chapter has been devoted to Taylor expansion and tensor invariants, to show that there are sets of linear combinations of components that transform onto themselves under any rotation.

The following was devoted to a historical presentation of ferroelectricity. This class of materials are of interest due to remarkable properties: below a critical Curie temperature, they can have spontaneous polarization that translates into microscopical dipoles that are generally oriented

along the same direction, even in the absence of any external electric field, with two possible orientations, giving rise to remnant polarization. All these materials are also pyroelectric in the sense that spontaneous polarization also depends on temperature and piezoelectric, meaning that this remnant polarization can be tuned by mechanical stress. In more detail, the ferroelectric solids studied in the course of this thesis are ionic crystals, with a primitive cell containing five ions that repeats itself at each node of a lattice. Several symmetry operations can leave this primitive cell invariant and combination with translation-related operations must form one of 230 group structures, among which ten can be ferroelectric.

The transition from a paraelectric state to a ferroelectric one thus involves a displacement of the barycenter of positive charges with respect to that of negative charges. Materials being essentially tridimensional, several equivalent directions arise for spontaneous polarization, and a sequence of structural phase transitions is sometimes observed. The absence of spontaneous polarization in the paraelectric phase can be due to several phenomena: each lattice cell can have zero polarization, in which case the transition is said to be displacive or presence of polarization that is randomly oriented, leading to cancellation on average, in which case the transition is said to be order-disorder. Regardless of the microscopic mechanism of the transition, the equilibrium state can be derived by minimizing a phenomenological Landau-Devonshire energy. In a one-dimensional toy model, it is a polynomial that only includes even terms and in which the temperature only has an effect on the second order term. Depending on the sign of the fourth order term, the transition can involve a coexistence of two phases if it is of the first order or no coexistence if it is of the second order. Fitting terms to reproduce experimental results, adding extra terms for several spatially equivalent directions and taking strain into account gives a more complex expression for the energy but this expression reproduces most features of all structural transitions in a perovskite. This thesis used another approach as Landau theory has the drawback of being purely phenomenological.

Computing the energy associated to a given set of classical nuclei positions, due to Born-Oppenheimer approximation, and electron wavefunctions is a prerequisite for a predictive simulation method. Instead of tackling this problem, Density Functional Theory deals with minimization of the energy associated to another quantity called electronic density. Electrons being indistinguishable and electron-electron interaction being difficult to derive, an exchange-correlation term is added to energy and energy minimization is performed on a fictitious system of independent electrons. This energy minimization technique gives informations about the stable state at zero temperature but it does not describe the behavior of the system at high temperature. A perturbative expansion is constructed around the cubic structure and the coefficients are obtained through the abovementioned method. Metropolis algorithm then allows observables measurement at any temperature. As values of local parameters at nearest neighboring sites were needed in the computation, the simulation cell surfaces required to take care of boundary conditions in the case of an isolated particle. Moreover, the expression for long-ranged electrostatic interaction was

simpler in the case of an isolated particle than in that of periodic boundary conditions. As this simulation method does not require experimental input and can predict polarization patterns, some previously obtained simulation results were presented for isolated cubes and composites made of ferroelectric cubes interspersed in another material. Literature review then continued with a discussion of experimental observations. More complex ordering in more complex geometries were then discussed and chiral configurations called skyrmions were also presented.

Chapter 2

Syntheses of Barium Titanate nanospheres, nanocubes and nanotori

Contents

2.1 Syntheses and characterization	52
2.1.1 Solvothermal methods	52
2.1.2 Electron Microscopy	53
2.1.3 X-Ray diffraction	53
2.2 Synthesis steps	54
2.2.1 Precursor syntheses	54
2.2.2 Ion-exchange	56
2.3 Conclusion	63

FIRST syntheses of Barium Titanate macroscopic samples can be traced back to 1945. Macroscopic samples of this oxide have contributed to better understand the minimum requirements for ferroelectricity due to the relative simplicity of its crystal structure and its sequence of three phase transitions. Several properties are associated to this complex structural evolution including ferroelectricity, piezoelectricity, and optical activity and those have made possible new devices including actuators, non-volatile memories, strain sensors, optical modulators and possibly supercapacitors [27] thanks to a high permittivity. Among a variety of chemical routes leading to such an oxide, low temperature methods sometimes enable production of particles having nanometric dimensions. From a theoretical and experimental point of view, Barium Titanate nanoparticles are of interest due to the possibility of tuning physical properties of material by altering the size and shape of its constituting nanoparticles [28]. Numerical simulations have recently been performed on creative geometries such as nanowires [22], elongated nanodots [29], hysteron, symmetrical [30] and asymmetrical [31] nanotori. In this chapter, results reported in [32] will be presented: we will concentrate on a fraction of all possible soft chemistry routes and explain first which methods were used for growth and characterisation of nanoparticles. A general synthesis scheme will be detailed afterwards. Lastly, a set of parameters modifying obtained products will be analyzed.

2.1 Syntheses and characterization

Advanced routes yielding nanometric Barium Titanate are quite numerous. Ball-milling [33], coprecipitation, molten salts, spray or freeze-drying [34], emulsion, sol-gel can be cited in addition to solvothermal syntheses [35]. This last route represents an entirely low-temperature technique requiring cheap chemical reagents [36] and will be described first. Particles being smaller than visible light wavelengths being routinely produced, detection of particle shapes naturally involved electron microscopy techniques that will be mentioned afterwards.

2.1.1 Solvothermal methods

As a description of solvothermal methods, figure 2.1 represents a typical synthesis pressure vessel. A characteristic of so-called solvothermal methods being heating of a sealed reaction vessel

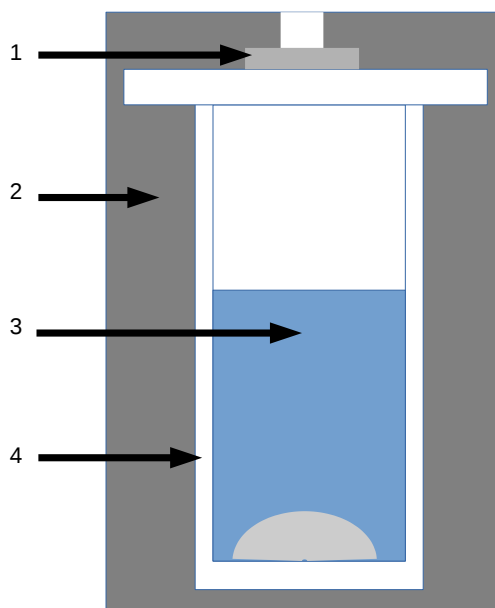


FIGURE 2.1: Representation of a pressure vessel having a (1) spring and bursting disk protecting from overpressure, (2) a stainless steel envelope surrounding (3) reagents, solvent and solid residue that are inside a (4) TeflonTM cup.

above the solvent boiling point, relatively large autogenous pressures are commonly reached. Presence of a TeflonTM liner aims at protecting stainless steel from corrosive reagents. Temperatures required to react grinded solid-state precursor powders being in excess of a thousand Celsius degrees and solvothermal conditions being possibly reached near a hundred degrees, a drastic reduction in syntheses temperatures is observed. Part of the reason may come from altered solvent properties on heating, including a sharp decrease in viscosity and a possible rise in precursors solubility and mobility. But the autogenous pressure is probably the main contributing factor. For

a liquid solvent in a closed system in which it is in equilibrium with its vapour and in the absence of any other gaseous species, at a fixed temperature there exists only one equilibrium pressure called the saturating vapour pressure. Equilibrium means that the system is stationary or that at any time there are as many molecules leaving the liquid phase to enter the gaseous phase as there are molecules from the gaseous phase that return to the liquid phase: for smaller pressures at this fixed temperature, the solvent will transform to the gaseous phase and it will fully convert to liquid phase for larger pressures. In the case of a closed system containing additional gaseous molecules at a fixed temperature, it is the fraction of total pressure due to the solvent gaseous phase (called partial pressure) that distinguishes two cases: for a partial pressure smaller than the solvent saturating vapour pressure, the entire solvent will be in the vapour phase. Otherwise, the gaseous phase will be said to be saturated of solvent molecules and any other solvent molecule added to the system will be in the liquid phase. The saturating vapour pressure increases with temperature and, under a fixed total external pressure, solvent is said to have reached its boiling point when its vapour pressure becomes equal to the external pressure. However, there is a critical temperature over which the distinction between liquid and gaseous phase vanishes so until the solvent critical point, pressure inside vessel is essentially linked to vapour pressure and remains independent from filling ratio. Above a solvent critical point, pressure will depend on autoclave content. Any temperature profile can be chosen so heating and cooling rate can be adjusted as much as dwell time. Autoclave used throughout subsequent studies were mainly Parr instrument digestion vessels 4744 and 4748 that have respective volumes 45 mL and 125 mL.

2.1.2 Electron Microscopy

Typical sample preparation routines involved ultrasonication of product powders in ethanol for half an hour followed by dipping of 300-mesh Transmission Electron Microscopy (TEM) copper grids with lacey carbon films. TEM experiments were carried out at a Titan G2 microscope operating between 60 and 300 kV. High resolution images were obtained with an aberration-corrected probe.

Similar preparation techniques were employed for preparing samples on which Scanning Electron Microscopy (SEM) was performed. SEM experiments were performed with a Leo Gemini 1530 Microscope having a Field Emission Gun.

2.1.3 X-Ray diffraction

Radiation intensity at various angles is recorded and peaks can then be indexed to a given crystal structure. A Joint Committee on Powder Diffraction Standards (JCPDS) database contained reference angles for peaks of crystalline materials.

X-ray Powder diffraction patterns were recorded with a Brüker D2 Phaser diffractometer having a copper radiation source and an X-Flash detector.

2.2 Synthesis steps

Chemical species comprising respectively Barium and Titanium have to be among reagents in the final step leading to Barium Titanate. Solvothermal syntheses were very sensitive to small variations in reaction parameters [37] as obtained product shapes were found to differ drastically on small changes such as reaction temperature or concentration of $\text{Ba}(\text{OH})_2$ [38]. Studying spontaneous shape generation requires reagents to be as monodisperse as possible.

2.2.1 Precursor syntheses

Dissolved Ba^{2+} cations coming from Barium Hydroxide octahydrate $\text{Ba}(\text{OH})_2 \cdot 8\text{H}_2\text{O}$ provided a source of Barium that did not play a significant role in shape generation processes [39]. Attention focused on solid titanium precursors coming from a variety of preliminary solvothermal syntheses. Layered alkali-metal or protonic titanate solid-state products were typically obtained in a first step and were used afterwards in a second reaction leading to Barium Titanate. Three types of titanium precursors were obtained and were written as NTO for $\text{Na}_2\text{Ti}_3\text{O}_7$, KTO for $\alpha - \text{K}_2\text{Ti}_6\text{O}_{13}$ and HTO for $\text{H}_2\text{Ti}_3\text{O}_7$. Figure 2.2 illustrates growth of NTO nanorods. A 10 M aqueous solution

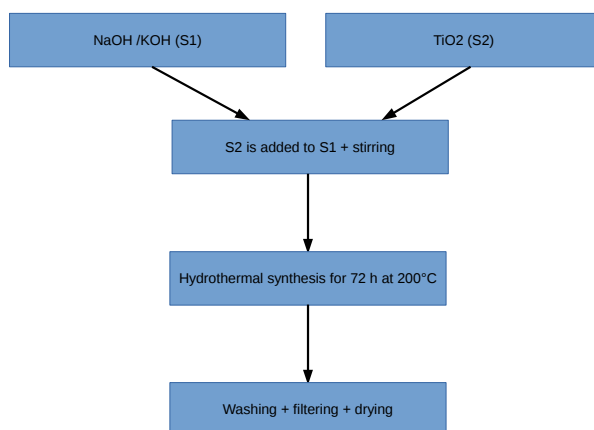


FIGURE 2.2: Diagram representing some important synthesis steps leading to NTO nanorods or KTO nanotubes.

of NaOH was prepared first by adding an adequate mass of pellets to deionized water directly inside a hydrothermal Teflon cup that was filled at seventy percent of its total volume. A Titanium concentration of 2.7×10^{-1} M was then reached by adding TiO_2 anatase under continuous stirring for 90 minutes. Solvothermal conditions were reached by heating mixture until arriving at 200°C for 72 hours. After letting autoclave return to room temperature, filtering of precipitate and washing with deionized water was repeated until pH of filtered solution was close to seven. Filtration was followed by redispersion in ethanol and drying for 12 hours in an oven at 70°C . Resulting powder X-Ray diffraction pattern was reproduced in figure 2.3 b1. All peaks were indexed to standard JCPDS XRD pattern number 31-1329 corresponding to NTO. A representative

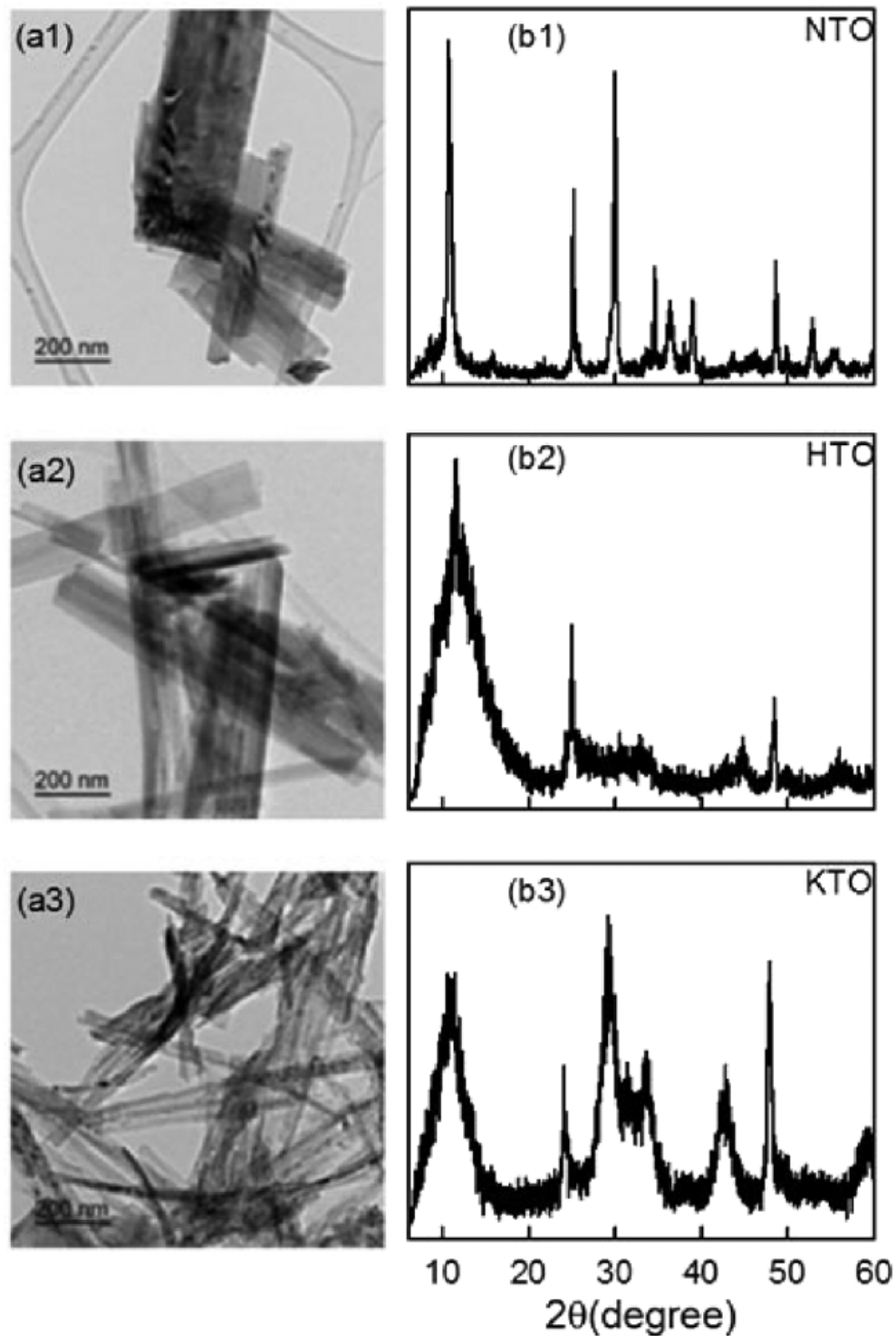


FIGURE 2.3: X-Ray diffraction peaks (a1, a2, a3) and TEM observation (b1, b2, b3) of NTO, HTO and KTO nanorods.

TEM observation of as-synthesized NTO samples can be found in figure 2.3 a1. Solid particles were obtained and nanorods is an accurate description of these NTO shapes. Lengths ranged from one to ten micrometers and diameter was one or several hundred nanometers. A H^+/Na^+

ion-exchange reaction was then performed in a solution of HCl to get HTO nanorods from obtained NTO powders. Concentration of HCl solution was 0.1 M and it had to be stirred over 15 hours.

Figure 2.3 b2 represents X-Ray diffraction pattern after ion exchange. All peaks can be indexed to standard JCPDS XRD pattern number 41-0192 corresponding to HTO. Figure 2.3 a2 shows a TEM image after ion exchange. Solid particles were preserved and HTO shapes can also be described as nanorods. Dimensions were left unchanged with micrometric lengths and diameters being around hundreds of nanometers.

KTO syntheses shared common features with the route to obtain NTO nanorods except for the replacement of NaOH by a 10 M KOH aqueous solution. Figure 2.3 b3 represents X-Ray diffraction peaks associated to samples obtained through steps of KTO synthesis. JCPDS XRD pattern number 40-0403 for KTO contained all peaks that corresponded to the powder. TEM observation of KTO samples is represented in figure 2.3 a3. Obtained particles were hollow as one can check on figure 2.4 b obtained at a higher magnification and KTO shapes can be described as nanotubes. Typical diameters were around thirty nanometers and lengths were roughly one micrometer.

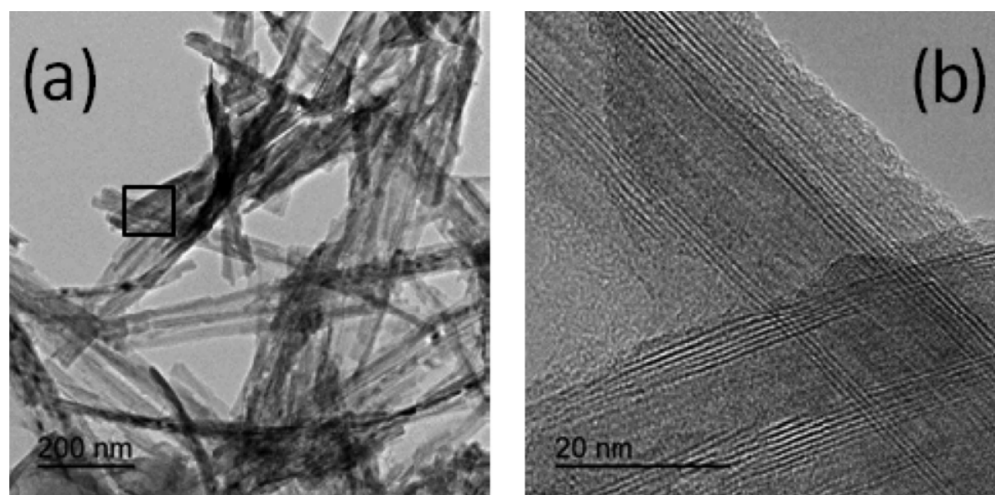


FIGURE 2.4: Scaled up (b) TEM observation of KTO nanotubes (a).

2.2.2 Ion-exchange

Barium titanate was obtained after a second solvothermal treatment involving previously synthesized NTO, HTO or KTO precursor and $\text{Ba}(\text{OH})_2 \cdot 8\text{H}_2\text{O}$ as Barium source. The Na^+ , H^+ or K^+ cation accompanying Titanium was topotactically replaced by Ba^{2+} in solution. Studying obtained shapes leads to comparison between products after ion exchange and relatively monodisperse Titanium precursors morphology. A two step solvothermal route allows to avoid use of macroscopic Titanium precursor powders that decorrelates reagent geometry from nanometric products. Deionized water was boiled for an hour and cooled to 4°C directly inside the Teflon cup

[40]. N_2 was bubbled through solvent at this low temperature so as to saturate solvent with it as one can see in figure 2.5 and as little CO_2 as possible was absorbed and thus $BaCO_3$ formation was minimized. A volumetric mix containing 60 percents of ethanol for 40 percents of water was

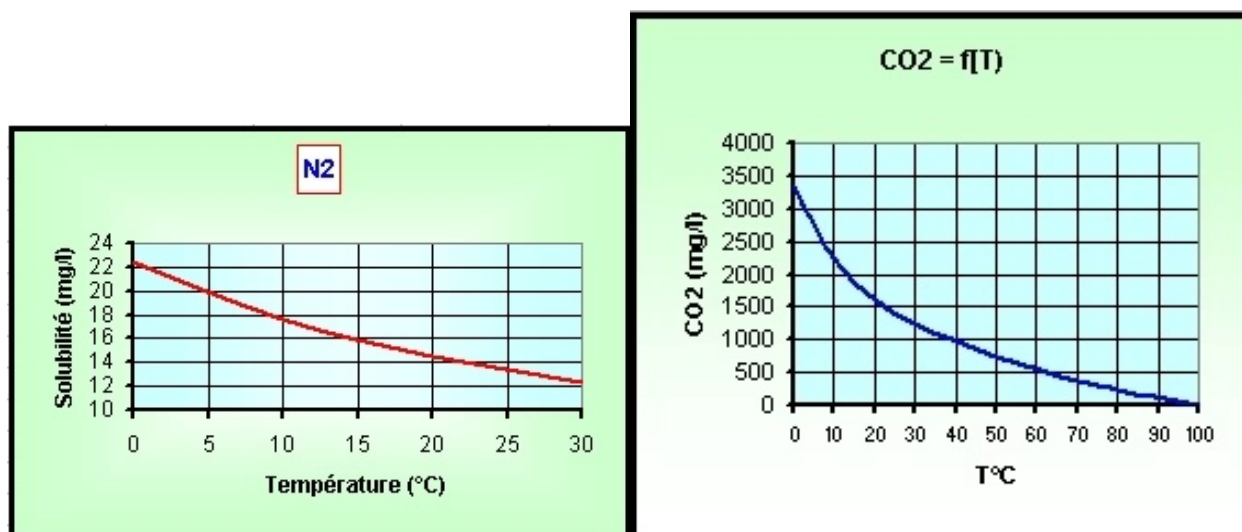


FIGURE 2.5: Solubilities of N_2 and CO_2 in water as functions of temperature.

formed by adding an appropriate amount of alcohol so that autoclave filling ratio reached 55 percent. $Ba(OH)_2 \cdot 8H_2O$ was added to get a 0.1 M concentration. 1.1 Ba/Ti molar ratio was attained by adding NTO, HTO or KTO powders and resulting mixture remained under continuous agitation for 30 minutes. After sealing autoclave, temperatures of 90°C, 100°C, 150°C, 200°C or 250°C were applied for 24 hours after a heating step. Cooling was followed by washing several times with deionized water until pH of filtrate was close to 7, redispersion in ethanol and drying in an oven at 70°C for 12 hours. All of these syntheses XRD patterns indicated production of Barium Titanate, even though some elements could be indexed with a cubic phase pattern corresponding to JCPDS card no. 31-0174 and others were a tetragonal phase pattern indexed by JCPDS card no. 05-0626. Relative weights of both phases lead to computation of a tetragonality parameter. A Parr instrument digestion vessel 4747 equipped with a pressure gauge, having volume 75 mL and no Teflon liner was employed to measure autogenous pressure at various temperatures and resulted in figure 2.6, and measurement were repeated with and without additional reagents including nanowire precursor and $Ba(OH)_2 \cdot 8H_2O$. Internal pressure did not seem to noticeably rise until temperatures exceeded 150°C. Obtained shapes below 150°C were predominantly aggregates that retained some of the precursor geometry. Syntheses performed at temperature above 150°C lead to well-separated shapes that can be described as totally independent from precursor. Size and shape of NTO and HTO precursors being quite similar, ionic radii of Na^+ and H_3O^+ being very close, titanium to sodium and titanium to proton ratio being identical, little difference was expected between low temperature products obtained with both reagents under solvothermal conditions. Tetragonality and average particle size obtained at all temperatures only for NTO and KTO are grouped in table 2.1. Even though only KTO precursor are hollow nanotubes from the start, HTO

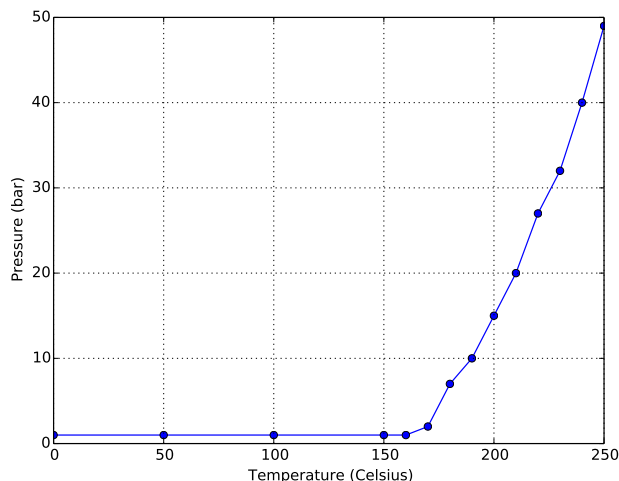


FIGURE 2.6: Pressure inside a solvothermal vessel filled at 55 percent with NTO and $\text{Ba}(\text{OH})_2 \cdot 8\text{H}_2\text{O}$ added to a water-ethanol mix at various temperatures.

	90°C	100°C	150°C	200°C	250°C
BT-NTO size (nm)	10-30	50-100	50-100	50-150	50-200
c/a	1.0013	1.0024	1.0048	1.0056	1.0062
BT-KTO size (nm)	—	100	100	100	100
c/a	—	1.0037	1.0056	1.0061	1.0065

TABLE 2.1: Sizes and tetragonalities of particles after solvothermal treatment of NTO or KTO precursors.

and KTO initially solid nanorod precursors can also be viewed as rapidly becoming hollow due to Kirkendall effect, as this will be discussed in depth in the next chapter. Lowest temperature synthesis performed with NTO precursors lead to nanospheres that were mostly keeping a trace from an original rod shape as one can check in figure 2.7 a. XRD diffraction peaks of HTO presented in figure 2.3 b2 were much broader than those of NTO and that indicates crystallinity of HTO to be lower than that of NTO. Such a difference did not affect products of solvothermal synthesis at low temperature as one could hardly detect differences between figure 2.7 a and figure 2.7 a1. Increasing temperature of solvothermal synthesis with NTO precursor to 100°C also lead to agglomerated nanospheres represented in figure 2.7 b. Little difference between NTO-synthesized figure 2.7 b and HTO-synthesized figure 2.7 b1 nano-objects was again observed. At a solvothermal temperature of 150°C, a fraction of obtained particles became detached from NTO precursor on a representative SEM image shown in figure 2.7 c. An absence of significant difference between results obtained with NTO and HTO at temperatures of 90°C, 100°C and 150°C (figure 2.7 c1) suggested to continue other syntheses only with one of the two precursors *i. e.* NTO. Syntheses at more than 150°C were not performed with HTO as results should be identical to NTO. XRD measurements of products coming from a synthesis using NTO were grouped top left corner of figure 2.8; a temperature of 90°C leads to peaks that were mostly those of cubic Barium Titanate. On increasing temperature to 150°C, (200) and (002) peaks became split and lead to indexation of

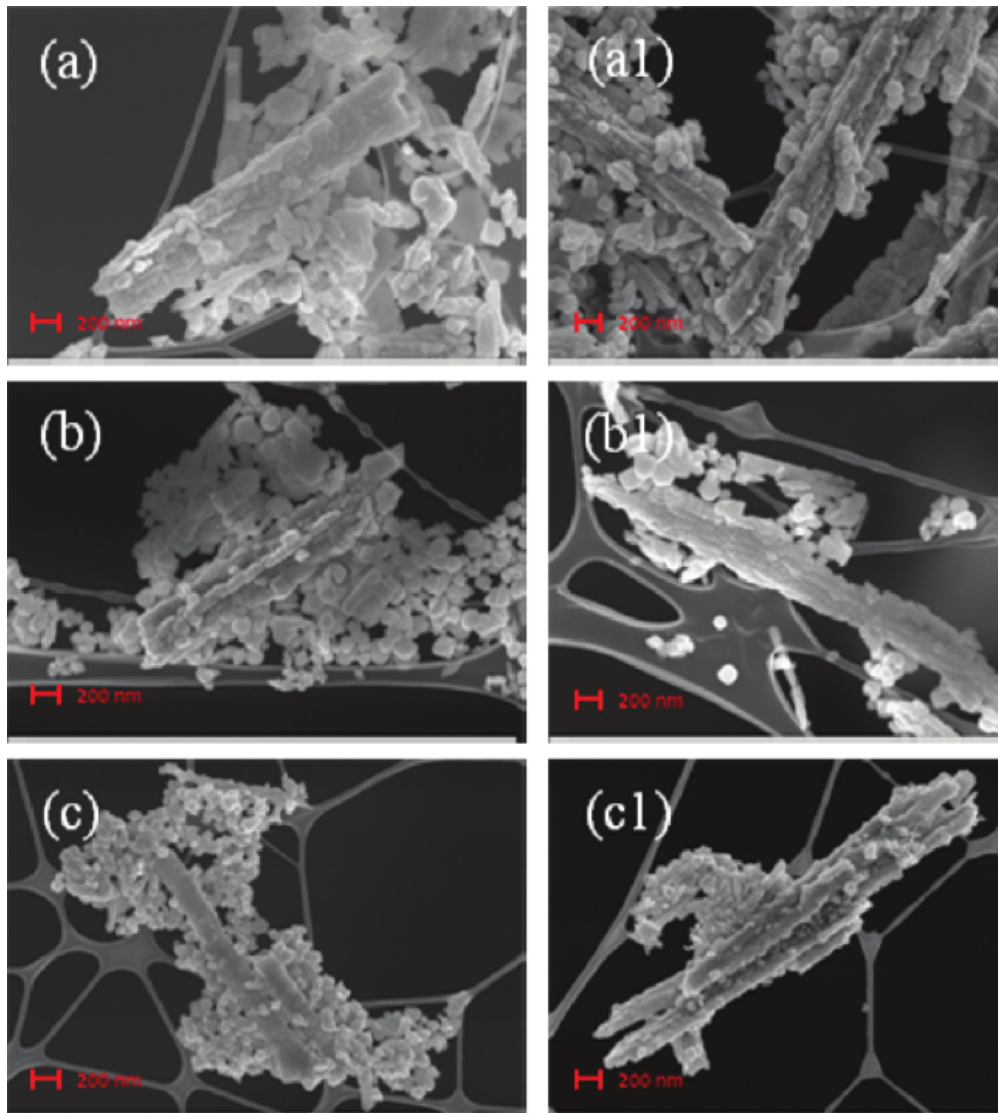


FIGURE 2.7: SEM observation of Barium Titanate products after solvothermal synthesis at 90°C, 100°C and 150°C from NTO (a, b, c) or HTO (a1, b1, c1) precursor.

corresponding diffractogram with a tetragonal phase as shown in the bottom of figure 2.8. Presence of hydroxyl defects favoured by low temperature syntheses may be a reason why a cubic structure gets stabilized and annealing probably suppresses this effect [41]. XRD measurements after a synthesis starting with HTO were grouped in top right corner of figure 2.8. As XRD peaks were recorded without any post-treatment, formation of a parasitic BaCO_3 phase is detected in products obtained from both NTO and HTO at 100°C. Less than 1% in mass of BaCO_3 was observed in XRD patterns of both products prepared at 150°C. BaCO_3 formation was minimized by higher reaction temperatures. Removing as much carbon dioxide CO_2 from solvent as possible was confirmed to be an important step. No difference between XRD patterns obtained with both precursors was observed after a redispersion in a 6% per unit volume CH_3COOH solution followed by filtration and washing with deionized water: BaCO_3 was completely removed.

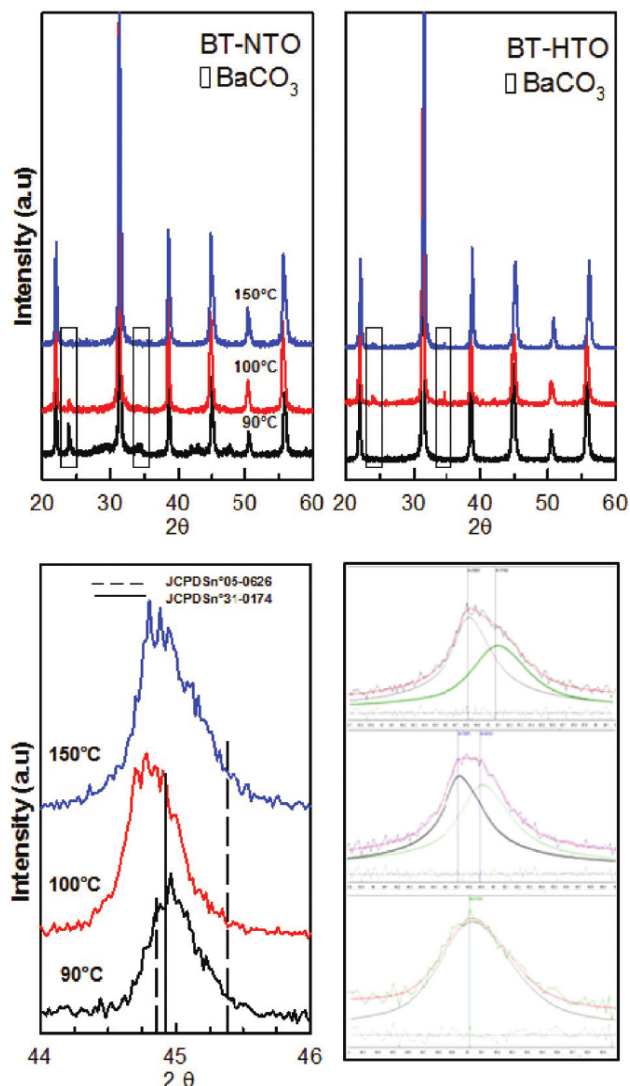


FIGURE 2.8: XRD patterns of BTO products obtained after solvothermal treatments of NTO (top left) or HTO (top right) at temperatures of 90°C, 100°C and 150°C. Zoom around 45° for NTO to observe (200) and (002) peaks (bottom left) and fit results (bottom right). The amount of BaCO_3 estimated from the XRD patterns obtained at 150°C is less than a percent.

Using KTO as precursor lead to product shapes that did not retain original nanotube morphology even at a synthesis temperature as low as 150°C as it can be checked in figure 2.9 a. Typical nanoparticle size was $\approx 50\text{nm}$ and a mix between isolated nanospheres and nanotori was observed. Shape of original precursor was again mostly lost and produced nanoparticles were free standing contrarily to those synthesized from NTO at 150°C that can be seen in figures 2.9 a and 2.9 a1. Titanium precursor composition thus modifies products of solvothermal syntheses. K/Ti molar ratio represents 1/3 in KTO whereas it is twice more in NTO *i. e.* 2/3. Topotactic ion exchange provides 1/6 of all Ba^{2+} in KTO and 1/3 in the case of NTO. Transformation from precursor structure to perovskite [42] could require insertion of more Ba^{2+} in a KTO case with

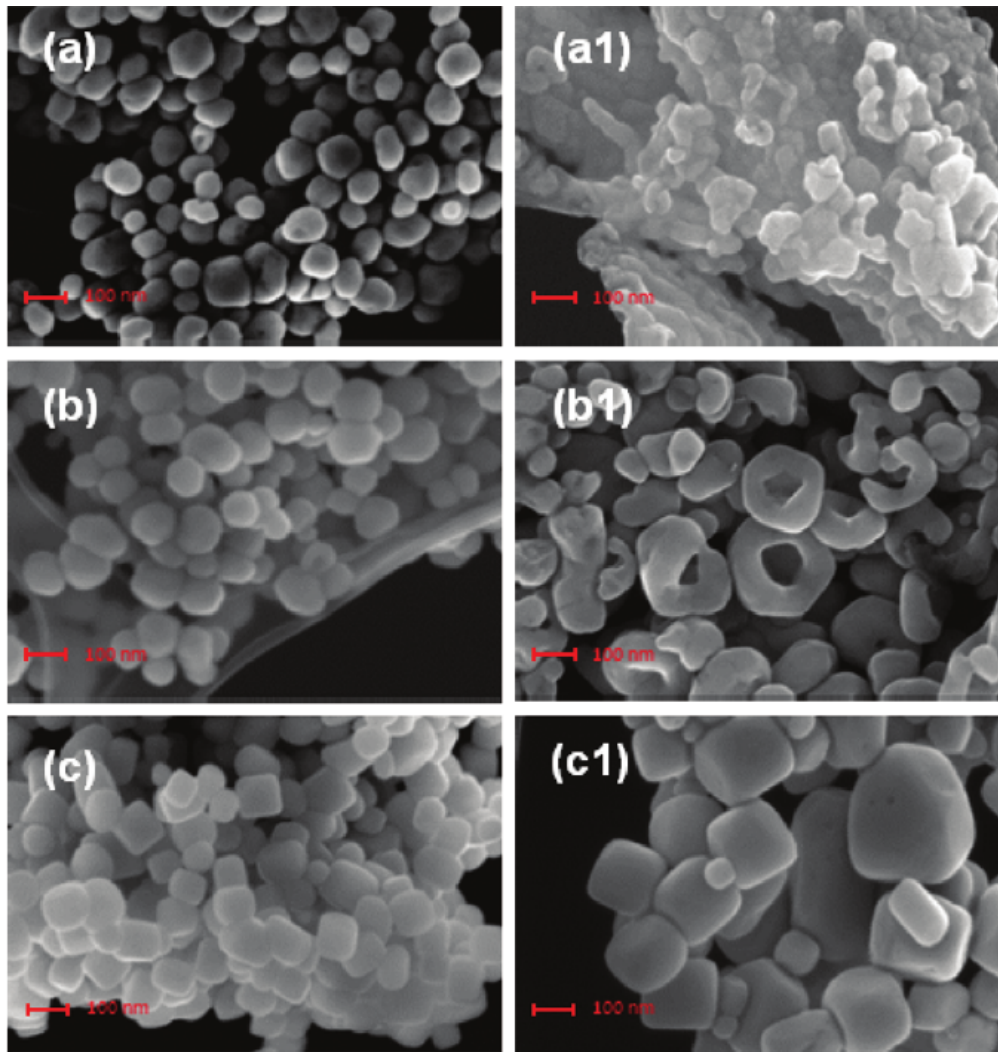


FIGURE 2.9: 150°C, 200°C and 250°C solvothermal syntheses products from KTO (a, b, c) or NTO (a1, b1, c1) precursor leading to SEM images of Barium Titanate independent nanospheres and nanotori.

respect to a NTO one and final product shapes can exhibit less similarity with precursor morphology. Increased synthesis temperatures also tend to grow independent particles. Individual nanospheres only as shown in figure 2.9 b were obtained after solvothermal treatment of KTO nanotubes at 200°C. Mean size was ≈ 100 nm. 200°C solvothermal treatment of NTO precursor lead to uniform nanotori that were never observed alone starting from KTO at any temperature: figure 2.9 b1 shows major diameters were in a 50-150 nm range. Single-crystallinity was verified on HRTEM image 2.10 and a closeup shown in figure 2.11 allowed measurement of lattice fringes spacing. A 0.4 nm interplanar distance distinguishes a (100) family of planes. No immediate relation can be established between NTO nanorods shape and resulting free standing nanotori [43, 44]. XRD patterns recorded for products obtained from KTO at all temperatures can be found in figure 2.12. Little amounts of BaCO_3 are observed in the case of nanotori and peaks of tetragonal Barium Titanate are pronounced, indicating presence of few OH defects compensated by Ba^{2+}

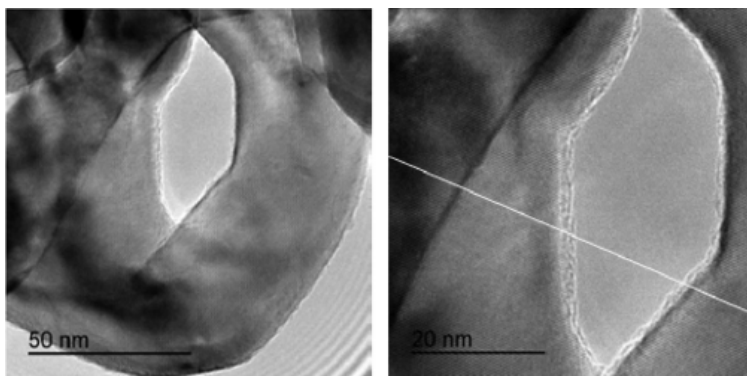


FIGURE 2.10: Barium Titanate nanotorus HRTEM observation. Alignment of atomic planes on both side of torus hole is shown by a white line.

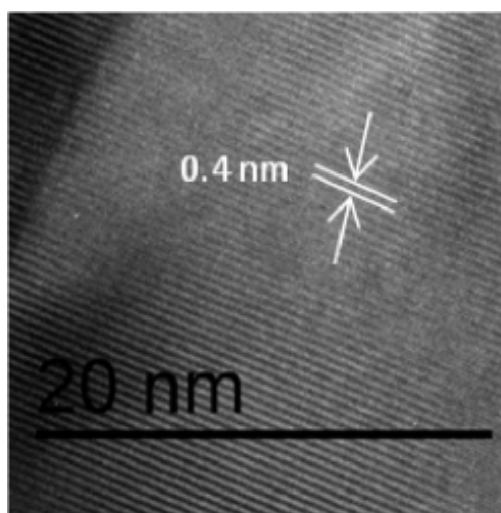


FIGURE 2.11: Barium Titanate nanotorus (100) atomic planes.

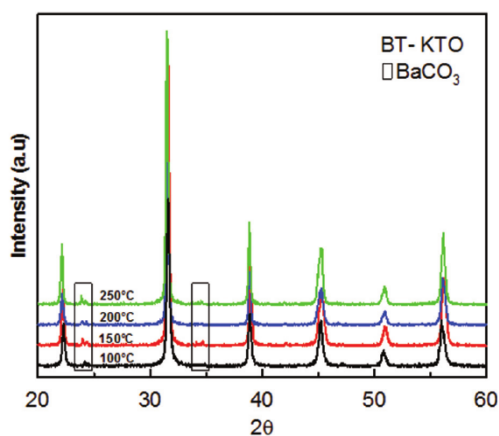


FIGURE 2.12: XRD patterns of products obtained from KTO powders after solvothermal treatments at various temperatures.

vacancies [45]. Syntheses performed from KTO precursor at a higher temperature of 250°C lead

to production of relatively monodisperse well-separated nanocubes that had typical sizes of ≈ 100 nm and can be viewed in figure 2.9 c. A similar temperature applied during a solvothermal synthesis starting with NTO precursor also produced independent nanocubes but size distribution was a little broader. Figure 2.9 c1 shows most nanoparticles dimensions were comprised in a 50 to 200 nm size range. Diffraction patterns recorded in figure 2.12 show a temperature increase does not completely remove BaCO_3 contamination, but tetragonality was increased again. Another

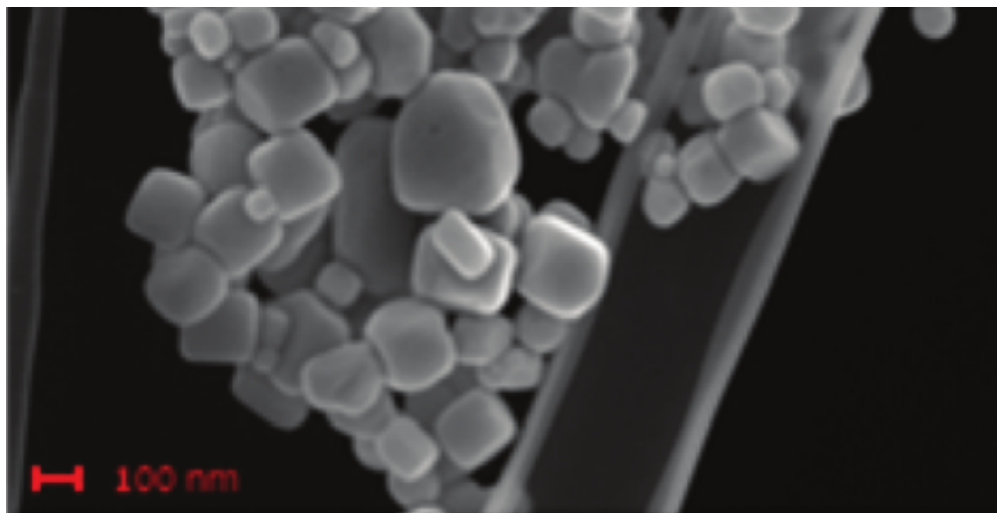


FIGURE 2.13: Polydispersity in SEM image of BTO individual nanocubes obtained after a 250°C solvothermal synthesis from NTO precursor with a Ba/Ti ratio of 1.1.

solvothermal synthesis performed with NTO precursor at a temperature of 250°C was conducted with nearly identical conditions with respect to those leading to figure 2.9 c1 and 2.13 apart from an increase in Ba/Ti molar ratio to 1.6 instead of 1.1 and more monodisperse particles shown in figure 2.14 were produced. Average size is close to ≈ 200 nm and an increase of separation between (200) and (002) peaks can be attributed to a less broad size distribution. As only a third of available barium sites are supplied by topotactic ion exchange with Sodium ions, increasing the concentration of Barium ions in solution may promote additional insertion and affect shape generation mechanisms.

2.3 Conclusion

An introduction to synthesis and characterization techniques utilized during experimental work was provided first. Experimentally, Barium Titanate is a mixed oxide which can be synthesized in several ways. The most common one involves a solid state reaction between Titanium Dioxide and Barium Oxide. As interdiffusion of ions in these phases requires high activation energies, reaction times are long and, at the temperatures of the syntheses, there is significant grain growth among reagents. Reactions taking place in solution often occur at lower temperatures

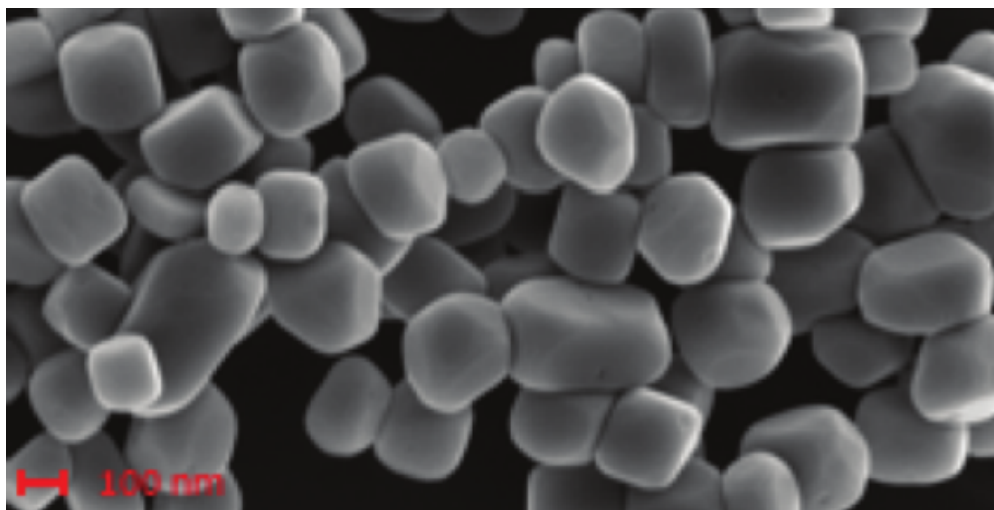


FIGURE 2.14: Monodispersity in SEM image of Barium Titanate individual nanocubes obtained after a 250°C solvothermal synthesis from NTO precursor with a Ba/Ti ratio of 1.6.

but the solvent boiling point often imposes a fundamental upper bound. In this work, solvothermal methods involved the use of a pressure vessel that allowed the reagents to be heated significantly above the boiling temperature of the solvent. Barium Titanate is produced without losing the nanometric size of reagents. Three types of syntheses were performed and resulted in three different titanium precursor nanorods or nanotubes, namely $\text{Na}_2\text{Ti}_3\text{O}_7$, $\alpha - \text{K}_2\text{Ti}_6\text{O}_{13}$ and $\text{H}_2\text{Ti}_3\text{O}_7$. A second solvothermal step allowed the cation associated to Titanium to diffuse out and be topotactically replaced by Barium. X-Ray diffraction confirmed that Barium Titanate was obtained and microscopy lead to observation of a broad variety of shapes among which agglomerated nanospheres, individual nanospheres, individual nanocubes, mixing of nanospheres and nanotori and individual nanotori can be cited. This variety of shapes provided inspiration for the numerical experiments: for instance, the chapter dealing with simulations performed on a perfectly isolated ferroelectric material torus will lead to prediction of new order parameter. Even though simulated shapes size are smaller than the experimentally produced ones, interaction between simulation and syntheses means the simulation results can possibly be tested by performing measurements on experimentally produced shapes. Analyzing mechanisms at play during generation of distinct geometries will be the focus of next chapter.

Chapter 3

Morphogenesis mechanisms

Contents

3.1 Nanospheres	65
3.2 Nanotori	66
3.3 Nanospheres and nanotori	71
3.4 Nanocubes	73
3.5 Conclusion	76

TWO step solvothermal syntheses of various Barium Titanate shapes including agglomerated or free standing nanospheres, nanotori and nanocubes were performed. Mechanisms proposed in [32] to explain growth of various geometries will be presented in more detail. Ostwald ripening [46] and Kirkendall effect [47] are often mentioned but neither can explain generation of torus-shaped particles. Additional characterization leads to distinction between solid and hollow nanoparticles.

3.1 Nanospheres

Precursor original shape was partly retained for syntheses conducted between 90°C and 150°C. A typical mechanism at play that explains particle size growth on increasing temperature is Ostwald ripening as illustrated in the top of figure 3.1. An energy difference is associated to particles depending on their size. Surface tension being inversely proportional to particle radius, a thermodynamically-driven elimination of small particles takes place which means "growth of large crystals from those of smaller size which have a higher solubility than the large ones"[48]. Simultaneous void formation also occurs all along ion-exchange between Na^+ or H_3O^+ and Ba^{2+} . In more details, Na^+ or H_3O^+ diffuse outwards a layered precursor nanorod structure [49] whereas Ba^{2+} diffuse inwards. Ionic radii of Ba^{2+} (1.35Å) being larger than that of Na^+ or H_3O^+ (1.00Å) rate of inward diffusion of Barium has to be slower than rate of outward diffusion. Furthermore, ionic replacements throughout solid crystalline structure are dominated by motion of vacancies rather than direct interchange of ions [50]. A relatively high rate of vacancies production can thus be reached at the solid-liquid interface and aggregation of vacancies can then lead to nucleation of voids inside precursor nanorods that become hollow nanotubes through a so-called Kirkendall

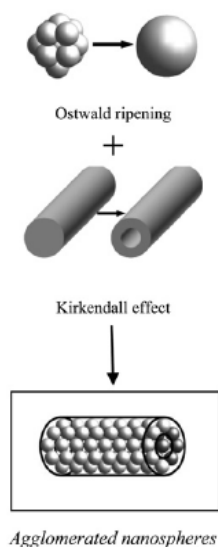


FIGURE 3.1: Barium Titanate nanoparticles morphogenesis processes at play in the NTO route between 90°C and 150°C.

effect. Both Ostwald ripening and Kirkendall effect can be invoked [51] to justify the growth of agglomerated nanospheres [52] all along the surface of a hollow nanotube as observed in figure 3.2.

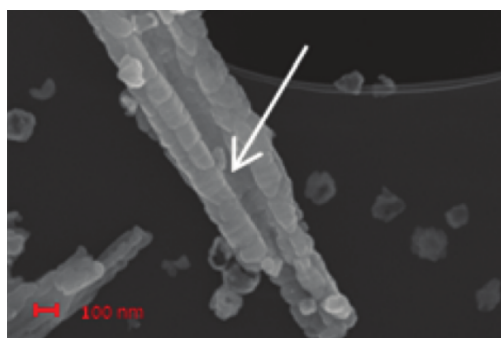


FIGURE 3.2: SEM image after treatment of NTO solid nanorod precursor for 24h at 150°C of a hollow (white arrow) nanotube made of agglomerated nanospheres.

3.2 Nanotori

Hydrothermal synthesis of Barium Titanate shapes bearing some similarity with tori was reported by Habib *et al.* [53] starting from $\text{Ba}(\text{OH})_2 \cdot 8\text{H}_2\text{O}$ and TiO_2 after 24 hours at 150°C. Hydrothermal synthesis of Barium Titanate so-called bowl-like nanoparticles was also reported by Deng *et al.* [54]. A careful synthesis of Titanium Dioxide precursor complex shapes lead to solvothermal growth of Barium Titanate nanotori in a study conducted by Xia *et al.* [55] and had results that depended on reaction time. Influence of Nd doping was studied by Lin *et al.* [56]. An aggregation-realignment-fusion mechanism was suggested to produce ring-like Barium Titanate objects after

a sol-gel hydrothermal synthesis conducted by Yang *et al.* [57]. Lastly, hydrothermal synthesis starting from NTO nanotubes and BaCl_2 produced torus-like particles and Kirkendall effect was discussed by Maxim *et al.* [58]. At 200°C , obtained nanotori were observed with SEM (figure 2.9 b1) and TEM (figure 2.10) to show that atomic planes were apparently neither bent around tori nor following radial structures. A mechanism leading to formation of nanotori from a nanotube splitting to slices perpendicular to its direction [59] thus had to be ruled out. Another process had to be invoked : atomic planes orientation suggested formation of nanotori took place along a nanotube direction such as in figure 3.3 rather than perpendicularly to it. Equations leading

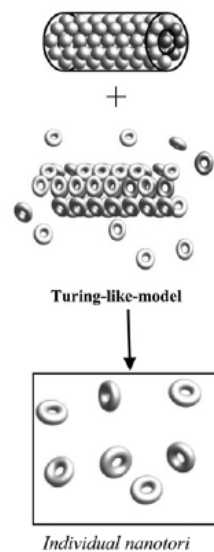


FIGURE 3.3: Barium Titanate nanoparticles morphogenesis processes at play in the NTO route at 200°C .

to ring-shaped geometries that can account for production of nanotori along nanotube surface will be presented thereafter. Diversity of animal fur patterns originally lead Turing into studying symmetry breaking morphogenesis processes in two-dimensional systems that have diffusion as a leading transport mechanism [60]. A minimal set of equations was written and described production of complex spatially modulated structures. Interaction between a chemical reaction kinetics and diffusion lead to so-called stationary patterns also known as Turing structures. Two compounds have to be involved in a minimal reaction-diffusion system. Increasing concentration of first compound must increase both species production rates and increasing concentration of second compound must decrease production rates, with a first compound diffusing much faster than a second one. During morphogenesis of nanotori, two quantities computed all around a nanotube surface can be mapped on described concentrations of two compounds. Concentration of barium ions on the one hand and concentration of vacancies linearly combined with concentration of barium ions on the other hand were shown to obey a system of reaction-diffusion equations bearing similarities with Turing model system. A mere periodic boundary condition on one direction of a plane can describe a nanotube geometry [61]: results obtained through simulations of original Turing model without this periodic boundary condition are probably not very different from those

with it. Particular shapes obtained on simulating Turing set of equations and represented in figure 3.4 and may explain formation of torus structures all along the nanotube axis provided that similar equations control evolution of relevant quantities. All variables used in subsequent computations

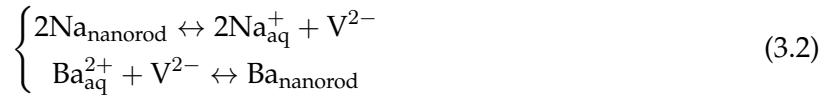


FIGURE 3.4: Representative Turing pattern wrapped around a nanotube geometry with a periodic boundary condition along direction x .

of this chapter were constrained to evolve in a two-dimensional space through averaging along nanotube thickness e : any quantity f stands for its average f_{av} defined in equation 3.1.

$$f_{av}(x, y) = \frac{1}{e} \int f(x, y, z) dz \quad (3.1)$$

Variations of f_{av} contained in an xy plane representing a nanotube surface give rise to diffusion processes tending to smear them. Additional exchanges with the aqueous medium surrounding the nanotube can occur simultaneously along the z direction that is perpendicular to nanotube external surface. Focusing on NTO precursor makes it possible to write chemical equilibrium at play during topotactic ion exchange (3.2) and subsequent calculations can also be performed for HTO or KTO precursor.



Thickness-averaged concentration of Sodium cations $n(x, y)$, Barium cations $b(x, y)$ and vacancies $v(x, y)$ formed a set of variables and an additional assumption was made by taking dissolved aqueous species concentration to remain constant during all experiment. Reaction rates were assumed to be proportional to reagent concentrations. As an example, rate of Barium cation insertion determined from equation 3.2 is proportional to vacancies concentration v times barium ions concentration in solution. Quantity of Barium ions in solution being much larger than that of inserted ions, it can be assumed not to evolve during all the synthesis and be included in reaction constant prefactor so that its contribution to the time derivative of b in equation 3.3 merely writes k_3v . An additional fourth relation in equation 3.3 deals with concentration of Titanium ions

c_0 : it states that one Titanium cation per Barium atom forms BaTiO_3 and one and a half Titanium cation are required per Sodium atom in $\text{Na}_2\text{Ti}_3\text{O}_7$ so that subtracting appropriate quantities gives another expression of the amount of cation vacancies v involved in ion-exchange.

$$\left\{ \begin{array}{l} \frac{\partial n}{\partial t} = -2k_1n^2 + 2k_2v + D_1\Delta n \\ \frac{\partial v}{\partial t} = k_1n^2 - (k_2 + k_3)v + k_4b + D_2\Delta v \\ \frac{\partial b}{\partial t} = k_3v - k_4b + D_3\Delta b \\ v = c_0 - (3/2)n - b \end{array} \right. \quad (3.3)$$

All three variables have to remain positive and saturation mechanisms avoid divergence of any of them. Even in the absence of any vacancy, Sodium and Barium quantities are limited by the amount of available Titanium ions. Moreover, a critical concentration of vacancies gives rise to precipitation *i.e.* nucleation of voids.

In more details, using a time derivative of last element of equation 3.3 to rewrite the second one leads to equation 3.4.

$$\left\{ \begin{array}{l} \frac{3}{2} \frac{\partial n}{\partial t} = -\frac{\partial b}{\partial t} - \frac{\partial v}{\partial t} = -3k_1n^2 + 3k_2v + \frac{3}{2}D_1\Delta n \\ \frac{\partial v}{\partial t} = k_1n^2 - (k_2 + k_3)v + k_4b + D_2\Delta v \\ \frac{\partial b}{\partial t} = k_3v - k_4b + D_3\Delta b \\ (3/2)n = c_0 - v - b \end{array} \right. \quad (3.4)$$

Right hand sides of second and third equation were combined with Laplacian of the fourth to write equation 3.5.

$$\left\{ \begin{array}{l} -k_1n^2 + k_2v - D_2\Delta v - D_3\Delta b = -3k_1n^2 + 3k_2v - D_1\Delta b - D_1\Delta v \\ \frac{\partial v}{\partial t} = k_1n^2 - (k_2 + k_3)v + k_4b + D_2\Delta v \\ \frac{\partial b}{\partial t} = k_3v - k_4b + D_3\Delta b \\ (3/2)n = c_0 - v - b \end{array} \right. \quad (3.5)$$

Isolating a $2k_1n^2$ term, substituting its expression and multiplying second and third equations respectively by $2(3D_2 - D_1 - 2D_3)$ and $2(D_3 - D_1)$ leads to equation 3.6.

$$\left\{ \begin{array}{l} 2k_1n^2 = 2k_2v + (D_2 - D_1)\Delta v + (D_3 - D_1)\Delta b \\ 2(3D_2 - D_1 - 2D_3)\frac{\partial v}{\partial t} = (3D_2 - D_1 - 2D_3)[(3D_2 - D_1)\Delta v + (D_3 - D_1)\Delta b - 2k_3v + 2k_4b] \\ 2(D_3 - D_1)\frac{\partial b}{\partial t} = 2(D_3 - D_1)D_3\Delta b + 2(D_3 - D_1)k_3v - 2(D_3 - D_1)k_4b + \\ (3/2)n = c_0 - v - b \end{array} \right. \quad (3.6)$$

Summing a third equation to a second one and performing a change of variable $X = (6D_2 - 2D_1 - 4D_3)v + (2D_3 - 2D_1)b$ gives equation 3.7.

$$\left\{ \begin{array}{l} 2k_1n^2 = 2k_2v + (D_2 - D_1)\Delta v + (D_3 - D_1)\Delta b \\ \frac{\partial X}{\partial t} = \frac{3D_2 - D_1}{2}\Delta X + k_3\frac{3D_3 - 3D_2}{3D_2 - D_1 - 2D_3}X + 2(3D_2 - 3D_3)\left[k_4 + k_3\frac{D_3 - D_1}{3D_2 - D_1 - 2D_3}\right]b \\ \frac{\partial b}{\partial t} = D_3\Delta b + \frac{k_3}{6D_2 - 2D_1 - 4D_3}X + \left[\frac{2D_1 - 2D_3}{6D_2 - 2D_1 - 4D_3} - k_4\right]b \\ (3/2)n = c_0 - v - b \end{array} \right. \quad (3.7)$$

Second and third equations allow term by term identification with Turing reaction diffusion minimal system [60] reproduced in equation 3.8.

$$\left\{ \begin{array}{l} \frac{\partial X}{\partial t} = a_1\Delta X + a_2X + a_3b \\ \frac{\partial b}{\partial t} = a_4\Delta b + a_5X + a_6b \end{array} \right. \quad (3.8)$$

Values of coefficient are given in equation 3.9.

$$\left\{ \begin{array}{l} a_1 = \frac{3D_2 - D_1}{2} \\ a_2 = k_3\frac{3D_3 - 3D_2}{3D_2 - D_1 - 2D_3} \\ a_3 = 2(3D_2 - 3D_3)\left[k_4 + k_3\frac{D_3 - D_1}{3D_2 - D_1 - 2D_3}\right] \\ a_4 = D_3 \\ a_5 = \frac{k_3}{6D_2 - 2D_1 - 4D_3} \\ a_6 = \frac{2D_1 - 2D_3}{6D_2 - 2D_1 - 4D_3} - k_4 \end{array} \right. \quad (3.9)$$

Figure 3.4 was obtained as a secondary pattern after simulating a model described by equation 3.8 with an initial condition that was called a primary pattern. In more detail, the evolution in the course of a reaction-diffusion simulation run with a code used by Kondo *et al.* [62] under no periodic boundary conditions is reproduced in figure 3.5. Nanorod conversion to nanotube

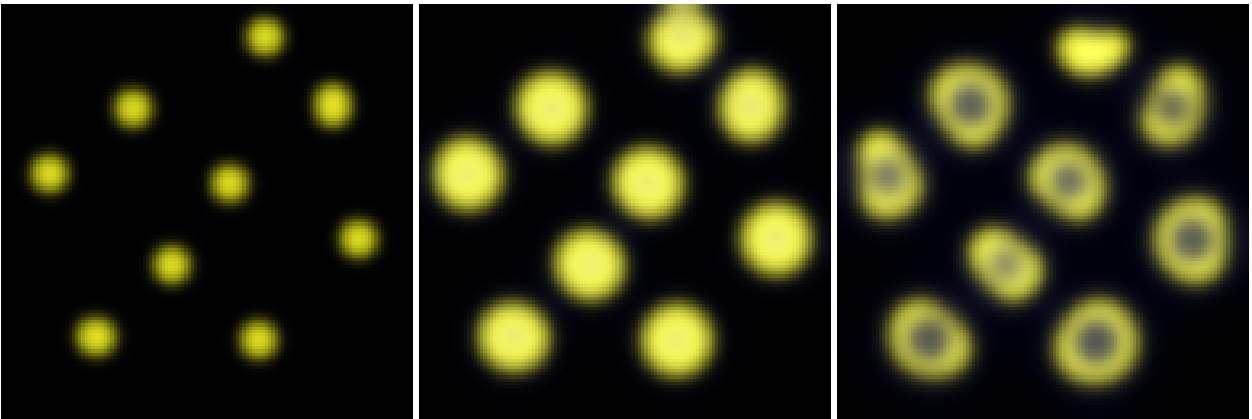


FIGURE 3.5: Initial condition, pattern obtained at the middle of a simulation and final state exhibiting ring-shaped patterns in a reaction-diffusion simulation.

and formation of such a primary pattern may occur during solvothermal heating ramp, and a

reaction-diffusion model leading to formation of ring-like patterns describes remaining constant temperature time. As the model is assumed to be valid on the precursor nanotube surface, ring-shaped patterns obtained at the simulation end are assimilated to generation of nanotori, whereas stability of disks would represent generation of spheres and a presence of both could hint at production of a mixture of nanospheres and nanotori. Depending on the values of reaction-diffusion coefficients which are probably a function of synthesis temperature, this same model could describe several reaction products. However, one of the hypotheses was to rely on a description that only computes averages over nanotube thickness: it leads this model into only predicting generation of solid shapes and other mechanisms will be invoked later to describe production of hollow shapes.

3.3 Nanospheres and nanotori

Low temperature syntheses performed with KTO precursor did not lead to uniform particle morphology as shown in figure 3.6. Products were individual BT objects with typical sizes comprised

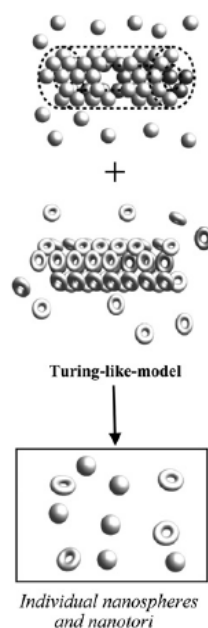


FIGURE 3.6: Barium Titanate nanoparticles morphogenesis processes at play in the KTO route between 90°C and 150°C.

between 50 nm and 100 nm whereas original KTO nanotube precursor diameter did not exceed 30 nm. Splitting into smaller sized products like in NTO may not be the only mechanism to be mentioned. Contrarily to ion-exchange involving Sodium and Barium, ionic radii of K^+ and Ba^{2+} being respectively 1.33 Å and 1.35 Å are not very different and outward diffusion of K^+ is as favoured as inward diffusion of Ba^{2+} , even though presence of more dissolved Ba^{2+} leads to a higher rate of insertion. KTO precursor nanotube interior is empty from the start and typical lengths (1 μm) and diameters (30 nm) are smaller than NTO ones by a factor of ten. Equivalent

quantities of Titanium ions in each KTO precursor nanotube are inferior to those present in NTO nanorods. All available sites become filled faster and temperatures required to form independent particles are lower. Increasing synthesis temperature with KTO precursor leads to another sequence of shapes that is essentially due to a difference between insertion of Ba^{2+} and outward diffusion rates of Na^+ and K^+ . For KTO, a mix of nanospheres due to Ostwald ripening and Kirkendall effect coexist with nanotori that were attributed to a Turing reaction-diffusion mechanism and obtained alone in the case of NTO precursor. NTO precursor being bigger, nanotori alone was expected from KTO precursor at lower temperatures but obtention of these objects was hindered by diversity of KTO precursor sizes. Additional images of spherical nanoparticles resulting from a

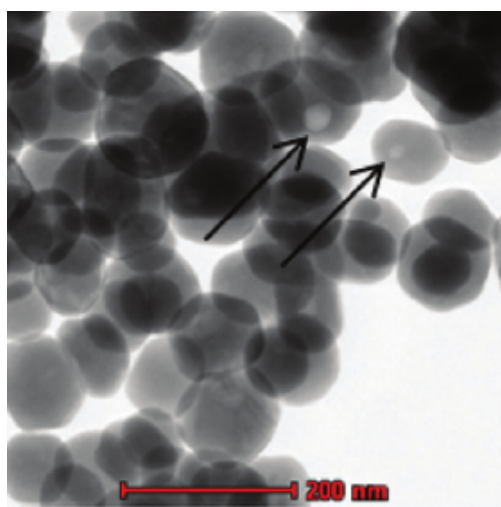


FIGURE 3.7: Holes inside BT spheres obtained from KTO are highlighted by black arrows in a STEM-ABF observation.

solvothermal synthesis at 200°C were obtained with STEM-ABF (Annular Bright Field) in figures 3.7 and 3.8. SEM observation alone performed on obtained nanospheres such as those of figure 2.9 b did not evidence hollow shapes. To the best of our knowledge, nanospheres of Barium Titanate were always assumed to be solid. However, hollow nanoparticles made of other materials including SiO_2 , TiO_2 and CoSe were reported to be produced after a variety of self-templating processes such as surface-protected etching, Ostwald ripening, Kirkendall effect and galvanic replacement [48]. Growth of obtained hollow nanospheres cannot be explained by a combination of these processes and a so-called self-rebuilding process had to be invoked. Particle size did not seem to vary much during transformation into sphere which corresponds with a shape transformation involving one particle itself and some of the nanotori holes were preserved, as could be checked on figure 2.9 a representing products after a 150°C heating step.

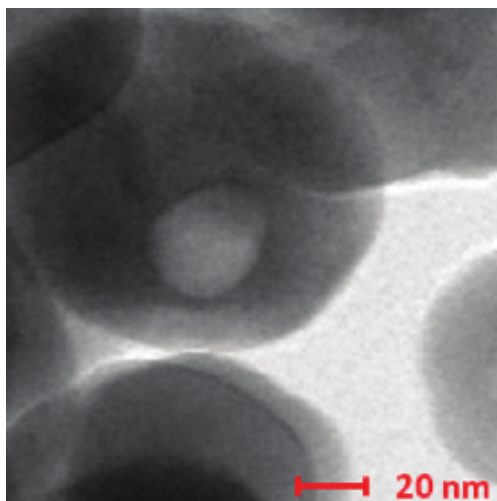


FIGURE 3.8: Closeup on a STEM-ABF observation of hollow nanometric BT spheres obtained from KTO.

3.4 Nanocubes

High temperature 250°C syntheses performed with KTO and NTO precursors both lead to similar shapes. As nanospheres proved to be hollow, nanocubes produced by the two synthesis methods were observed with STEM-HAADF (High Angle Annular Dark Field). Images with suffi-

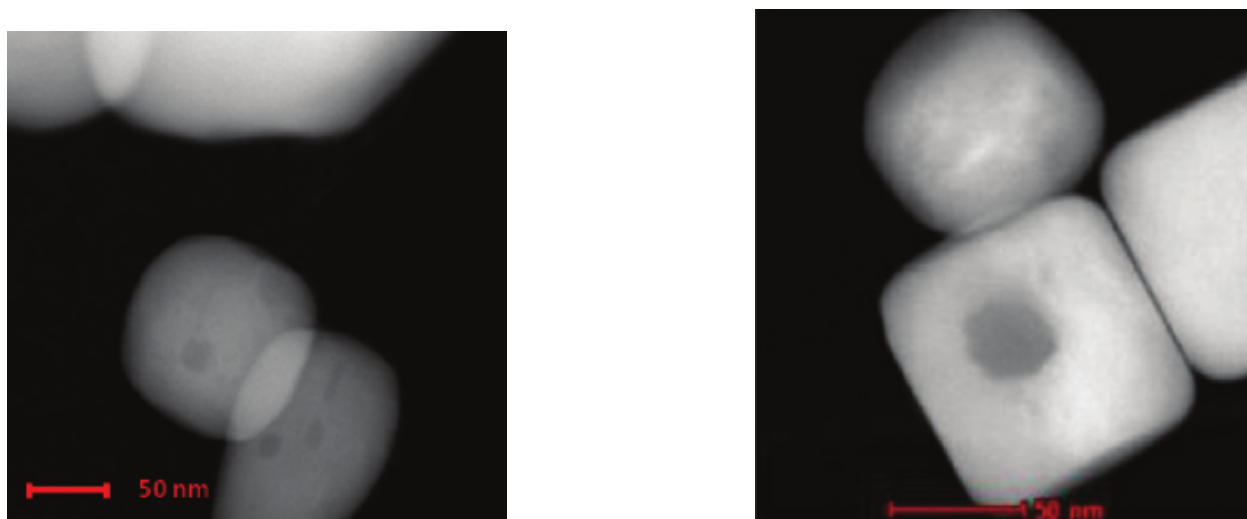


FIGURE 3.9: Holes inside cubes obtained from NTO (left) and KTO (right) in a STEM-HAADF observation.

cient contrast obtained with such a technique were obtained and, among solid nanocubes having rounded edges, a minority of hollow nanocubes was observed in figures 3.9. No prior report of Barium Titanate hollow nanocubes existed but CeO_2 and CaTiO_3 were described by Zhou *et al.* [63, 64] to undergo a Reversed Crystal Growth Route during solvothermal treatment to also produce hollow nanocubes. Creation of these shapes was attributed to aggregation dominating

individual particle growth followed by surface recrystallization of agglomerates. For zeolites, individual particles with characteristic sizes around 20 nm form discus-shaped clusters 200-400nm thick and having diameters around 1-2 μ m. However, metallic precursor *i.e.* titanium was a solid state product in Barium Titanate syntheses contrary to other routes leading to hollow nanocubes [63]. Regarding products of syntheses beginning with NTO precursor, growth of individual nanotori after a solvothermal temperature of 200°C was reported before and increasing temperature to 250°C lead to hollow nanocubes. Size of hollow nanocubes strongly suggests that they were initially made of several nanotori: footprint of nanotori has characteristic size close to dimensions of nanocube surfaces but nanotori height is much smaller than that of a nanocube. A mechanism different from Reverse Crystal Growth, Kirkendall effect and Ostwald ripening had to be suggested. Due to the process of fusion of several nanotori followed by reconstruction of planar surfaces, merging-rebuilding seems to be an appropriate description as shown in figure 3.10. Evidence of

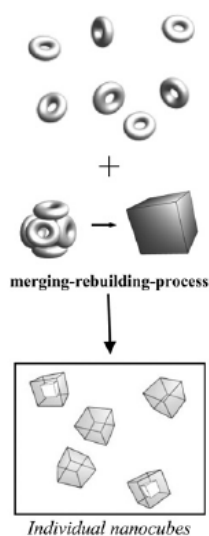


FIGURE 3.10: Barium Titanate nanoparticles morphogenesis processes at play in the NTO route at 250°C.

a reconstruction process was provided by observation of shapes produced between temperatures of 200°C leading to nanotori and 250°C resulting in nanocubes. Partially merged Barium Titanate nanotori reproduced in figure 3.11 were obtained at 225°C. Such a shape brings support to existence of a merging-rebuilding mechanism transforming nanotori into hollow nanocubes. Only nanocubes having no more than one hole were observed and location of the hole was systematically at the center of each nanocube. Open and closed porosity in sintered ceramics undergo similar transformations: voids resulting from agglomeration of isolated tori are gradually removed all along solvothermal treatment. Open porosity disappears first during heat treatment of a ceramic and observed solvothermally obtained nanocubes do not have holes reaching surfaces. A hole trapped at the center of particle can remain like closed porosity in ceramics. Due to rarity of hole trapping at the center of a nanocube, a majority of solid elements is obtained. Focusing on products obtained with a KTO precursor, hollow nanocubes obtained after solvothermal synthesis

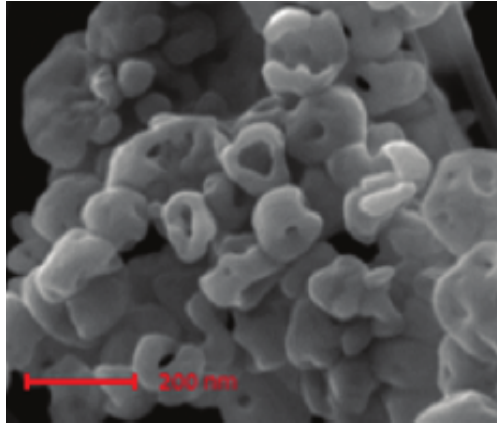


FIGURE 3.11: Partially merged Barium Titanate nanotori obtained from NTO after a solvothermal treatment at 225°C.

at 250°C replaced hollow nanospheres obtained at 200°C. Size differences between particles obtained at those two temperatures represented in figure 2.9 b and 2.9 c can be neglected. Increasing temperature makes one nanotorus transform into one nanosphere that gives rise to one nanocube and the whole process could be described as self-rebuilding without merging of independent particles as in figure 3.12. A mix of solid and hollow nanocubes is obtained for reasons similar to

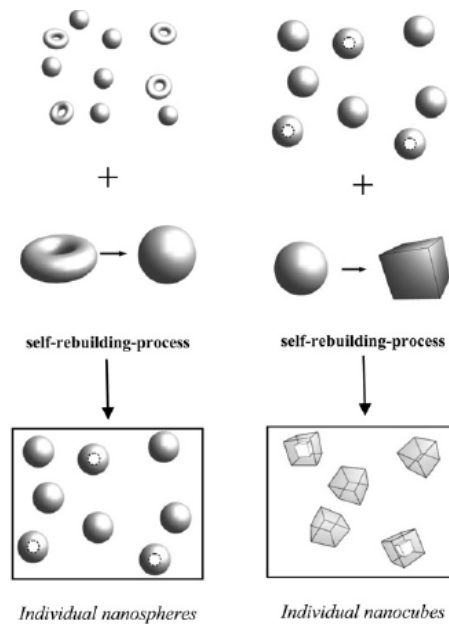


FIGURE 3.12: Barium Titanate nanoparticles morphogenesis processes at play in the KTO route at 200°C (left) and 250°C (right).

those given for NTO.

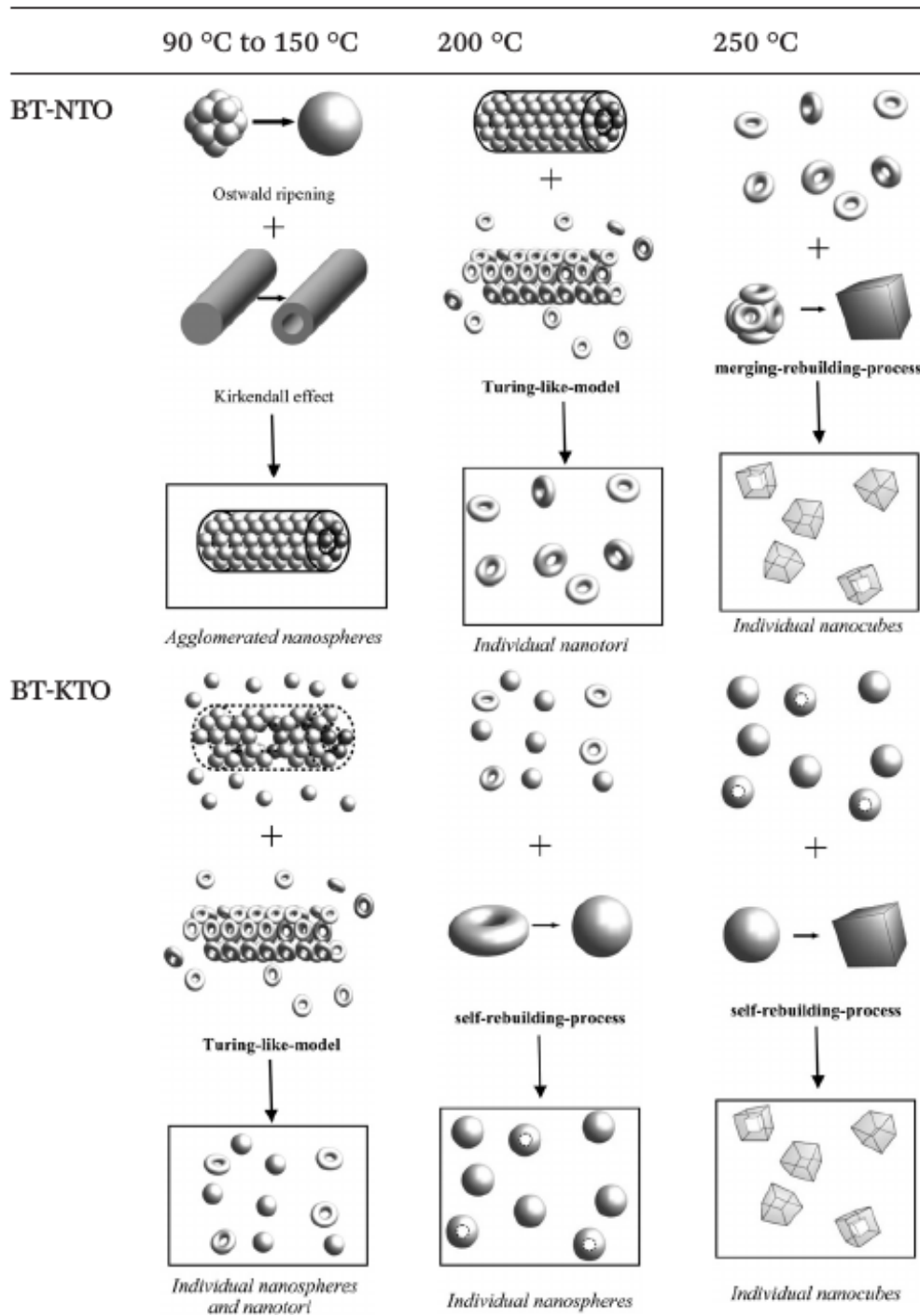


FIGURE 3.13: Summary of Barium Titanate nanoparticles morphogenesis processes.

3.5 Conclusion

Figure 3.13 sums up the growth processes of particles from two types of precursors at different solvothermal synthesis temperature: several nanostructures of single crystalline Barium Titanate were shown to arise and mechanisms leading to nanospheres were described first. Even though

the characteristic sizes remained of the same order of magnitude, the geometry of obtained particles sometimes had no resemblance with that of reagents. A microscope study shows that synthesis temperature dramatically alters obtained results: smaller particles appear on the surface of precursor and preserve overall shape for low temperatures, whereas higher temperatures favor growth of individual particles. Synthesis of nanotori alone was reported afterwards. Transmission Electron Microscopy allowed observation of atomic planes and established that in this original geometry, atomic planes are not concentric and the crystal structure is unstrained. Combined synthesis of nanospheres and nanotori was mentioned before focus moved on to nanocubes. Regarding these nanocubes, Transmission Electron Microscopy revealed that some of them can be hollow. Precursor type, temperature and Ba/Ti molar ratio were shown to jointly control final product shape. Classical growth mechanisms were cited to justify some obtained shapes: Ostwald ripening tended to favour large spherically shaped particles so as to minimize surface tension. For nanorods, Kirkendall effect described faster outward migration of an exiting cation than inward diffusion of Barium. As a result, vacancies were produced and merged at the core of the nanorod to transform it into a nanotube. Turing reaction-diffusion model was adapted to a nanotube precursor so as to justify production of nanotori before self-rebuilding and merging-rebuilding processes were proposed.

Chapter 4

Towards more complex order parameters in inhomogeneous materials

Contents

4.1 Description of charge distributions	79
4.1.1 Multipolar expansion	80
4.1.2 Rearranging into sets of terms stable versus rotations	81
4.2 Electrostatic interaction in inhomogeneous background permittivity	83
4.2.1 Inhomogeneous permittivity without periodic boundary conditions	84
4.2.2 Inhomogeneous permittivity with periodic boundary conditions	85
4.3 Conclusion	86

EVEN though several order parameters have been evidenced by previous studies and a method for computing dipole-dipole interaction was presented, this chapter will concentrate on these points. In a first section, we will deal with the order parameters that allow to describe a distribution of charge: we will go beyond multipolar expansion and show the role of a $(n-1)$ -th power of position-polarization tensor. Sets of components of this tensor that are invariant under a rotation of the coordinate system will be formed and will be shown to have the same expression as toroidal and hypertoroidal moments. In a second section, we will present steps towards extending the dipole-dipole interaction computation to a medium that does not have homogeneous background permittivity: a modification of Poisson equation is expected due to permittivity value being space-dependent and a method will be presented for computing the intersite interaction term in periodic boundary conditions.

4.1 Description of charge distributions

The field corresponding to any charge distribution created by an ensemble of dipoles as a function of powers of distance to origin can be described in a versatile and general formalism with elements from the mathematical preliminary of previous chapter. In this work, a description of multipolar expansion for an ensemble of dipoles will be provided and its term will be grouped into the sets of tensor components that are invariant under rotations.

4.1.1 Multipolar expansion

Multipolar moments are coefficients appearing on performing a serial expansion of a potential that is usually expressed as a function of powers of distance to origin and angle. Such an expansion provides an in principle exact description of the original potential. The zero-th order term of the expansion is called monopolar, first order is dipolar, third and fourth respectively are quadrupolar and octupolar. Multipolar moments represent an orthogonal basis for decomposing a potential function with the response of a field to presence of potential sources brought infinitely close one to the other. Various geometrical arrangements are possible and can be represented by directional derivatives.

In spherical coordinates, the special case of any field deriving from a potential and having a homogeneously vanishing monopolar term leads to Laplace equation, which has a basis of solutions made of a product between a radial part and spherical harmonics with multipolar moments being the prefactors.

Fields deriving from a potential can be approximated by a finite number of multipolar moments and exactly reproduced with an infinite one. Truncation after dipole term often represents a crude first guess in the special case of a localized distribution of charge but linear combinations of solutions obtained at any given order allow approximation with desired accuracy. Yet, not all three dimensional vector fields derive from a potential and are entirely described by monopolar, dipolar and higher order terms. According to Dubovik *et al.* [65], electromagnetic properties of exotic magnetic ordering along a small torus were considered by Zel'Dovich [66] as soon as the end of the fifties. Various toroidal moments then had to be introduced to describe the curl of the vector field in addition to the expansion of its potential part in multipolar moments/spherical harmonics.

Several derivations could be mentioned [67] even though assuming a non-solenoidal polarization vector field, bearing in mind a vacuum electrostatics case, sometimes leads to overlooking the terms corresponding to the rotational that will be shown in the rearranging into sets of terms stable versus rotations.

Expression of charge density Using the definition of a delta function leads to equation 4.1.

$$\rho(\mathbf{r}) = \int \rho(\boldsymbol{\xi}) \delta(\boldsymbol{\xi} - \mathbf{r}) d^3\xi \quad (4.1)$$

Delta expansion Writing value of a delta function at any point $\boldsymbol{\xi} - \mathbf{r}$ as a sum of its derivatives at point \mathbf{r} , in a generalization of equation 1.1, leads to equation 4.2.

$$\delta(\boldsymbol{\xi} - \mathbf{r}) = \sum_{n=0}^{\infty} \frac{(-1)^n}{n!} \underbrace{(\xi - r)_{\alpha} \cdots (\xi - r)_{\kappa}}_n \partial_{\alpha} \cdots \partial_{\kappa} \delta(\mathbf{r}) = \sum_{n=0}^{\infty} \frac{(-1)^n}{n!} \underbrace{\xi_{\alpha} \cdots \xi_{\kappa}}_n \partial_{\alpha} \cdots \partial_{\kappa} \delta(\mathbf{r}) \quad (4.2)$$

Conversion into discrete summation of moments Inserting equation 4.2 in an integral description of charge 4.1 leads to a decomposition into a sum presented in equation 4.3.

$$\rho(\mathbf{r}) = \sum_{n=0}^{\infty} \frac{(-1)^n}{n!} \partial_{\alpha} \cdots \partial_{\kappa} \delta(\mathbf{r}) \int \rho(\boldsymbol{\xi}) \xi_{\alpha} \cdots \xi_{\kappa} d^3\xi \quad (4.3)$$

Charge distribution consisting of point-like dipoles Last part of the summation in the right-hand side of equation 4.3 contains an n-th power of position-charge tensor. On dealing with a simulation supercell containing no charges but only point-like dipoles of magnitude \mathbf{p}_i located on sites i , the integral over space of charge density $\int \rho(\boldsymbol{\xi}) d^3\xi$ necessarily cancels and one can assume that the charge distribution writes as in equation 4.4.

$$\rho(\mathbf{r}) = \sum_{i,\alpha} p_{i,\alpha} \partial_{\alpha} \delta(\mathbf{r} - \mathbf{R}_i) \quad (4.4)$$

Absence of homogeneous charge means that the contribution of the $n=0$ term to the summation can be neglected and integration by parts with the equation 4.4 allows to rewrite expression 4.3 as a sum of components from the $(n-1)$ -th power of position-polarization tensor 4.5.

$$\rho(\mathbf{r}) = \sum_{n=1}^{\infty} \frac{(-1)^{n+1}}{n!} \partial_{\alpha} \partial_{\beta} \cdots \partial_{\kappa} \delta(\mathbf{r}) \sum_i (p_{i,\alpha} R_{i,\beta} \cdots R_{i,\kappa}) \quad (4.5)$$

The zero-th order of this sum over sites in terms of position has merely three components that are readily identified with sum of all polarization components p_x , p_y and p_z , leading to computation of homogeneous polarization. Higher order terms in this sum can be recasted in a more symmetrical form.

4.1.2 Rearranging into sets of terms stable versus rotations

Linear combinations of non-normalized orthogonal components of a tensor transforming in invariant subspaces under operations of $SO(3)$ are presented in the literature, including reference [3] and their general expressions were reproduced in first chapter. First order includes two ensembles containing respectively three (4.6) and five (4.8) combinations of components in addition to an $\mathbf{r} \cdot \mathbf{p}$ term.

$$\begin{aligned} & \mathbf{r}_y \mathbf{p}_z - \mathbf{r}_z \mathbf{p}_y \\ & \mathbf{r}_z \mathbf{p}_x - \mathbf{r}_x \mathbf{p}_z \\ & \mathbf{r}_x \mathbf{p}_y - \mathbf{r}_y \mathbf{p}_x \end{aligned} \quad (4.6)$$

Term by term identification to components of a vector product between position and local polarization vectors $\mathbf{r} \times \mathbf{p}$ (4.7) allows a comparison with a so-called toroidal moment.

$$\begin{pmatrix} r_x \\ r_y \\ r_z \end{pmatrix} \times \begin{pmatrix} p_x \\ p_y \\ p_z \end{pmatrix} = \begin{pmatrix} r_y p_z - r_z p_y \\ r_z p_x - r_x p_z \\ r_x p_y - r_y p_x \end{pmatrix} \quad (4.7)$$

These quantities are fully antisymmetric on index permutation between position and local polarization.

$$\begin{aligned} & r_x p_x - r_y p_y \\ & r_x p_x + r_y p_y - 2r_z p_z \\ & r_y p_z + r_z p_y \\ & r_z p_x + r_x p_z \\ & r_x p_y + r_y p_x \end{aligned} \quad (4.8)$$

The presence of five additional terms that are unaffected by index permutation just like the $\mathbf{r} \cdot \mathbf{p}$ term is associated to an $l=2$ term of an expansion of solutions of Laplace equation into spherical harmonics. Comparing the last four terms with expression of electric quadrupole $\frac{3}{2} (r_i p_j + r_j p_i) - (\mathbf{r} \cdot \mathbf{p}) \delta_{ij}$ underlines the similarities. At a second order, four sets containing respectively three (4.9), five (4.11), three (4.12), and seven (4.13) combinations are formed as follows. A fully antisymmetric under index exchange one appears again (4.9).

$$\begin{aligned} & r_z r_x p_z + r_x r_y p_y - r_y r_y p_x - r_z r_z p_x \\ & r_x r_y p_x + r_y r_z p_z - r_x r_x p_y - r_z r_z p_y \\ & r_y r_z p_y + r_x r_z p_x - r_x r_x p_z - r_y r_y p_z \end{aligned} \quad (4.9)$$

Term by term identification leads to a perfect match with a so-called hypertoroidal moment [23] defined with a double cross product of position and local polarization $\mathbf{r} \times (\mathbf{r} \times \mathbf{p})$ (4.10).

$$\begin{aligned} & \begin{pmatrix} r_x \\ r_y \\ r_z \end{pmatrix} \times \left[\begin{pmatrix} r_x \\ r_y \\ r_z \end{pmatrix} \times \begin{pmatrix} p_x \\ p_y \\ p_z \end{pmatrix} \right] = \begin{pmatrix} r_x \\ r_y \\ r_z \end{pmatrix} \times \begin{pmatrix} r_y p_z - r_z p_y \\ r_z p_x - r_x p_z \\ r_x p_y - r_y p_x \end{pmatrix} \\ & = \begin{pmatrix} r_y r_x p_y - r_y r_y p_x - r_z r_z p_x + r_z r_x p_z \\ r_z r_y p_z - r_z r_z p_y - r_x r_x p_y + r_x r_y p_x \\ r_x r_z p_x - r_x r_x p_z - r_y r_y p_z + r_y r_z p_y \end{pmatrix} \end{aligned} \quad (4.10)$$

Three other combinations of the same order having respectively five, three and seven elements appear, as stated in equations 4.11, 4.12 and 4.13.

$$\begin{aligned}
& r_y r_z p_x + r_x r_z p_y - 2r_x r_y p_z \\
& \quad r_y r_z p_x - r_x r_z p_y \\
& r_z r_x p_z - r_x r_y p_y + r_y r_y p_x - r_z r_z p_x \\
& r_x r_y p_x - r_y r_z p_z - r_x r_x p_y + r_z r_z p_y \\
& r_y r_z p_y - r_x r_z p_z - r_y r_y p_z + r_x r_x p_z
\end{aligned} \tag{4.11}$$

$$\begin{aligned}
& 2r_z r_x p_z + 2r_x r_y p_y + r_z r_z p_x + r_y r_y p_x + 3r_x r_x p_x \\
& 2r_x r_y p_x + 2r_y r_z p_z + r_x r_x p_y + r_z r_z p_y + 3r_y r_y p_y \\
& 2r_y r_z p_y + 2r_x r_z p_x + r_x r_x p_z + r_y r_y p_z + 3r_z r_z p_z
\end{aligned} \tag{4.12}$$

$$\begin{aligned}
& r_y r_z p_x + r_x r_z p_y + r_x r_y p_z \\
& 2r_z r_x p_z + 2r_x r_y p_y + r_z r_z p_x + r_y r_y p_x - 2r_x r_x p_x \\
& 2r_x r_y p_x + 2r_y r_z p_z + r_x r_x p_y + r_z r_z p_y - 2r_y r_y p_y \\
& 2r_y r_z p_y + 2r_x r_z p_x + r_y r_y p_z + r_x r_x p_z - 2r_z r_z p_z \\
& \quad 2r_z r_x p_z - 2r_x r_y p_y + r_z r_z p_x - r_y r_y p_x \\
& \quad 2r_x r_y p_x - 2r_x r_z p_z + r_x r_x p_y - r_z r_z p_y \\
& \quad 2r_y r_z p_y + 2r_x r_z p_x + r_y r_y p_z + r_x r_x p_z
\end{aligned} \tag{4.13}$$

Presence of seven terms reminds of $l=3$ term in the decomposition of solutions of Laplace equation in spherical harmonics.

4.2 Electrostatic interaction in inhomogeneous background permittivity

As mentioned in the literature review, composites composed of a ferroelectric perovskite and a nonferroelectric one have given rise to simulation of vortices. However, the experimental growth of such simulated composites that are multidimensional superlattices represents a daunting experimental challenge.

On the other hand, coating ferroelectric perovskite nanoparticles by an amorphous material having a low permittivity that is temperature-independent such as silica through a modified Stöber process has been reported [15] and assembling these coated particles seems a more experimentally tractable task. In a composite that is not made of one perovskite and another material, it would be convenient to set the polar local modes to zero inside the amorphous part and to let electronic permittivity ε_∞ evolve from its *ab initio*-derived value inside the perovskite to that of the amorphous material $\varepsilon_{amorphous}$. Even though there will be unavoidable spurious oscillation due to Gibbs phenomenon, the space-dependent simulated ε_∞ permittivity would resemble a

step function between two values representing the two materials, as shown in a one-dimensional case in figure 4.1.

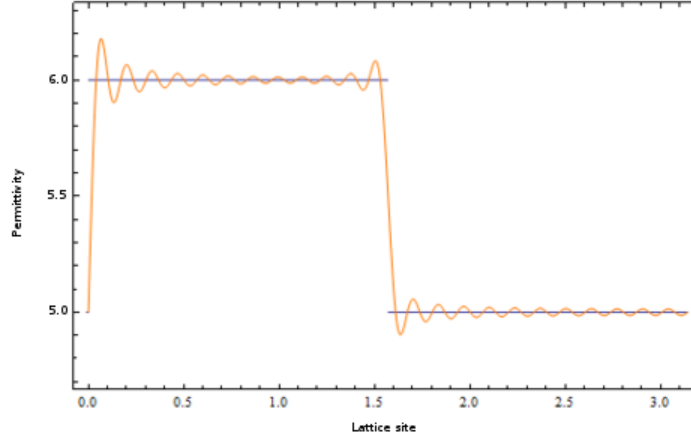


FIGURE 4.1: Permittivity spatial dependance and phenomenon of Gibbs oscillations.

If an expression was derived, it would be possible to simulate an inclusion of high linear permittivity such as liquid water inside a perovskite cube. As the experimental part has detailed it before, it seems that voids are spontaneously generated in synthesis procedures used to grow Barium Titanate nanocubes and these inclusion are possibly filled with solvent molecules.

In materials that have compositional disorder, one may try to design zones in which local modes are set to zero but there is a very large linear permittivity ε_{matrix} next to ferroelectric zones in which local modes can evolve and energetics are modelled by the entire effective Hamiltonian which has comparatively small values for the electronic contribution to permittivity ε_{∞} . As a result of interspersing zones in which local modes are set to zero, all the material is not ferroelectric but, in the rest of material, ferroelectric domains called polar nanoregions can form. As a result, dipole glass studies and possibly relaxor materials simulations can also benefit from the possibility of dealing with an inhomogeneous background permittivity.

4.2.1 Inhomogeneous permittivity without periodic boundary conditions

In the case in which background relative permittivity is not spatially constant, the main step of electrostatic interaction computation is reproduced in order to explain how results are affected: due to the spatial dependency of permittivity, the Poisson equation no longer writes as in 1.41 but rather as 4.14.

$$-\frac{\varepsilon_{\infty}(\mathbf{r} - \mathbf{R}_j)}{4\pi} \Delta V_j(\mathbf{r} - \mathbf{R}_j) = Z^* \mathbf{u}_j \cdot \nabla \delta(\mathbf{r} - \mathbf{R}_j) \quad (4.14)$$

As a consequence, the equation whose Green's function must be obtained and derivated in order to obtain the potential created by a dipole is no longer Laplace equation: its form depends on the expression of $\varepsilon_\infty(\mathbf{r})$ and equation 1.42 is no longer valid: there is no closed expression for the most general case of arbitrary $\varepsilon_\infty(\mathbf{r})$.

4.2.2 Inhomogeneous permittivity with periodic boundary conditions

If one turns to the case of periodic boundary conditions, the background permittivity can be assumed to be also periodic and to have Fourier coefficients $\hat{\varepsilon}_r(\mathbf{G})$. As in the homogeneous permittivity case, the important step remains to compute the electric field created at site i by a dipole located at site j , $-\mathbf{p}_i \cdot \mathbf{E}_j(\mathbf{R}_i)$. The Fourier transform of a Dirac comb of Gaussian dipole charge packets is left unchanged and, as the Fourier transform of product writes as a convolution product of the Fourier transforms, equation 1.44 now writes 4.15.

$$\forall \mathbf{G} \neq \mathbf{0}, \sum_{\mathbf{G}' \neq \mathbf{0}} \left(\frac{\hat{\varepsilon}_r(\mathbf{G} - \mathbf{G}')}{4\pi} (\mathbf{G} \cdot \mathbf{G}') \hat{V}_j(\mathbf{G}') \right) = Z^* (\mathbf{u}_j \cdot \mathbf{iG}) \exp \left(-\mathbf{iG} \cdot \mathbf{R}_j - \frac{|\mathbf{G}|^2}{4\lambda^2} \right) \quad (4.15)$$

This expression corresponds to a matrix product and, as such, can be inverted to yield the Fourier coefficients of potential created by a dipole located at site j : apart from the value at the origin that can be set to zero using gauge freedom, all the $\hat{V}_j(\mathbf{G})$ coefficients can be obtained. Potential discrete Fourier transform then leads to discrete Fourier transform of electric field through multiplication by reciprocal lattice vectors $\hat{\mathbf{E}}_j(\mathbf{G}) = -\mathbf{iG} \hat{V}_j(\mathbf{G})$. Electrostatic dipole-dipole interaction energy term is the opposite of scalar product of electric field at site i times dipole moment at site i . Consequently, from the Fourier coefficients of electric field, this energy is obtained through multiplication by origin shift to site i , $\exp(\mathbf{iG} \cdot \mathbf{R}_i)$ followed by inverse Discrete Fourier Transform and scalar product of the result with opposite of local mode at site i times Born effective charge $Z^* \mathbf{u}_i$. Computation of intersite interaction energy can thus be carried out even though it does no longer write as in equation 1.45.

However, to avoid a spurious self-interaction term, dipole-dipole interaction computation in periodic boundary conditions between a dipole at site i and its copies located in surrounding simulation supercells also requires to remove the field created by an isolated Gaussian dipole charge packet (1.46) at its core. Due to the fact that permittivity is periodic but the charge distribution associated to this problem is strongly aperiodic, the computation of an expression equivalent to 1.47 cannot be performed.

As a result, only the expressions of terms associated to electrostatic interaction between a dipole at site i different from site j can be obtained in periodic boundary condition.

4.3 Conclusion

Multipole expansion provide a framework describing any distribution of charges. This very general development does not need any kind of assumption on nature of sources to prove correct. However, a case of special interest is that of an ensemble of dipoles disposed on a cubic grid, that was partially dealt with in the literature about numerical simulations of BTO. Various studies on formation of vortices in materials possessing local dipoles motivated the quest for order parameters different from homogeneous polarization such as toroidal or hypertoroidal moment but these parameters seemed to be mere special components picked in a somewhat more general tensor. We have then shown how any distribution of charges emerging from an array of dipoles can in fact be reconstructed from $(n-1)$ -th power of position-polarization tensor. To the best of our knowledge, it is the first time linear combinations of components of this particular tensor were then systematically grouped into sets that are invariant under a rotation of the coordinate system. From this more general way of obtaining expressions of parameters quantifying ordering of local polarization, sets that represent the already known homogeneous polarization also called dipolar moment, toroidal and hypertoroidal moments were derived but other sets that have never been investigated before also appeared. In a vortex state in which some additional ordering occurs in spite of all components of homogeneous polarization and hypertoroidal moment remaining zero at the same time (and we will see that this situation occurred at least once, on simulating a torus that had a precise minor to major radius ratio), the order parameters described in this section or similarly constructed parameters having higher order can be calculated.

Dipole-dipole interaction in materials that do not have homogeneous permittivity can be used to model composite materials, from inclusions that have a different crystal structure and low electronic permittivity to zones that have a high linear permittivity in a compositionally disordered material. However, there is no general expression of dipole-dipole interaction in a non-periodic simulation cell that has inhomogeneous permittivity. In a periodic simulation cell with inhomogeneous permittivity, the intersite interaction term can be derived but the interaction between a dipole and its own copies cannot be obtained.

Chapter 5

Hollow nanocubes

Contents

5.1 General Barium Titanate simulations	88
5.1.1 First-principles derived original parameters	88
5.1.2 Monte-Carlo evolution	89
5.1.3 Hollow dot	90
5.2 Simulations under extreme boundary conditions	91
5.2.1 First-principles derived parameters	91
5.2.2 Case of a solid cube under short-circuit boundary condition	92
5.2.3 Case of a solid cube under open-circuit boundary condition	95
5.2.4 Case of a hollow cube under short-circuit boundary condition	98
5.2.5 Case of a hollow cube under open-circuit boundary condition	101
5.3 Simulations around a critical depolarizing field	103
5.3.1 Case of a solid cube	103
5.3.2 Case of hollow cubes	105
5.4 Conclusion	106

BYOND numerical simulations of solid shapes, experimental observations lead us into considering a case in which a particle has internal boundaries in addition to external ones. The case of Barium Titanate nanocubes received particular attention: it has been simulated that local polarization will form vortices inside each solid nanocube, but experimental confirmation was very difficult to obtain: this was assigned to the difficulty at getting the same boundary conditions as in the simulation. However, our experimental work tended to show that methods of nanocube growth often lead to hollow structures. The importance of the fact that ferroelectric nanocubes can be hollow has, to the best of our knowledge, never been estimated before. More specifically, it was expected that a cube being hollow would tremendously affect the obtained field lines pattern with a decrease in homogeneous polarization and an increase in toroidal moment on increasing the hole size as shown in figure 5.1. Extreme cases of short-circuit and open circuit boundary conditions did not let much room for observation of interplay between nanocube internal morphology and local polarization but behavior around a critical depolarization coefficient received special attention. A review of literature regarding simulation results in the case of Barium Titanate

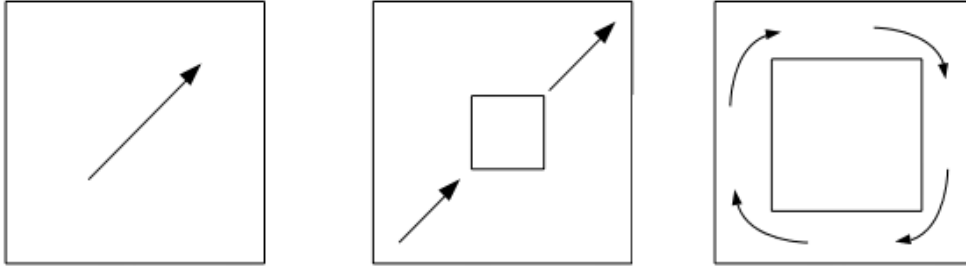


FIGURE 5.1: Expected evolution of low temperature field lines pattern.

without voids in fully periodic boundary conditions will come first. Numerical techniques used to create a hole inside the dot will also be discussed. Simulations performed without voids in this work will then be described and results will be compared with prior work. Some results obtained in a dot having a cavity under extreme boundary conditions will come afterwards and chapter will end with simulations performed around a so-called critical depolarization coefficient for an entire range of cavity sizes.

5.1 General Barium Titanate simulations

Effective Hamiltonian simulations inputs come from first principles calculations and were originally taken to be values provided afterwards. Outputs include local polarization and local strain at all sites at the end of a simulation and averaged quantities such as homogeneous polarization and strain.

5.1.1 First-principles derived original parameters

An entire set of parameters is reproduced in table 5.1.

On-site	κ_2	0.0568	α	0.320	γ	-0.473
Intersite	j_1	-0.02734	j_2	0.04020	j_5	0.00580
	j_3	0.00927	j_4	-0.00815		
	j_6	0.00370	j_7	0.00185		
Elastic	B_{11}	4.64	B_{12}	1.65	B_{44}	1.85
Coupling	B_{1xx}	-2.18	B_{1yy}	-0.20	B_{4yz}	-0.08
General	Z^*	9.956	ε_∞	5.24		

TABLE 5.1: Original first-principles derived Hamiltonian parameters [7] in atomic units.

An underestimate of lattice constant by first principles calculations due to Local Density Approximation lead to introduction of a compensating negative pressure $P = -4.8$ GPa. Practically, a tensile strain was necessary to recover experimental size of five-atom unit cells which Local Density Approximation predicted to be too small by a few percents. Simulations conducted with and

without such a tensile strain have shown that this strain notably increases the simulated transition temperatures. Simulations described in next subsection were performed in a dot containing $13 \times 13 \times 13$ sites surrounded by a vacuum layer.

5.1.2 Monte-Carlo evolution

Finite temperature cooling simulations with periodic boundary conditions lead to observation of several transitions. Increase of a strain component while remaining ones are slightly decreased is attributed to a change from a cubic to a tetragonal structure. Onset of a similar increase of a second component of strain to reach values of first component while third is decreased is linked to a tetragonal-orthorhombic transition. Another transition occurring at lower temperature towards a state where three components of strain are equal is attributed to an orthorhombic-rhombohedral change of structure, as reproduced in figure 5.2. Even though effective Hamiltonian does not

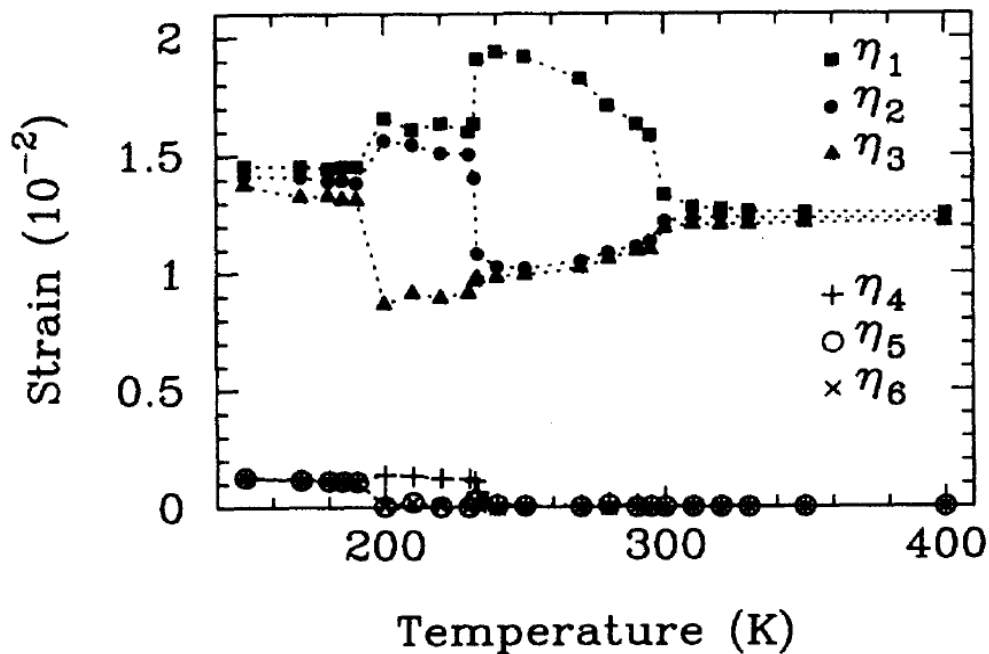


FIGURE 5.2: Temperature evolution of strain components. Figure reprinted from Zhong *et al.* [7].

exactly correspond to the formalism of Landau theory, the energy term associated to stress-strain coupling involves the square of polarization times local strain. In a description of phase transition involving a primary and a secondary order parameter, this corresponds to the case of an improper transition with a faintness index equal to two [68]. As a result, similar transition temperatures for polarization are expected. Finite values of diagonal strain at all temperatures has to be viewed as a compensation of lattice constant underestimate.

5.1.3 Hollow dot

A method was devised to simulate a ferroelectric hollow cube. Five-atom unit cells were supposed to be spaced evenly inside a simulation box as in the original case. Yet, during the generation of the simulation cell, a list of all sites located in a layer on the simulation cell surface and inside a tunable cubic volume was built. In the code that was subsequently used, a Monte-Carlo step consisted of three separate updates of local parameters. An attempt at displacing the corner of a site was performed to update local inhomogeneous strain (due to periodic boundary conditions the position of a site located at one surface is equal to that of the site located on the opposite surface, so the whole cell cannot shrink or expand) and an attempt at changing polar local mode was also considered. After a loop running over all sites, an attempt at changing the value of an independent variable representing homogeneous strain is performed. Replacing a five-atom site by a vacuum site was done as follows. Homogeneous strain update part of the code was left unchanged but local mode and local inhomogeneous strain was prevented from evolving. As the code started with an absence of local polarization and inhomogeneous strain, this technique simulated vacuum with a material that had the same elastic constant as Barium Titanate but an absence of polar distortion and inhomogeneous strain. With this methodology, any ensemble of sites could be replaced by vacuum but, in this chapter, we chose to focus on a cubic hollow inclusion centered in the simulation supercell as represented in figure 5.3. The only parameter

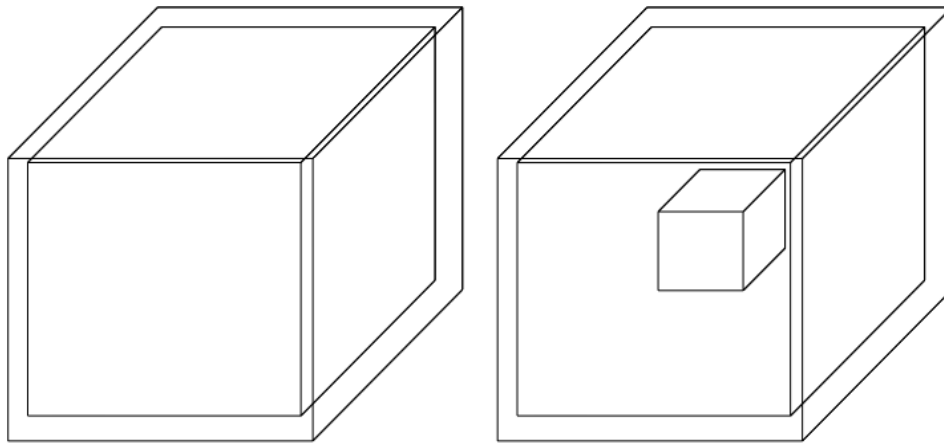


FIGURE 5.3: Simulation cell representing a cube of ferroelectric material surrounded by one vacuum layer (left) and simulation cell representing the same cube with a vacuum inclusion inside it (right).

that was tuned was lateral size of cubic hollow inclusion that ranged from total absence of any vacuum sites to all sites being vacuum apart from the surfaces.

5.2 Simulations under extreme boundary conditions

Results obtained in the case of a cube having perfect Short Circuit or completely Open Circuit electrical boundary conditions will now be presented.

5.2.1 First-principles derived parameters

Simulations performed and described later were conducted with a different set of input parameters reproduced in table 5.2. Apart from the κ_2 and j coefficients, these parameters were more recently derived in [69] to simulate a solid called Barium Strontium Titanate containing an arbitrary fraction of Barium and Strontium on the A site of the perovskite and used in the case where all the simulated sites contain Barium. This set of parameters was consistent with that employed during

On-site	κ_2	0.051758	α	0.2808	γ	-0.41281
Intersite	j_1	-0.0120107708	j_2	0.0222156256	j_5	0.003536007
	j_3	0.0042062141	j_4	-0.0023677794		
	j_6	0.0007541296	j_7	0.000377065		
Elastic	B_{11}	4.776	B_{12}	1.610	B_{44}	1.725
Coupling	B_{1xx}	-1.973	B_{1yy}	-0.041	B_{4yz}	-0.059
General	Z^*	9.6646	ε_∞	5.21		

TABLE 5.2: Numerical values used to simulate Barium Titanate.

the prior thesis of Mickaël Anoufa [15]. Simulations described in the entire rest of this chapter were performed in a dot containing $15 \times 15 \times 15$ sites including one surrounding layer representing vacuum under a negative pressure of -5.2 GPa that aimed at correcting the underestimate of lattice constant due to Local Density Approximation. The completely shorted ($\beta=1$) case can be compared with periodic simulations without pseudo-perovskite of the prior thesis, but presence of this vacuum layer on the surfaces did modify the sequence of phase transitions. Comparison with another set of results obtained in the course of the thesis of Lydie Louis [14] through simulation conducted with parameters extracted by Iniguez *et al.* [70] is possible, though effective Hamiltonian coefficients and applied negative pressure -4.8 GPa are markedly different since they come from results of Iniguez *et al.*. To a lesser extent, the fact that results were not obtained during cooling as in this work but during a posterior annealing process can lead to overestimating the temperature of transitions. The choice of cooling simulation in this work, on the other hand, tends to underestimate transition temperatures but allowed significantly lower simulation times and direct comparison with prior simulations of Mickaël Anoufa that were also performed on cooling. However, even if we emphasized the differences between the two types of simulations, both were conducted in periodic boundary conditions (results for the effective Hamiltonian of Barium Strontium Titanate were, for instance, reported in [71]) and lead to the experimentally reported sequence of phase transitions occurring in bulk.

5.2.2 Case of a solid cube under short-circuit boundary condition

Evolution as a function of temperature under perfect screening conditions $\beta = 1$ shares some similarities with a completely periodic case and particularly the same dipole-dipole interaction expression. However, the presence of a layer of sites that have no inhomogeneous strain and polarization on the surface can drastically modify obtained results as it was reported in the thesis of Lydie Louis [14] or with the effective Hamiltonian of Barium Strontium Titanate [71]; moreover, the experimental verification of simulation results would require to follow the temperature evolution of an isolated ferroelectric nanocube surrounded by a layer of metal and this has, to the best of our knowledge not been reported yet. In the simulations conducted with the set of coefficients we mentioned, low temperature state is also rhombohedral with three finite components of homogeneous strain and has an energy of -1.537×10^{-3} Ha (-41.82 meV). The same presence of uniform local distortion can be noticed on a figure representing the local polarization on the surface layer of the cube at the lowest simulated temperature in the left of figure 5.4. The overall polarization pattern at low temperature consists of unique preferred spontaneous polarization direction along a [111] axis, that is represented on the simplified right side of figure 5.4. At high

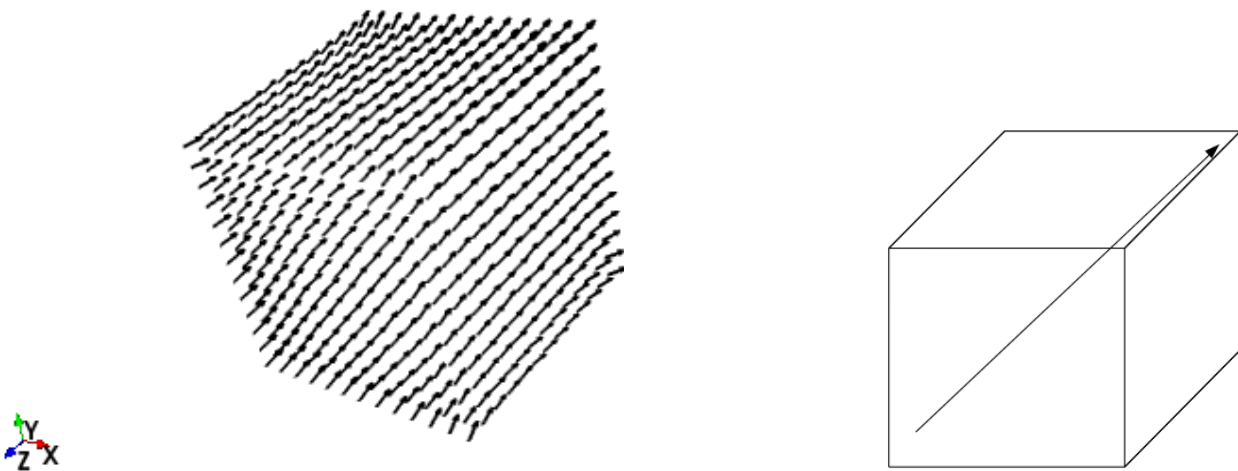


FIGURE 5.4: Local polarization pattern on the surface of a solid dot (left) and general structure of polarization (right) under a depolarization coefficient $\beta = 1$ at a temperature $T = 5$ K.

temperatures, little deviation from a cubic structure is observed apart from thermal expansion. Adding a vacuum layer on the surfaces with regard to the completely periodic case removes the sequence of three phase transitions occurring at distinct temperatures, exactly as it has been reported with effective Hamiltonian simulations of Barium Strontium Titanate [71]. Onset of finite values of each component of strain occurs mostly at the same time, as can be seen in figure 5.5 left and right sides. From these figures and from the temperature evolution of other order parameters

such as homogeneous polarization, critical temperature can be assumed to be $T_c = 400$ K. All diagonal components simultaneously evolve from a positive 1.05 percents representing the tensile strain compensating lattice side underestimate at the transition temperature to 1.15 percents at low temperature whereas all off-diagonal components go from negligible values at high temperatures to 0.06 percents. Polarization exhibits a similar behavior including a direct change from a

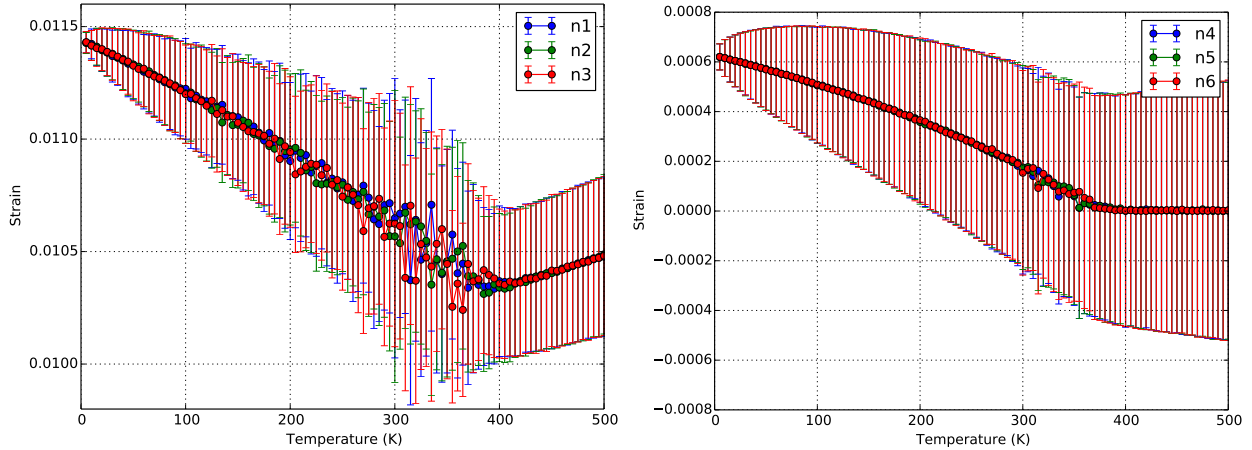


FIGURE 5.5: Temperature evolution of absolute values of diagonal (left) and off-diagonal (right) components of strain in a solid dot under a depolarization coefficient $\beta = 1$.

high temperature nonpolar structure to a low-temperature phase having polarization along a $[111]$ direction through a transition at $T_c = 400$ K of all three components visible in figure 5.6. Typical values of polarization at low temperature in atomic units are of the order of 0.004 a.u. for $\beta = 1$ boundary conditions. The results obtained in [14] are reproduced in figure 5.7 for comparison.

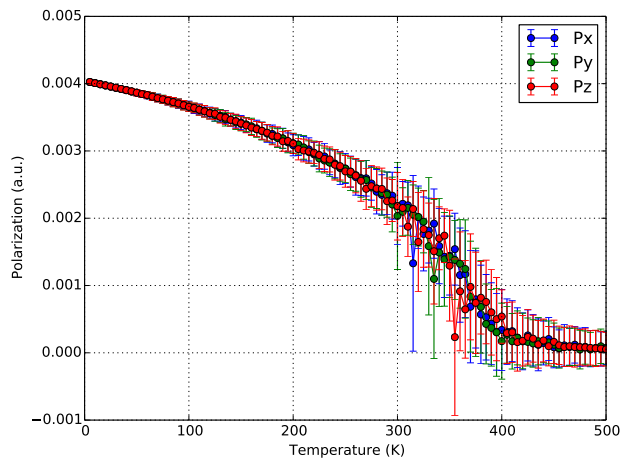


FIGURE 5.6: Temperature evolution of absolute values of all components of polarization in a solid dot under a depolarization coefficient $\beta = 1$.

The highest transition temperature is also predicted to be at 400 K. Low temperature state similarly features three finite components of polarization having values of the order of 4.0×10^{-3} a.u.

but the behavior in the intermediate temperature range is different: the onset of the three components of polarization happens at different temperatures. However, also in that case, the presence of a vacuum layer modifies the sequence of phase transitions that could be expected from a simulation of bulk Barium Titanate. The sequence no longer features a cubic-tetragonal-orthorhombic-rhombohedral sequence, but rather a cubic-tetragonal-monoclinic-rhombohedral one. The common feature is that both simulations predict a sequence of phase transitions that is not that of the bulk for an isolated cube in short-circuit boundary conditions and the difference between results could be explained by the different set of coefficients and negative pressure employed or the fact that simulation outputs are recorded on annealing in that work. Values of toroidal moment do

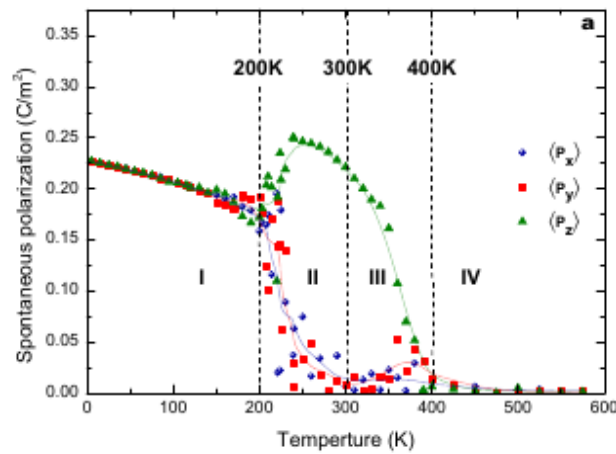


FIGURE 5.7: Prior simulations of all components of polarization in a solid dot under a depolarization coefficient $\beta = 1$ obtained in [14].

not exhibit a very significant surge with respect to error bars in most of the temperature evolution represented in figure 5.8. Overall evolution tends to display a transition from a high temperature

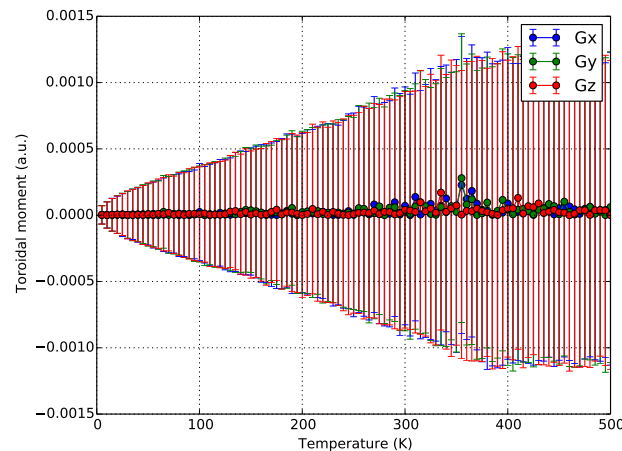


FIGURE 5.8: Temperature evolution of absolute values of all components of toroidization in a solid dot under a depolarization coefficient $\beta = 1$.

nonpolar state to a homogeneously polarized one, without very significant toroidization.

5.2.3 Case of a solid cube under open-circuit boundary condition

Temperature evolution on cooling under perfect open circuit conditions $\beta = 0$ differs even more from a completely periodic case. A low temperature state still exhibits finite components of homogeneous strain and has an energy of -1.093×10^{-3} Ha. At high temperatures, only thermal expansion is observed again. A transition occurs on all components at the same time again, but at much lower temperatures. The detailed vortex structure formed by local distortion can be viewed on a figure representing the local polarization on the surface layer of the cube at the lowest simulated temperature in the left part of figure 5.9. The overall polarization pattern at low temperature consists of a polarization vortex that lies along a [111] axis, that is represented in the right side of figure 5.9. No vortex is observed in the cubic state and onset of this vortex requires a symmetry breaking, namely a transition to rhombohedral state. All components of diagonal strain exhibit

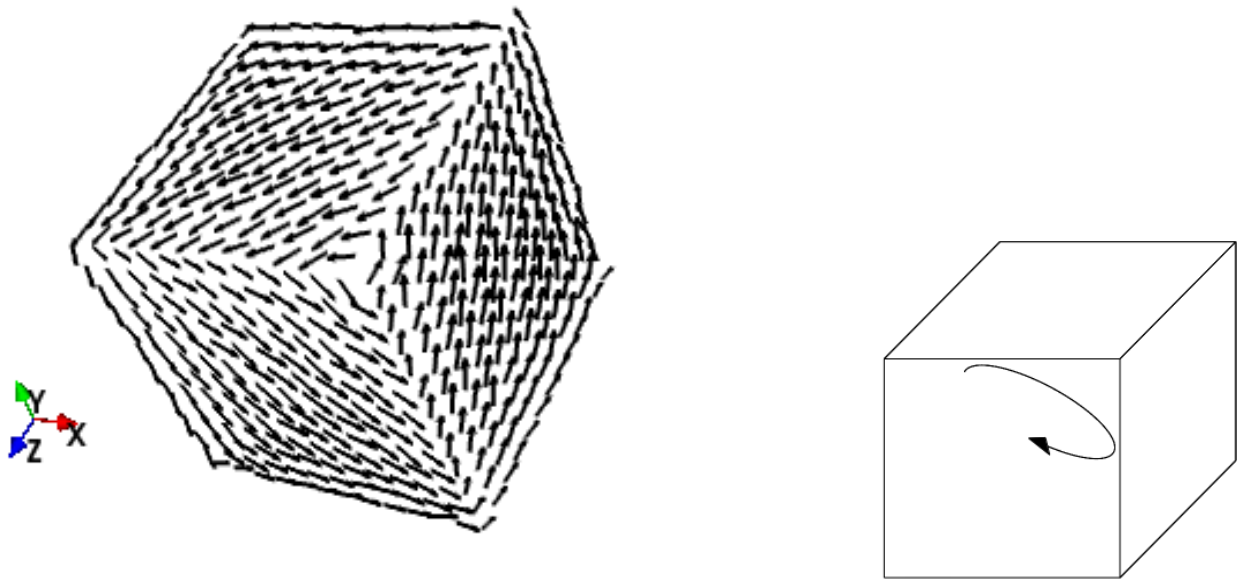


FIGURE 5.9: Local polarization pattern on the surface of a solid dot (left) and overall view (right) under a depolarization coefficient $\beta = 0$ at a temperature $T = 5$ K.

an steadily increasing behavior at high temperatures due to thermal expansion. A change at low temperature in evolution of diagonal strain also affects all three components at once: this transition on all components of strain can be seen in left part of figure 5.10. Transition in strain and evolution of other order parameters such as toroidal moment lead to assuming that critical temperature is lowered to $T_c = 100$ K in this case. Diagonal components all simultaneously evolve from 0.97 percents at the transition temperature to 1.02 percents at the lowest simulated temperature. A compensation of lattice underestimate is again present, but the effect of this transition on

strain are quantitatively weaker than under short-circuit boundary condition. The right part of figure 5.10 shows that off-diagonal components of strain exhibit the same transition temperature $T_c = 100$ K and rise from negligible values at high temperatures to 0.01 percents, even though error bars are relatively large on this quantity. Polarization no longer exhibits nonzero values on

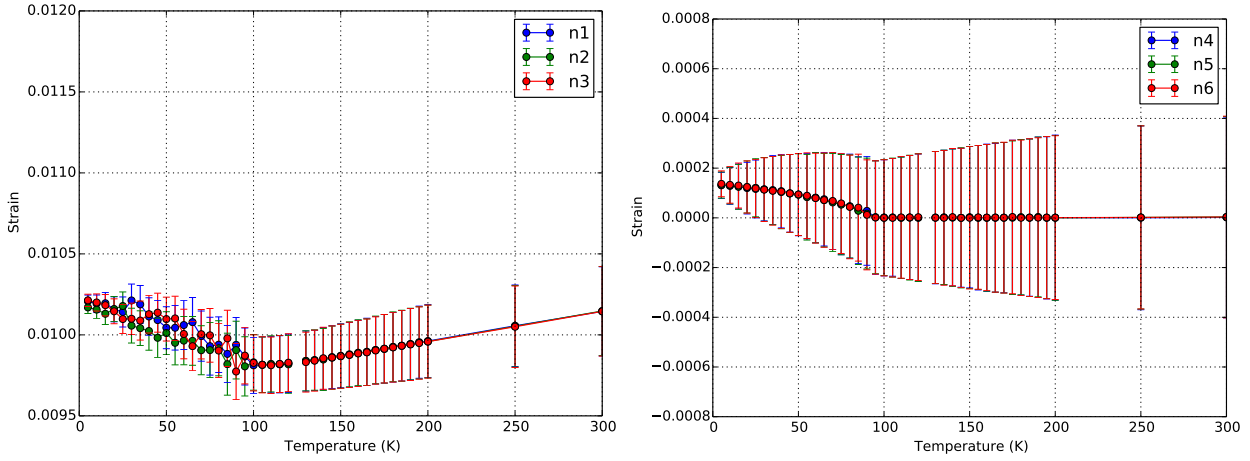


FIGURE 5.10: Temperature evolution of absolute values of diagonal (left) and off-diagonal (right) components of strain in a solid dot under a depolarization coefficient $\beta = 0$.

any component at all temperatures and fluctuations within error bars are visible in figure 5.11. In more detail, only the x-axis component seems to become finite at an extremely low $T_c = 30$ K but it then reaches values of approximately 1.5×10^{-5} a.u. that can be compared with 0.004 a.u. in the $\beta = 1$ case. Homogeneous polarization does not seem to describe the polar order in the low temperature phase. Evolution of toroidization, on the other hand, resembles that of strain:

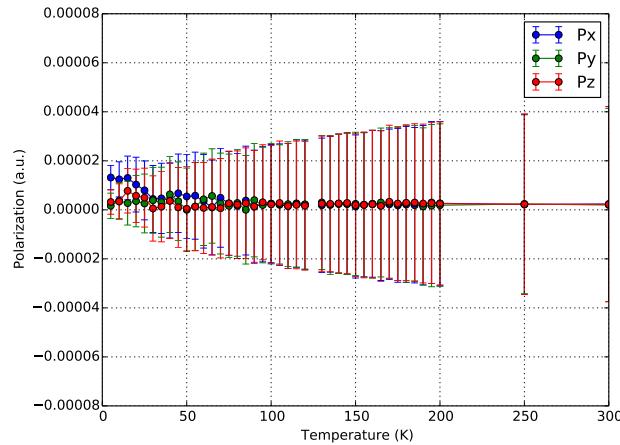


FIGURE 5.11: Temperature evolution of absolute values of all components of polarization in a solid dot under a depolarization coefficient $\beta = 0$.

values of all components of toroidal moment at high temperature are negligible and remain so only until a transition occurs at $T_c = 100$ K. All three components of toroidization are finite at low

temperature and the transition temperature for all components is the same as can be seen in figure 5.12. Toroidal moment at low temperature in atomic units is about 0.022 a.u. for $\beta = 0$ boundary conditions. Results obtained in [14] are reproduced in figure 5.13 for comparison. As these were

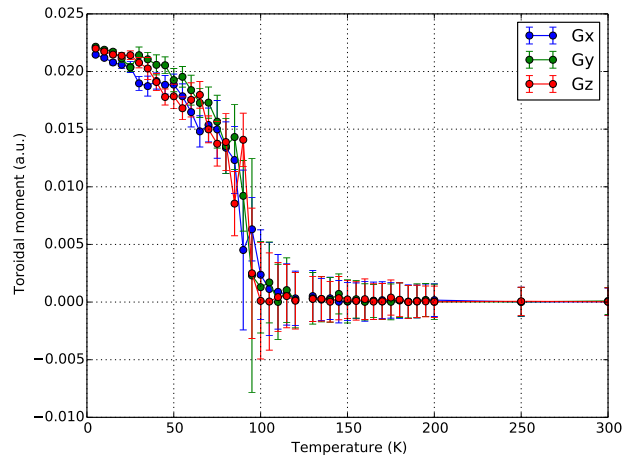


FIGURE 5.12: Temperature evolution of absolute values of all components of toroidization in a solid dot under a depolarization coefficient $\beta = 0$.

obtained through an annealing sequence, the initial low temperature state had an influence on the entire phase transition sequence and various techniques including simple cooling or a more complex sequence of cooling-poling-relaxing were proposed. Using the ground state obtained with this second technique, the low temperature state similarly features three finite components of toroidization that all arise at the same temperature. Yet, the transition temperature is predicted to be at 200 K in that work, contrary to 100 K in the simulation performed above. As the set of simulation parameters and negative pressure are different, this discrepancy remains possible.

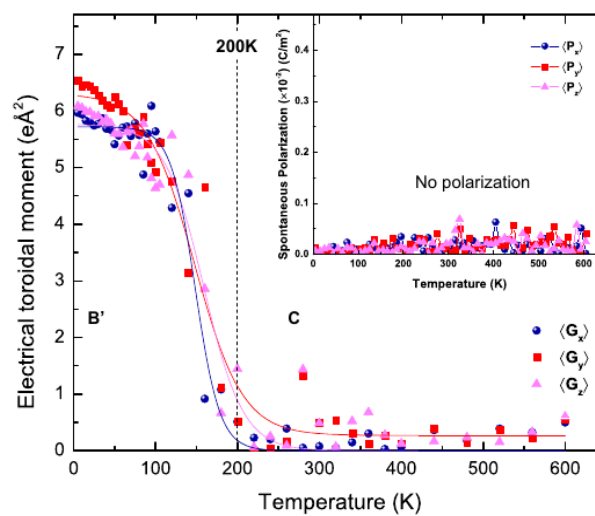


FIGURE 5.13: Prior simulations of all components of toroidization in a solid dot under a depolarization coefficient $\beta = 0$ obtained in [14].

Onset of a toroidization along [111] for completely open-circuit $\beta = 0$ boundary conditions completely replaces polarization along [111] in a short-circuit $\beta = 1$ case.

5.2.4 Case of a hollow cube under short-circuit boundary condition

Simulation results under both extreme boundary conditions $\beta = 0$ and $\beta = 1$ were not found to depend at all on hole size and typical results are reproduced for a dot having a $5 \times 5 \times 5$ hole at its center. In the specific case of $\beta = 1$, low temperature state is again rhombohedral with three finite components of homogeneous strain and has an energy of -1.462×10^{-3} Ha. A vector plot representing the local polarization on the surface layer of the hollow cube at the lowest simulated temperature is shown in the left part of figure 5.14 and exhibits the same homogeneous polarization features that were observed in the solid cube case. Despite presence of an inner vacuum zone in which local polarization is set to zero, there are no effects on the overall polarization pattern at low temperature. It still consists of unique preferred spontaneous polarization direction along a [111] axis, that is represented in the right part of figure 5.14. Presence of a hole does not modify

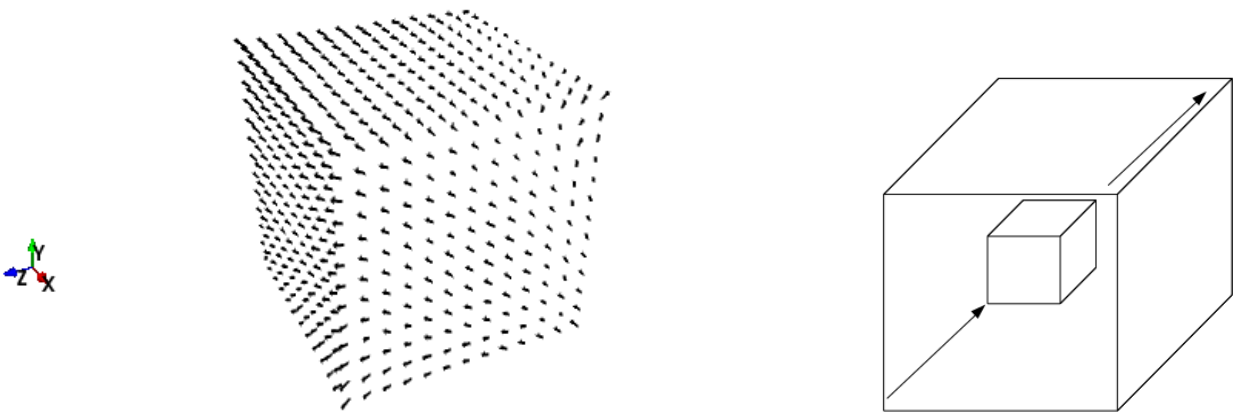


FIGURE 5.14: Local polarization pattern on the surface (left) and its general structure (right) for a dot including a $5 \times 5 \times 5$ hole under a depolarization coefficient $\beta = 1$ at a temperature $T = 5$ K.

the loss of the sequence of three phase transitions occurring at distinct temperatures. The high temperature evolution of diagonal strain still has a baseline corresponding to negative pressure superimposed with thermal expansion in all directions. Onset of finite values of each component of strain occurs mostly at the same time and transition temperatures are not significantly different from the case that had no void, as can be seen in left and right side of figure 5.15. In more detail, the transition seems to occur at $T_c = 400$ K for two components of diagonal strain and at 350 K for the other one. Positive values of 1.02 percents are observed at the transition temperature for diagonal strain, whereas the low temperature values are as high as 1.11 percents. The transition on all components of off-diagonal strain occurs at $T_c = 400$ K and results on turning from a state

with vanishing values of off-diagonal strain to a low temperature one with 0.06 percents. The cube

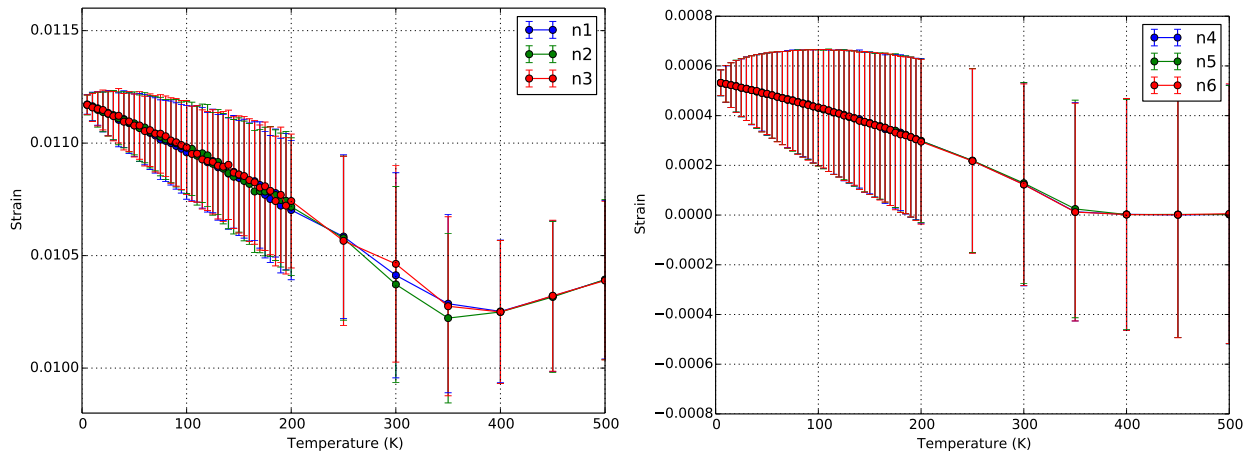


FIGURE 5.15: Temperature evolution of absolute values of diagonal components of strain in a dot with a $5 \times 5 \times 5$ hole under a depolarization coefficient $\beta = 1$.

being hollow does not change polarization behavior including a direct change from a high temperature nonpolar structure to a low-temperature phase having polarization along a $[111]$ direction as in figure 5.16. Transition on all three components occurs at $T_c = 400$ K for all three components. In atomic units, typical values of polarization are again of the order of 0.004 a.u. at low temperature for $\beta = 1$ boundary conditions. A value smaller than that obtained for a solid dot was expected due to absence of polarization in the hollow inclusion but higher values of local polarization all around this zone compensated this effect. Presence of a hole does not change negligibility of val-

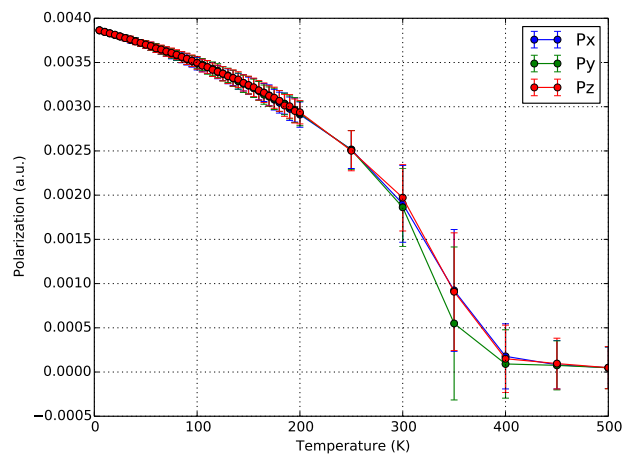


FIGURE 5.16: Temperature evolution of absolute values of all components of polarization in a dot with a $5 \times 5 \times 5$ hole under a depolarization coefficient $\beta = 1$.

ues of toroidal moment with respect to error bars in most of a temperature evolution represented in figure 5.17. The hollow inclusion favoured a state that only had polarization.

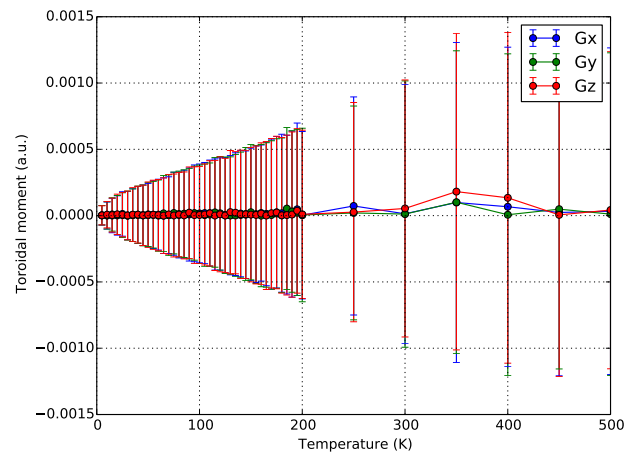


FIGURE 5.17: Temperature evolution of absolute values of all components of toroidization in a dot with a $5 \times 5 \times 5$ hole under a depolarization coefficient $\beta = 1$.

On the whole, the trend going from a high temperature nonpolar state to a homogeneously polarized one without toroidization is globally preserved.

5.2.5 Case of a hollow cube under open-circuit boundary condition

Temperature evolution on cooling under perfect open circuit conditions $\beta = 0$ is also close to the solid cube equivalent case. Finite components of homogeneous strain are again observed in the low temperature state that has an energy of -1.084×10^{-3} Ha whereas the high temperature zone only gives rise to thermal expansion again. A simultaneous transition affecting all components of toroidal moment is observed at low temperatures. Presence of a zone without local polarization at the center of simulated supercell did not affect the vortex structure formed by local distortion around it. It is shown on a figure representing the local polarization on the surface layer of the cube at the lowest simulated temperature in the left part of figure 5.18. Right side of figure 5.18 displays the overall low temperature polarization pattern with a polarization vortex surrounding the zone representing vacuum. All diagonal components of strain increase steadily at high

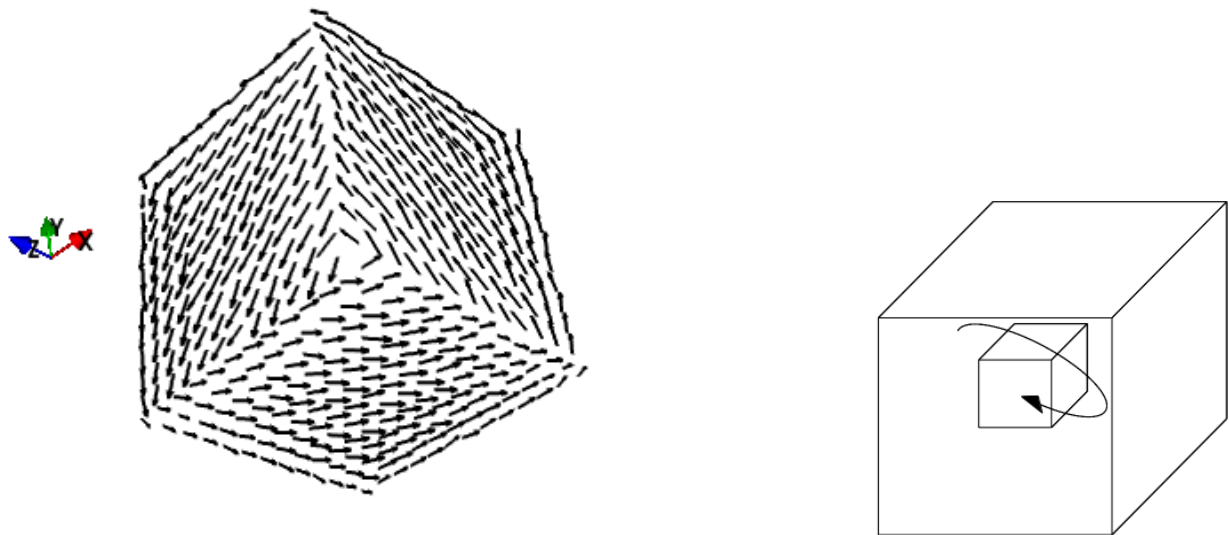


FIGURE 5.18: Local polarization pattern on the surface of a hollow dot (left) and global view (right) under a depolarization coefficient $\beta = 0$ at a temperature $T = 5$ K.

temperatures due to thermal expansion. As in the solid cube case, the behavior of all three components of diagonal strain simultaneously changes at low temperatures: these three transitions can be observed on the left part of figure 5.19. Evolution of diagonal strain and toroidal moment shows that the transition temperature is completely left unchanged by presence of a hole inside the dot: it remains the same $T_c = 100$ K as in the solid cube case. In more detail, the diagonal components evolve from 0.97 percents at the transition temperature to 1.01 percents at the lowest simulated temperature: on the whole, the behavior of diagonal strain is left unchanged compared to the solid cube case. The evolution of off-diagonal components of strain can be seen in the right

part of figure 5.19. Error bars are large again but as in the solid cube case, the transition that occurs on all off-diagonal strain components takes place at the same $T_c = 100$ K that other components of strain: it goes from negligible values at high temperatures to 0.01 percents at the lowest simulated temperature. Destruction of all components of homogeneous polarization is also visible at

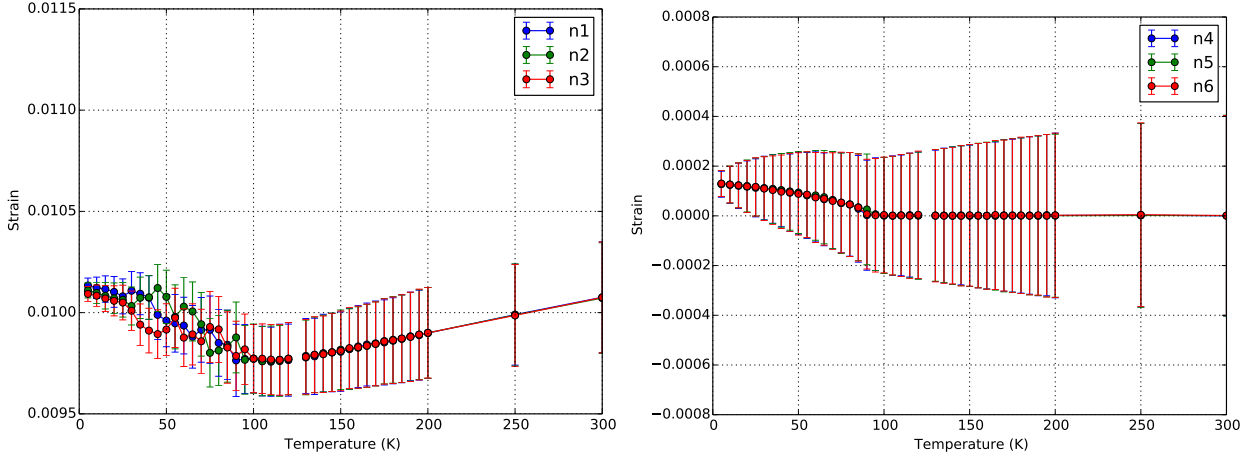


FIGURE 5.19: Temperature evolution of absolute values of diagonal (left) and off-diagonal (right) components of strain in a dot with a $5 \times 5 \times 5$ hole under a depolarization coefficient $\beta = 0$.

all temperatures. Fluctuations within error bars are plotted in figure 5.20. In more detail, all three components of polarization seem to become finite at an extremely low $T_c = 35$ K but they then reach values of the order of 2×10^{-5} a.u. that can be compared with 0.004 a.u. in the $\beta = 1$ case. Presence of a hole did modify slightly the low temperature behavior because in the solid cube case, only one component became finite at $T_c = 30$ K but this transition remains very small and ordering of polarization in the low temperature phase can be inferred to be mostly inhomogeneous. Values

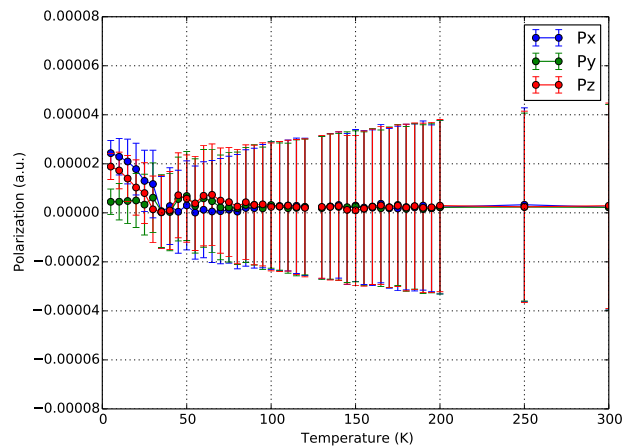


FIGURE 5.20: Temperature evolution of absolute values of all components of polarization in a dot with a $5 \times 5 \times 5$ hole under a depolarization coefficient $\beta = 0$.

of all components of toroidal moment as a function of temperature have an evolution analogous

to that of diagonal or off-diagonal strain. Just like in the solid cube case, all three components of toroidal moment vanish at high temperatures and all three become finite at $T_c = 100$ K. Figure 5.21 shows that low temperature values of all three components of toroidization are the same. Presence of a hole did not modify at all the 0.022 a.u. result obtained in the case of a solid dot. Extreme cases of toroidization along [111] for completely open-circuit boundary conditions and

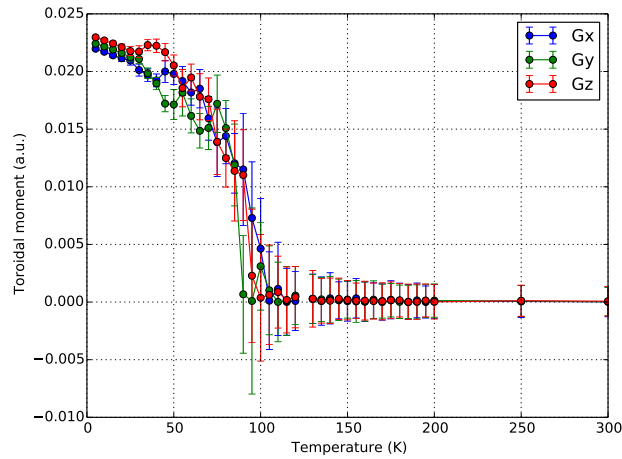


FIGURE 5.21: Temperature evolution of absolute values of all components of toroidization in a dot with a $5 \times 5 \times 5$ hole under a depolarization coefficient $\beta = 0$.

polarization along [111] in short-circuit conditions are left unchanged by presence of a void. Only minor differences on off-diagonal strain or a very low temperature small transition on homogeneous polarization were found to differ between the solid and hollow dot. Yet, a behavior in an intermediate range of boundary conditions happens to be more sensitive to presence of hollow inclusions.

5.3 Simulations around a critical depolarizing field

Particular sensibility was found to exist in cases for which electrostatic boundary conditions are in an intermediate range. Evolution for various values of β will now be described.

5.3.1 Case of a solid cube

Absolute values of all components of polarization and toroidal moment at low temperature $T = 5$ K were found to evolve rapidly around relevant values of β that were displayed in figure 5.22. Little coexistence was observed, only values $\beta = 0.87$ and $\beta = 0.88$ allowed observation of coexistence of polarization with toroidal moment. Homogeneous polarization with three finite components resembling a $\beta = 1$ case was present above a critical value and homogeneous toroidization was very small. Below a critical depolarization coefficient of approximately $\beta \approx 0.875$ three components of homogeneous toroidization became finite and homogeneous polarization was strongly diminished as in a $\beta = 0$ case. These results can be compared with those obtained in [14] that are

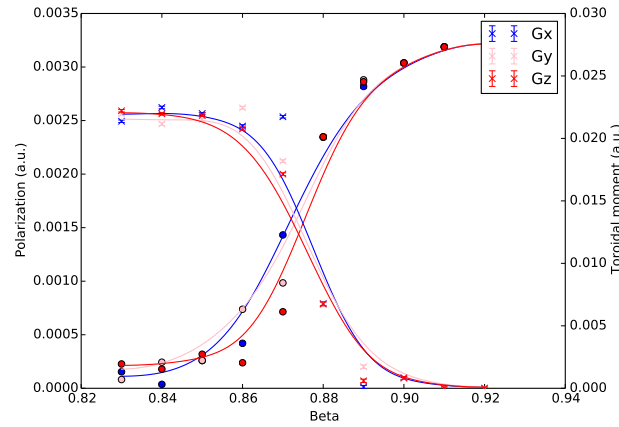


FIGURE 5.22: Low temperature homogeneous polarization and toroidal moment components for a solid cube for different values of depolarization coefficient β .

reproduced in figure 5.23. The use of different coefficients to simulate Barium Titanate results in some noticeable differences: the coexistence region is larger and it is centered on higher values of depolarization coefficient. The surprising result is that the behavior simulated for Barium Titanate in this work is closer to results reported for lead zirconate titanate simulations in [14]. Evaluating

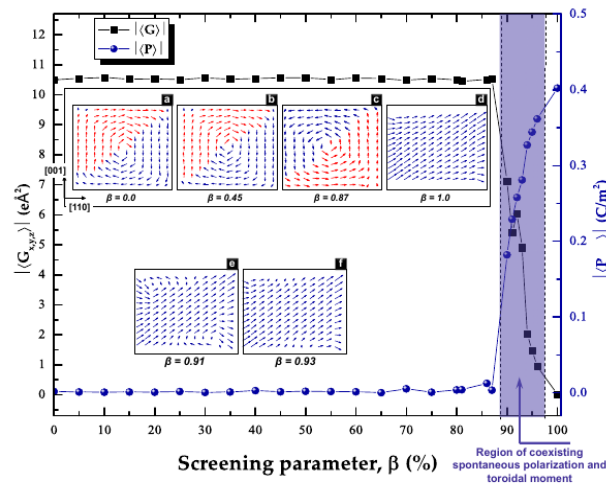


FIGURE 5.23: Previously simulated [14] low temperature homogeneous polarization and toroidal moment components for a solid cube at different β .

an experimental value of parameter β is particularly challenging but prior work including [72] and [28] tended to agree on a value $\beta = 0.97$. Particular attention thus has to be paid to the evolution of the system under this screening coefficient. In the simulations performed during this work, as it is above $\beta \approx 0.875$, homogeneous polarization is expected.

5.3.2 Case of hollow cubes

Most representative hollow inclusion size are studied through similar plotting of order parameters at $T = 5$ K. Figures 5.24, 5.25 and 5.26 represent three distinct cases of polarization and toroidal moment evolution. For a $3 \times 3 \times 3$ hollow inclusion, a strong analogy to the solid cube

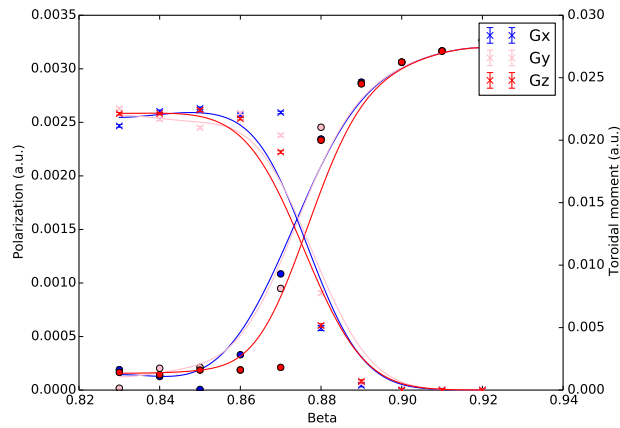


FIGURE 5.24: Low temperature homogeneous polarization and toroidal moment components for a cube with a $3 \times 3 \times 3$ hole for different values of depolarization coefficient β .

case is observed. All three components of homogeneous polarization remain finite above a critical value of depolarization coefficient with small homogeneous toroidization. Below a value of $\beta \approx 0.875$ resembling exactly the solid nanocube case, homogeneous polarization decreases and toroidization arises. The coexistence region is not wider than for the solid cube case and only values $\beta = 0.87$ and $\beta = 0.88$ again allowed observation of polarization superimposed with toroidal moment. Increasing hole size to a $7 \times 7 \times 7$ volume leads to a small deviation from previous case.

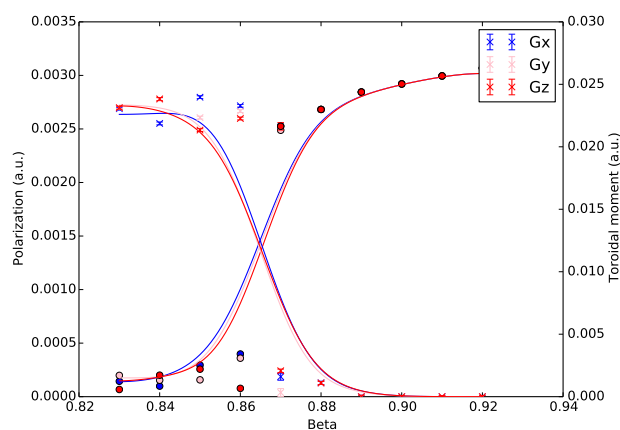


FIGURE 5.25: Low temperature homogeneous polarization and toroidal moment components for a cube with a $7 \times 7 \times 7$ hole for different values of depolarization coefficient β .

A homogeneously polarized state with little toroidization is still observed above a threshold β .

Homogeneous polarization vanishes and toroidization sets on at a value of $\beta \approx 0.865$ that seems lower than in solid or barely hollow cases. The coexistence region is again extremely thin and polarization with toroidal moment is only observed for $\beta = 0.86$ and $\beta = 0.87$. A similar trend

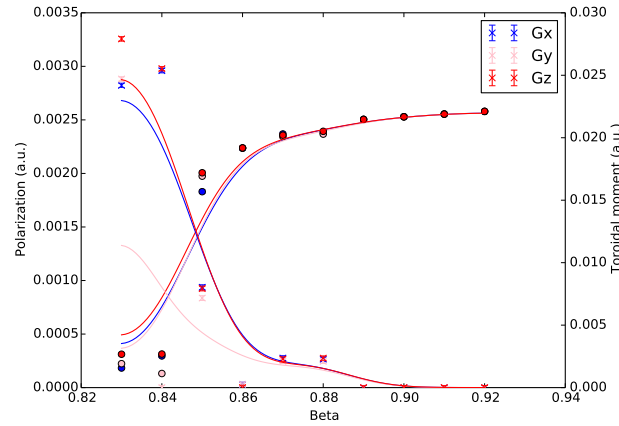


FIGURE 5.26: Low temperature homogeneous polarization and toroidal moment components for a cube with a $11 \times 11 \times 11$ hole for different values of depolarization coefficient β .

is maintained on increasing hole size to $11 \times 11 \times 11$. Homogeneous polarization remains stable and no toroidization appears in most of simulated range. A decrease of polarization and a rise in toroidization leads to a critical $\beta \approx 0.845$, with coexistence of polarization and toroidal moment at $\beta = 0.84$ and $\beta = 0.85$. Through a decrease of critical value of critical screening coefficient, adding a volume of vacuum inside a ferroelectric cube alters low temperature equilibrium structure. Yet, as experimental values of screening coefficients were reported to be $\beta = 0.97$, a homogeneous polarization state is expected.

5.4 Conclusion

Pure Barium Titanate is the product of experimental syntheses and a textbook example of ferroelectricity. Results previously obtained on this material with perfectly periodic boundary conditions were recalled first: by modifying the atomic positions, coefficients describing a perturbative expansion of energy around a cubic structure were derived. This effective Hamiltonian approach gives an expression of energy as a function of atomistic degrees of freedom that can be used in Metropolis simulation. The more this expansion describes accurately the change in energy associated to relative displacements of ions, the more precisely the phase transitions occurring in the material are predicted. On describing the bulk properties of the material, a sequence of phase transitions on cooling from cubic to tetragonal followed by tetragonal to orthorhombic and orthorhombic to rhombohedral is predicted in agreement with experiments. However, these simulations in bulk completely use the periodic boundary conditions and, as such, neglect any effect related to the presence of surfaces. As in the literature, it is possible to keep the same effective

Hamiltonian but to change boundary conditions. Regarding electrostatic interaction, a linear combination between Open-Circuit and Short-Circuit boundary conditions is performed. For short-ranged interactions, at the simulated material surfaces, a layer in which inhomogeneous strain and local polarization are zero is added in order to remove any effect from periodic boundary conditions at the sites located on the surfaces of the simulation cell. This last procedure was assumed to provide a way of replacing some sites by a medium as close as possible to vacuum. As experimentally produced cubes were hollow, this work then focused on simulating these shapes. As a consequence, in addition to setting inhomogeneous strain and polarization to zero on the surface, the same steps were applied for all sites located in an inside cube. In other words, the whole simulation cell represented $15 \times 15 \times 15$ sites, the surface layer represented vacuum and the same model was applied to a cubic inclusion of variable size located at the center.

The general expectation was that increasing hole size would lead to vanishing homogeneous polarization and increased toroidal moment. Simulations performed under open-circuit or short-circuit boundary conditions were described afterwards but hollow and solid cubes did not give rise to very different results: short-circuit boundary conditions lead to homogeneous polarization with virtually no toroidization and open-circuit boundary conditions gave homogeneous toroidization with no homogeneous polarization. These results were mostly independent from presence or absence of a hollow region at the center of simulated ferroelectric dot. Yet, intermediate boundary conditions lead to a transition from one behavior to another at a so-called critical depolarization coefficient. The evolution of this coefficient on changing the size of hollow inclusions was studied. It was shown that as the size of the inclusion becomes larger, the critical depolarization coefficient decreases: the narrow zone in which there is a coexistence of homogeneous polarization and toroidal moment is present at smaller values of the depolarization coefficient. Overall, the homogeneously polarized state stability is increased by the presence of a cavity. This counterintuitive result contradicts the original behavior that was expected for increasing hole sizes. It can be explained by the fact that in the homogeneous polarization state, the hole removes dipoles that had little impact on the overall pattern, whereas in the case of toroidal polarization, the hole removes a fraction of the vortex core which tends to destabilize the structure. The fact that the existence of a hole tends to favour a homogeneously polarized state is, however, fully in agreement with the absence of experimental observation of vortices in ferroelectric dots.

Chapter 6

Nanotori

Contents

6.1 Considered shapes	109
6.1.1 Torus construction	110
6.1.2 Electrical boundary conditions	111
6.1.3 Local polarization representation	111
6.2 Geometry-dependent transitions	111
6.2.1 Torus having small minor to major radius ratio	112
6.2.2 Torus having close minor and major radius	114
6.2.3 Intermediate major to minor torus radius ratio	116
6.3 Beyond toroidal moment	118
6.3.1 Another charge moment	118
6.3.2 Geometry-dependent temperature behavior	120
6.3.3 Electric field cycling	122
6.4 Conclusion	124

ADDITIONAL experimental results lead into studying shapes that were no longer following simulation supercell surfaces. Local polarization tended to produce exotic patterns that were relatively poorly described by homogeneous polarization and toroidal moment. An introduction to simulation conditions will be provided first. Several polarization patterns will be discussed afterwards. A relevant order parameter will then be introduced and a discussion on effect of a homogeneous electric field will follow. A driving force for the search of new order parameter can be the fact that ferroelectric toroidization is an axial vector. As such, it cannot be affected by homogeneous electric fields and writing memory nanodevices storing information on toroidal moments requires complex solutions. These reasons motivated the study of nanorings with an off-centered hole

6.1 Considered shapes

Beyond hollow cubes, there has already been an enormous research effort in experimental synthesis and effective Hamiltonian simulation of superlattices of BTO wires [72, 73] or planes [74].

Dealing with PZT, simulations of flat nanoparticles were conducted [75, 76] and lead to local polarization topological defects [77] of an interesting nature. However, even though experimental production of arrays of PZT tori was reported [78], less attention has been paid to effective Hamiltonian simulation of symmetric toric shapes. As the energy penalty associated to the presence of a vortex core is removed from the simulated torus shape [79], a torus adds a strong incentive to have a finite component of toroidal moment (and no homogeneous polarization contrary to a cube under short-circuit boundary condition) and, as we will show it in the description of the low temperature state, paves a way to a complex local polarization ordering. One of these possible local polarization orderings was a transverse hypertoroidal moment arising in asymmetrical nanotori [31] and simulations with external electric field lead to switching of this parameter. Yet, experimentally obtaining such shapes is difficult, whereas symmetrical ferroelectric nanotori seem more easy to grow.

6.1.1 Torus construction

In simulations performed along this chapter, mathematical definition of a solid torus with major radius R and minor radius r that is represented in figure 6.1 provided a criterion distinguishing sites inside a supercell. Due to enormous strain of the order of magnitude of the ratio between

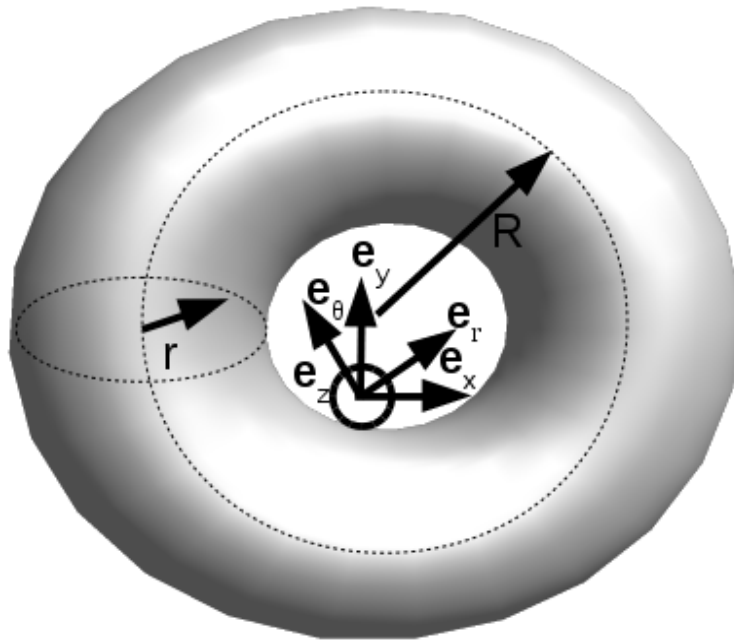


FIGURE 6.1: Simulated Barium Titanate shapes having major radius R and minor radius r .

torus minor to major radius ratio that can occur in such configurations, experimental insight allowed to discard the idea of a structure [80] in which atomic planes form concentric circles [81]: in all subsequent simulations, the sites were set to be lying on a cubic grid. A torus shape was obtained by deciding that the sites having coordinates verifying equation 6.1 were simulated as

Barium Titanate whereas other sites represented vacuum.

$$\left(\sqrt{x^2 + y^2} - R\right)^2 + z^2 < r^2 \quad (6.1)$$

During all the study, the number of sites inside the torus was kept approximately constant at $N=2400$ even when the shape of the torus enclosed in the simulation box was modified. In an analogy to modelling of a vacuum layer on dot surface, sites representing vacuum have elastic constants set to match those of Barium Titanate but local mode and inhomogeneous strain set to zero.

6.1.2 Electrical boundary conditions

Cubic geometry gave a specific role to perfectly periodic boundary conditions. In that case, simulating an infinite array of dipole images leads to same electric potential on opposite parallelepiped simulation cell surfaces that also become equipotentials. This simulation situation is physically equivalent to having shorted metal plates on both surfaces. A torus surface is a little more difficult to describe. Periodic electrical boundary condition still represents an infinite amount of dipole tori copies but the resulting electric potential will be the same only on the opposite surfaces of the parallelepiped that surrounds the torus: it will not be the same on any two opposite points of the surface of the toric particle itself. Thus, periodic boundary condition no longer provides a convenient numerical technique to simulate perfect screening of the torus by free charges, that translated into depolarization coefficient $\beta = 1$. Dipole-dipole interaction with no periodic copies implying $\beta = 0$ does not lead to the same problem, as there are no screening charges to account for. Linear combinations of the two electrical dipole-dipole interaction matrix allowing simulation of various values of depolarization coefficient β are ruled out due to invalidity of the $\beta = 1$ case and all simulations in this chapter were performed under open-circuit $\beta = 0$ boundary conditions, as in [82].

6.1.3 Local polarization representation

Finite values of polarization existing only inside the torus by construction, integral lines following equation 6.2 represent a possibility to emphasize subtle polarization ordering.

$$\mathbf{p} \times d\mathbf{l} = \mathbf{0} \quad (6.2)$$

6.2 Geometry-dependent transitions

Torus dimensions were varied in simulations and sequences of phase transitions changed accordingly, but the high temperature configuration always exhibited no ordering of dipole moments at

all, which is associated to a completely disordered polarization field lines pattern shown in figure 6.2 that corresponds to the highest observed symmetry point group ∞/mmm , except that the dipole grid has $4/mmm$ symmetry.



FIGURE 6.2: Local polarization field lines at $T = 450$ K for a torus included in a $38 \times 38 \times 9$ box.

6.2.1 Torus having small minor to major radius ratio

A simulation performed into a rectangular box comprising $77 \times 77 \times 7$ sites is considered as describing a case of a torus having minor radius very small with regard to major radius. Strain evolution of diagonal components as a function of temperature shows a transition occurring at a temperature $T \approx 85$ K. Two diagonal components along $[100]$ and $[010]$ show an increase whereas the $[001]$ component decreases as can be seen in the left part of figure 6.3. Off-diagonal components of strain do not evolve during transition as represented in the right part of figure 6.3, and this can lead into thinking that the cubic grid of five-atom sites becomes a tetragonal one, with

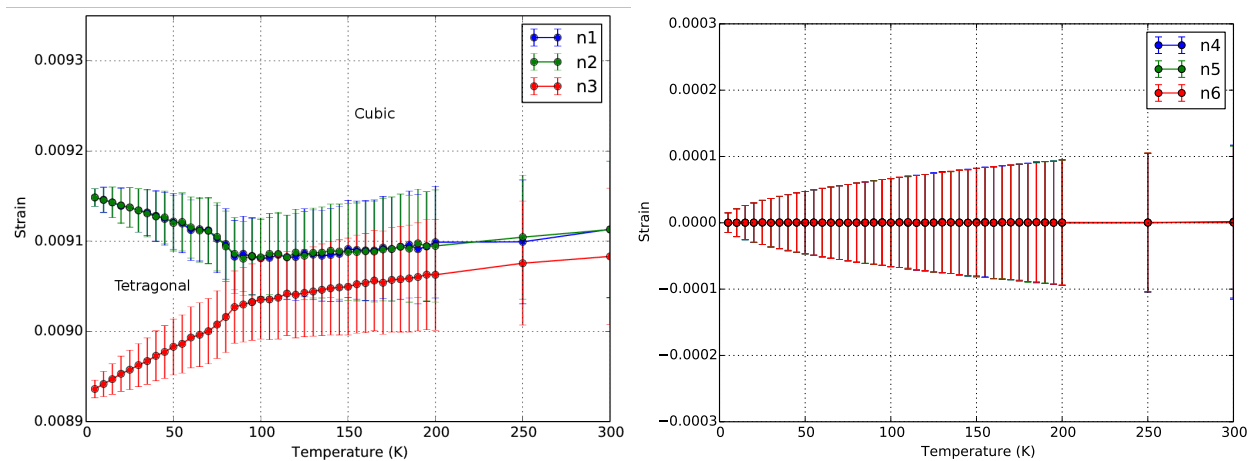


FIGURE 6.3: Diagonal (left) and off-diagonal (right) components of strain evolution as a function of temperature for a torus included in a $77 \times 77 \times 7$ box.

nents of strain do not evolve during transition as represented in the right part of figure 6.3, and this can lead into thinking that the cubic grid of five-atom sites becomes a tetragonal one, with

two dimensions larger than the third. Homogeneous polarization components are plotted in figure 6.4 with a scale comparable to the case of a cube under short-circuit boundary conditions. Depolarization coefficient being set to $\beta = 0$, polarization remains at negligible levels with respect to partially screened cube cases. Figure 6.5 reproduces toroidal moment components as a func-

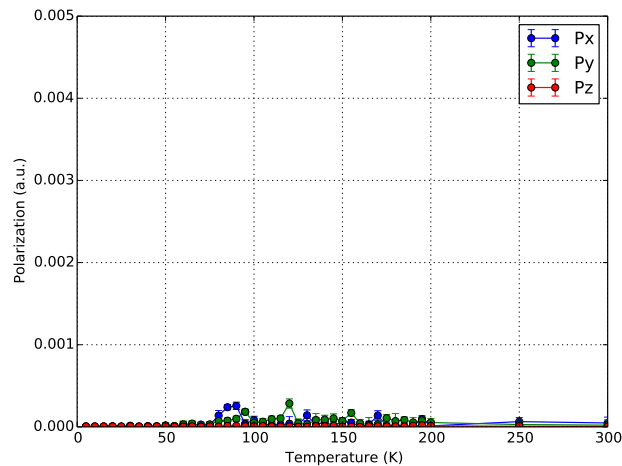


FIGURE 6.4: Temperature evolution of components of polarization for a torus included in a $77 \times 77 \times 7$ box.

tion of temperature. Virtually no toroidization is observed along directions [100] and [010] and a transition essentially distinguishes a high temperature structure having no toroidization at all and a low temperature one having large toroidization along a [001] direction. A circular polarization

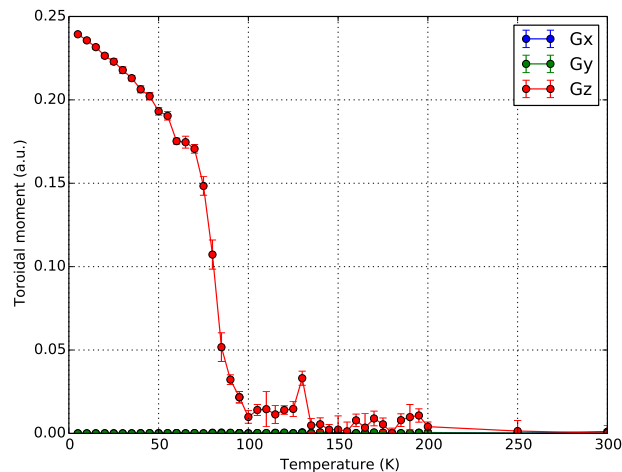


FIGURE 6.5: Temperature evolution of components of toroidization for a torus included in a $77 \times 77 \times 7$ box.

field lines pattern shown in figure 6.6 at low temperature confirms toroidization is the sole order parameter arising in the system, and the pattern symmetry point group is apparently ∞/m

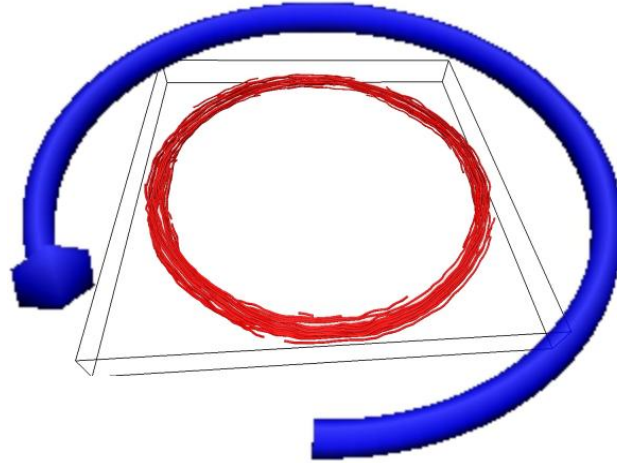


FIGURE 6.6: Local polarization field lines at $T = 5$ K for a torus included in a $77 \times 77 \times 7$ box.

6.2.2 Torus having close minor and major radius

In another torus geometry included in a $23 \times 23 \times 12$ box and thus having minor radius r and major radius R of same order of magnitude, additional features appear. The left part of figure 6.7 reproduces a succession of two transitions affecting normal strain. A decrease of a component along $[001]$ occurs first at $T \approx 105$ K whereas components along $[100]$ and $[010]$ increase simultaneously. A second transition from a diminishing $[001]$ component to an increasing one then occurs near $T \approx 50$ K. Shear strain remains negligible during both transitions as shown in the right part of

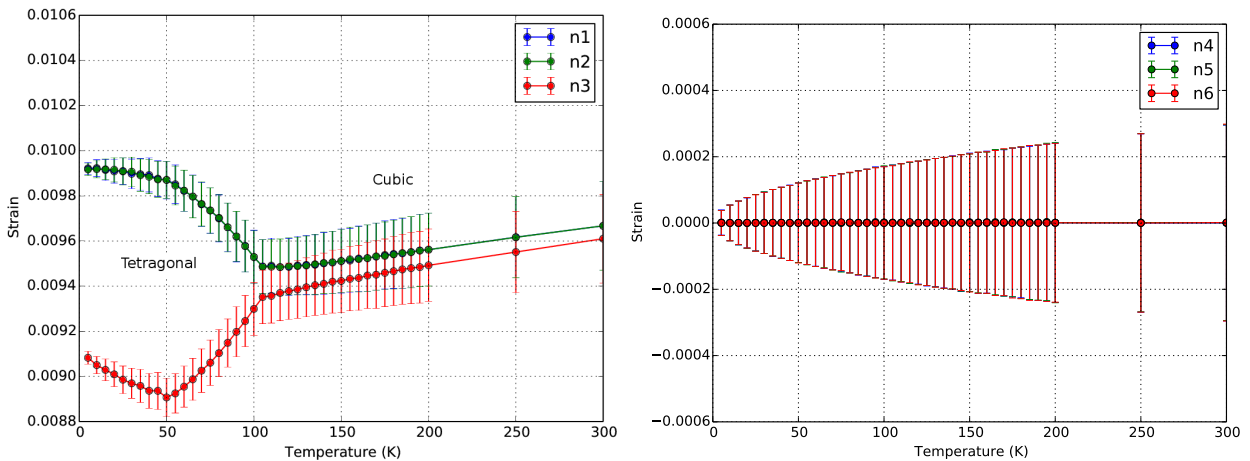


FIGURE 6.7: Normal(left) and shear(right) strain evolution as a function of temperature for a torus included in a $23 \times 23 \times 12$ box.

figure 6.7, and this shows that the cubic grid of five-atom sites becomes a tetragonal one, with two dimensions larger than the third and stays so even after a second transition. Figure 6.8 represents,

with a scale comparable to the case of a cube under short-circuit boundary conditions, all components of homogeneous polarization remaining negligible due to open-circuit boundary conditions. All toroidal components as functions of temperature are reproduced in figure 6.9. Absence

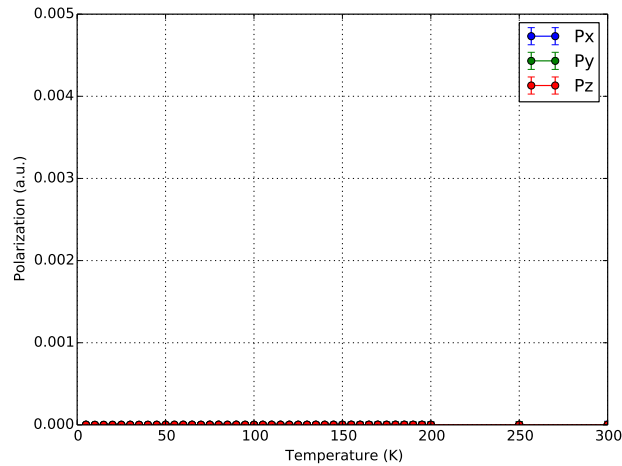


FIGURE 6.8: Homogeneous polarization components at several temperature for a torus included in a $23 \times 23 \times 12$ box.

of toroidization along directions $[100]$ and $[010]$ occurs again and the low temperature structure essentially has large toroidization along a $[001]$ direction in opposition to a non-toroidized high temperature phase. No effect of a second transition observed in strain affects toroidal moment at $T \approx 50$ K. Figure 6.10 reproduces a low temperature simulation result in terms of field lines pattern.

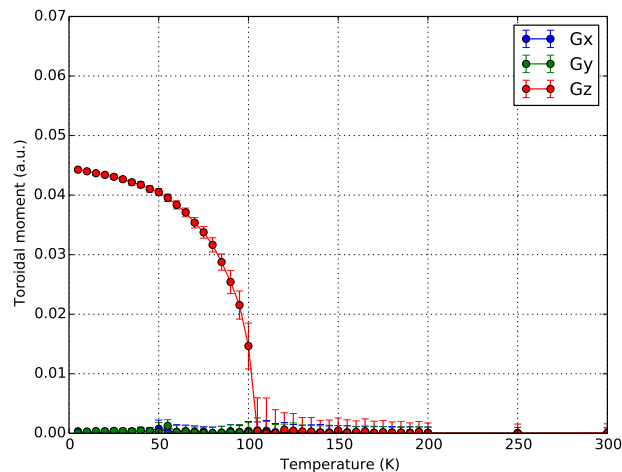


FIGURE 6.9: Toroidization components at various temperatures for a torus included in a $23 \times 23 \times 12$ box.

As none are purely circular, an additional order parameter has to complement pure toroidization to describe a local polarization structure. A preferred order parameter has to describe ordering of local dipoles along the torus poloidal direction. The symmetry point group of the pattern appears to be ∞ and does not contain an inversion symmetry element.

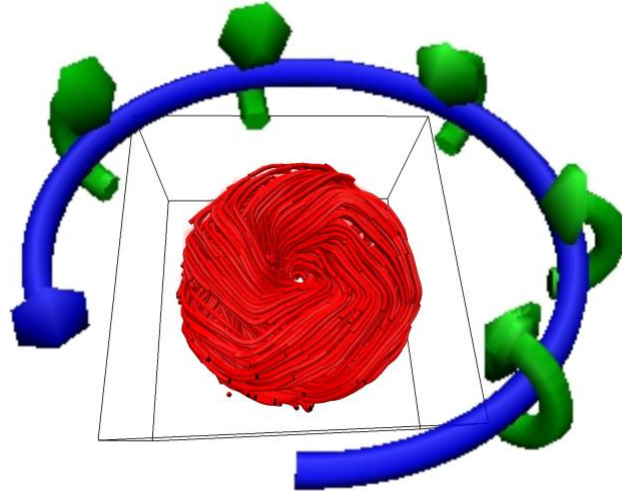


FIGURE 6.10: $T = 5$ K local polarization field lines for a torus included in a $23 \times 23 \times 12$ box.

6.2.3 Intermediate major to minor torus radius ratio

Existence of two limiting cases with different patterns of polarization leads to studying intermediate geometries such as a torus included in a $38 \times 38 \times 9$ box. Another new low-temperature state was obtained, even though numerous similarities with a behavior reported for a $77 \times 77 \times 7$ case existed. Temperature changes modify values of normal strain that exhibits a clear transition occurring at a temperature $T \approx 100$ K. Normal strain components along $[100]$ and $[010]$ increase whereas a $[001]$ component diminishes as can be seen in the left part of figure 6.11. Shear strain components

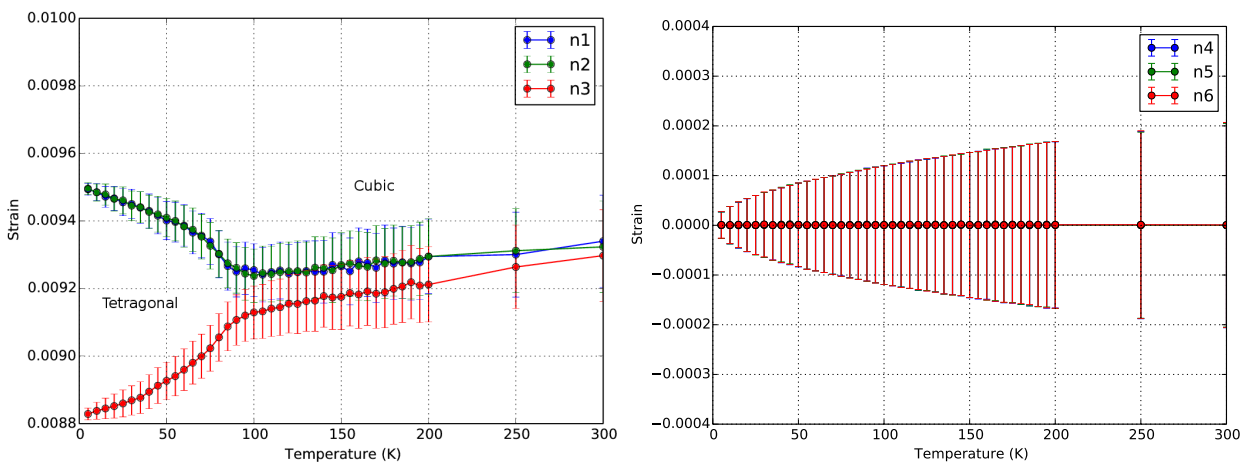


FIGURE 6.11: Normal(left) and shear(right) strain evolution as a function of temperature for a torus included in a $38 \times 38 \times 9$ box.

represented in the right part of figure 6.11 remain very weak in the entire temperature range, and this corresponds to the cubic grid of five-atom sites becoming again a tetragonal one, with two dimensions larger than the third. Homogeneous polarization components are plotted in figure 6.12. Depolarization coefficient being again fixed at $\beta = 0$, negligible levels of polarization with a

scale comparable to the case of a cube under short-circuit boundary conditions are again observed. Figure 6.13 represents all toroidal moment components as a function of temperature. Negligible

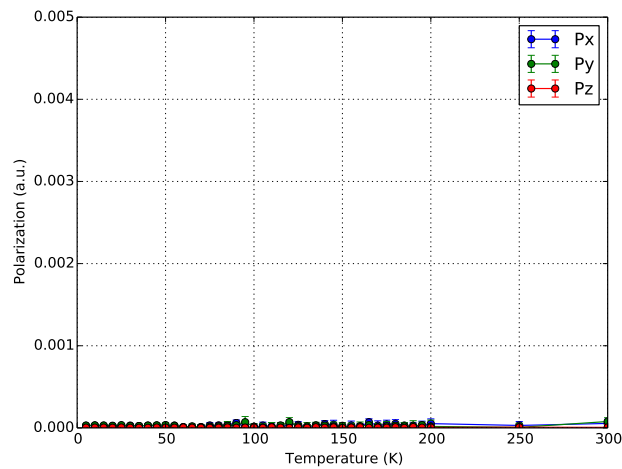


FIGURE 6.12: Temperature evolution of polarization components for a torus included in a $38 \times 38 \times 9$ box.

toroidization is reported along directions [100] and [010] and a transition occurs between a high temperature structure having no toroidization at all and a low temperature one having values of toroidization along a [001] direction that are intermediate between those reported in a $23 \times 23 \times 12$ box and a $77 \times 77 \times 7$ one. Polarization field lines are no longer circles contained in horizontal

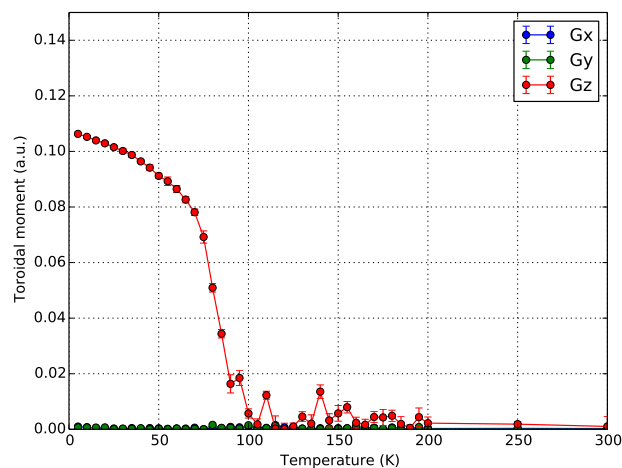


FIGURE 6.13: Temperature evolution of components of toroidization for a torus included in a $38 \times 38 \times 9$ box.

planes and exhibit some degree of analogy with figure 6.10. A pattern obtained at $T = 5$ K shown in figure 6.14 confirms that polarization again has components along a poloidal direction but that sign of these components changes with azimuth and the eight reported nodes point at a symmetry point group being $\bar{8}$. A local order parameter accurately describing poloidal components of polarization has to give rise to spatial oscillations.

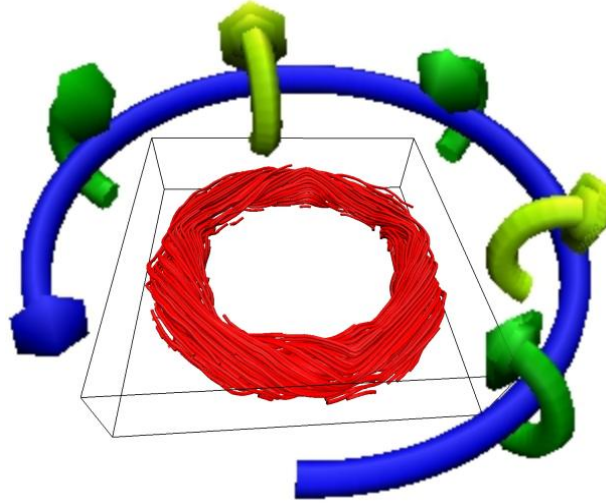


FIGURE 6.14: Local polarization field lines at $T = 5$ K for a torus included in a $38 \times 38 \times 9$ box.

6.3 Beyond toroidal moment

Several polarization states were mentioned to have an ordering that did not lead to circular field lines. Toroidal moment perpendicular to circles is no longer sufficient to describe low temperature states.

6.3.1 Another charge moment

Geometric observation of poloidal polarization in figure 6.10 shows that dipoles form vortices perpendicular to an e_θ direction of figure 6.1. A moment with respect to any parametric curve \mathcal{C} can be computed (6.4) with, for any site position \mathbf{r}_i inside the simulation supercell a vector distance $\mathbf{d}_\mathcal{C}(\mathbf{r}_i)$ from this point to the nearest point $\mathbf{r}_i - \mathbf{d}_\mathcal{C}(\mathbf{r}_i)$ that belongs to \mathcal{C} . A unitary tangent vector at such a point writes $\mathbf{t}_\mathcal{C}(\mathbf{r}_i - \mathbf{d}_\mathcal{C}(\mathbf{r}_i))$.

$$\mathbf{G}_\mathcal{C} = \frac{1}{2Nv} \sum_i (\mathbf{d}_\mathcal{C}(\mathbf{r}_i) \times \mathbf{p}_i) \cdot \mathbf{t}_\mathcal{C}(\mathbf{r}_i - \mathbf{d}_\mathcal{C}(\mathbf{r}_i)) \quad (6.3)$$

$$= \frac{1}{2Nv} \sum_i (\mathbf{t}_\mathcal{C}(\mathbf{r}_i - \mathbf{d}_\mathcal{C}(\mathbf{r}_i)) \times \mathbf{d}_\mathcal{C}(\mathbf{r}_i)) \cdot \mathbf{p}_i. \quad (6.4)$$

In the case of parametric curve \mathcal{C} being a straight line, toroidal moment definition along direction of such a line can be recovered. Another special case is that of a parametric circular curve located at the core of simulated torus shape and having same radius R (6.5).

$$\begin{aligned} \mathcal{C} : [0, 2\pi] &\rightarrow \mathbb{R}^3 \\ \theta &\mapsto (R\cos(\theta), R\sin(\theta), 0). \end{aligned} \quad (6.5)$$

Expressions of vector distance to circle \mathcal{C} (6.6) and tangent vector at nearest point of \mathcal{C} (6.8) are derived.

$$\mathbf{d}_{\mathcal{C}}(x, y, z) = \quad (6.6)$$

$$\left(x - Rx/(x^2 + y^2)^{1/2}, y - Ry/(x^2 + y^2)^{1/2} \right) \quad (6.7)$$

$$\mathbf{t}_{\mathcal{C}} \left(Rx/(x^2 + y^2)^{1/2}, Ry/(x^2 + y^2)^{1/2}, 0 \right) = \left(-y/(x^2 + y^2)^{1/2}, x/(x^2 + y^2)^{1/2}, 0 \right). \quad (6.8)$$

Overall expression of polarization moment with respect to parametric circle \mathcal{C} (6.9) can then be computed.

$$\mathbf{G}_{\theta} = \frac{1}{2Nv} \sum_i \left(x_i z_i \mathbf{p}_{ix} / (x_i^2 + y_i^2)^{1/2} + y_i z_i \mathbf{p}_{iy} / (x_i^2 + y_i^2)^{1/2} + \left(R - (x_i^2 + y_i^2)^{1/2} \right) \mathbf{p}_{iz} \right). \quad (6.9)$$

Expression of toroidal moment being the description of polarization curl, an axial component of toroidization curl also called hypertoroidal moment (4.9) describes local polarization forming vortices along \mathbf{e}_{θ} . With respect to equation 6.9, expression in cartesian coordinates of hypertoroidal moment (6.10) only adds a polarization term $\sum_i R \mathbf{p}_{iz}$ that can be neglected in simulations leading to absence of homogeneous polarization and a radial distance to cylindrical axis factor that resembles a constant in cases where major radius is large compared to minor radius.

$$\mathbf{H}_{ez} = \frac{1}{4Nv} \sum_i \left(x_i z_i \mathbf{p}_{ix} + y_i z_i \mathbf{p}_{iy} - (x_i^2 + y_i^2) \mathbf{p}_{iz} \right). \quad (6.10)$$

Simulated poloidal polarization field lines components can thus be described in terms of axial hypertoroidal moment components.

A change of origin must not affect values of an order parameter. The summation of local dipole moments expressing homogeneous polarization does not need additional calculations to become origin-independent. Toroidal moment fulfills such a criteria provided that it is computed with the inhomogeneous part of polarization (6.11).

$$\delta \mathbf{p}_i = \mathbf{p}_i - \frac{1}{N} \sum_j \mathbf{p}_j \quad (6.11)$$

An expression of hypertoroidal moment that does not depend on origin choice is reproduced in equation 6.12.

$$\mathbf{H}_e = \frac{1}{4Nv} \sum_i \left[\mathbf{r}_i \times (\mathbf{r}_i \times \delta \mathbf{p}_i) + \mathbf{r}_i \times 2v\mathbf{T} - \frac{1}{N} \sum_j \mathbf{r}_j \times (\mathbf{r}_i \times \delta \mathbf{p}_j) \right] \quad (6.12)$$

Using Jacobi identity and changing summation order in third term of equation 6.12 results in another equation 6.13 that can be combined with definition of a supercell-centered set of coordinates $\sum_i \mathbf{r}_i = \mathbf{0}$ to allow use of double cross product of dipole position with local polarization as a

simplified expression of origin-independent toroidal moment.

$$\frac{1}{4Nv} \sum_i \left[-\frac{1}{N} \sum_j \mathbf{r}_j \times (\mathbf{r}_i \times \delta \mathbf{p}_j) \right] = -\frac{1}{4Nv} \sum_i [\mathbf{r}_i \times 2v\mathbf{T}] + \frac{1}{4N^2v} \sum_j \left[\mathbf{r}_j \times \left(\delta \mathbf{p}_j \times \sum_i \mathbf{r}_i \right) \right] \quad (6.13)$$

6.3.2 Geometry-dependent temperature behavior

A case in which minor to major radius is very small was described by simulations performed on a torus included in a $77 \times 77 \times 7$ box. No other ordering than homogeneous toroidization along a [001] axis was observed. Figure 6.15 representing [001] component of hypertoroidal moment as a function of temperature remaining negligible confirms absence of poloidal ordering. In fact,

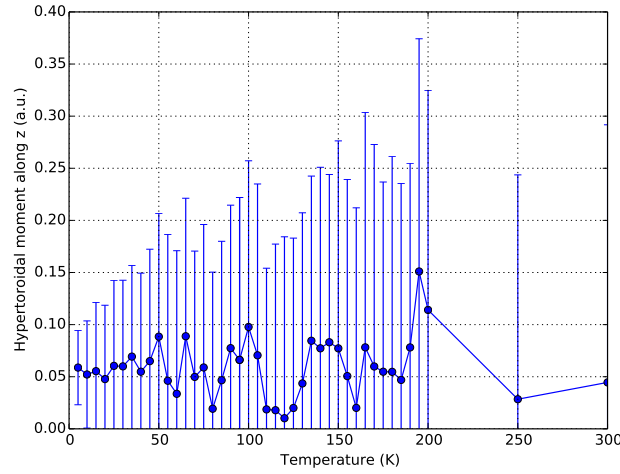


FIGURE 6.15: Torus included in a $77 \times 77 \times 7$ box: hypertoroidal moment along z-axis as a function of temperature.

prior effective Hamiltonian simulations were performed on PZT nanorings, even though the hole of these rings was off-centered, and evidenced a very similar behavior: only toroidal moment was reported [83]. Another limit of very close minor and major radius values was studied by focusing on a $23 \times 23 \times 12$ box containing simulated torus. An additional transition was observed at $T \approx 50$ K. Hypertoroidal moment along [001] rises from zero at high temperature to finite values on figure 6.16 and describes a poloidal component that was observed on a low temperature field lines pattern. It must be stressed that the low temperature phase does not have hypertoroidal moment alone as this was considered in prior works by Gorbatshevich *et al.* [84], Scott *et al.* [85] or Zhu *et al.* [86]. There is a coexistence between this hypertoroidal moment and the toroidal moment. Due to this combination, the field lines of figure 6.10 do not superimpose with their image in a mirror plane or, in other words, their symmetry point group ∞ is chiral. As a consequence, the resulting structure is chiral and two circularly polarized electromagnetic waves do not necessarily propagate at the same speed. Similar behavior was simulated in a composite containing an array

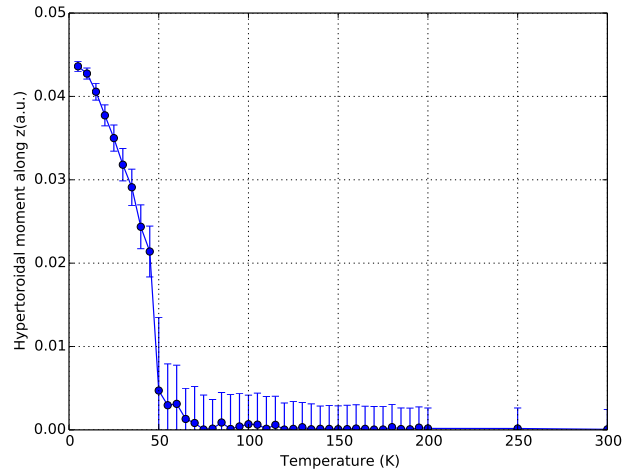


FIGURE 6.16: Hypertoroidal moment along z-axis at several temperatures for a torus included in a $23 \times 23 \times 12$ box.

of BTO nanowires penetrating a STO matrix due to the coexistence of a toroidal moment with homogeneous polarization [87].

Intermediate values of major to minor radius ratio were simulated with a torus inside a $38 \times 38 \times 9$ box. Large fluctuations occur again near $T \approx 50$ K, but no hypertoroidal moment along [001] is present at lower temperatures. Figure 6.17 represents an absence of description of a phase transition by hypertoroidal moment whereas corresponding field lines pattern seemed to exhibit poloidal components. Cancellation of a sum of hypertoroidal moments inside all a simulation

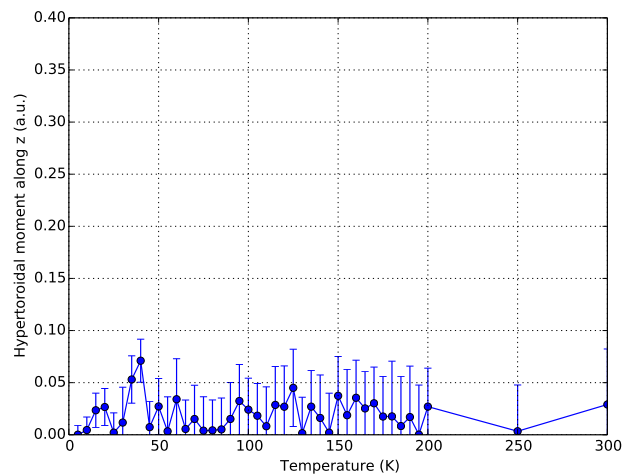


FIGURE 6.17: Torus included in a $38 \times 38 \times 9$ box: temperature evolution of hypertoroidal moment along z-axis.

cell could come from absence of any hypertoroidal moment everywhere or from a coexistence of zones having opposite values of hypertoroidal moment. Azimuth being a parameter along which hypertoroidal moment in figure 6.14 oscillates, average hypertoroidal moment at a given θ

coordinate was computed after a truncated ($K=7$) sum described in equation 6.15.

$$\langle h_{ez} \rangle_{\rho,z}(\theta) = \frac{1}{2K+1} \sum_i h_{ezi} \left[1 + 2 \sum_{k=1}^K \left(T_k \left(\frac{x_i}{(x_i^2+y_i^2)^{1/2}} \right) \cos(k\theta) + \frac{y_i}{(x_i^2+y_i^2)^{1/2}} U_{k-1} \left(\frac{x_i}{(x_i^2+y_i^2)^{1/2}} \right) \sin(k\theta) \right) \right] \quad (6.14)$$

$$(6.15)$$

In equation 6.15, T_k and U_k represent Chebyshev polynomials of first and second kind whereas h_{ezi} represents local z-axis hypertoroidal moment at site i . Hypertoroidal moment average as a function of azimuth θ can then be plotted in figure 6.18 for a cube inside a $38 \times 38 \times 9$ box at a temperature $T = 5$ K. Presence of eight nodes and absence of a constant component confirm can-

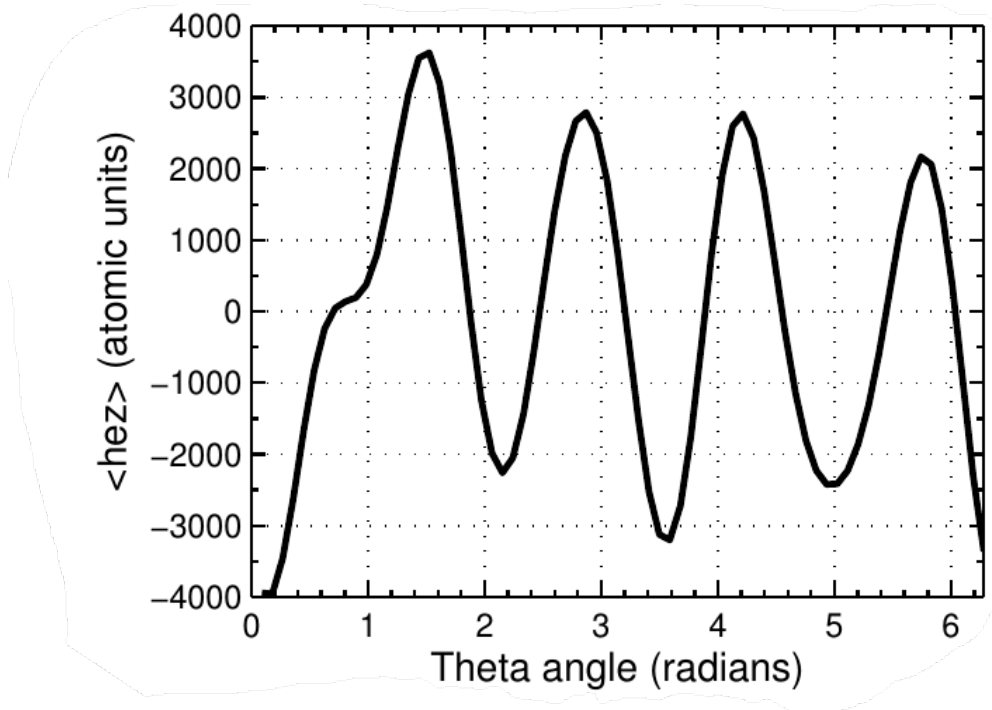


FIGURE 6.18: Azimuthal dependence of hypertoroidal moment along z-axis for a torus included in a $38 \times 38 \times 9$ box at $T = 5$ K.

cellation of average hypertoroidal moment but does not mean that it is negligible over the whole torus. Hypertoroidal moment oscillations coexisting with toroidal moment can be described as phase IV, homogeneous hypertoroidal and toroidal moment being written as phase III, toroidal moment alone becoming phase II and phase I meaning absence of any polarization ordering leads to construction of a phase diagram reproduced in figure 6.19. Aspect ratio a represents a dimensionless number describing torus shape and resulting from division of minor radius by major radius.

6.3.3 Electric field cycling

Monte-Carlo Metropolis methods can lead to slightly misleading results on attempting to simulate results from dynamics but response to external excitations represents a desired feature each time

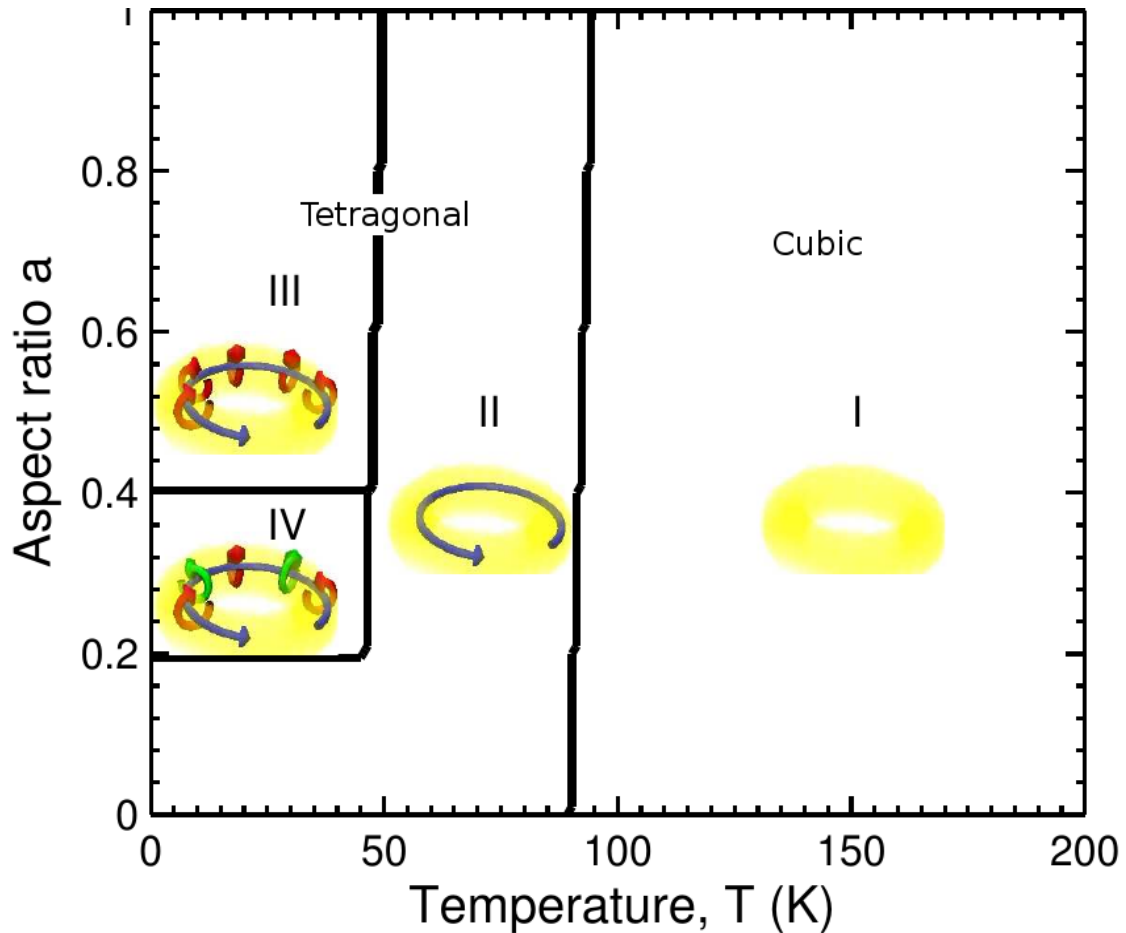


FIGURE 6.19: Aspect ratio versus temperature phase diagram.

an order parameter is evidenced. Homogeneous electric field along a nanotorus main axis was the focus of attempts to interact with a homogeneous hypertoroidal moment arising in phase III. Space inversion leads to a change in sign of homogeneous polarization and homogeneous electric field that are coupled energetically. Space inversion does not affect homogeneous toroidization sign and any coupling to electric field is thus forbidden. Homogeneous hypertoroidal moment exhibiting a sign change under space inversion, possible coupling to homogeneous electric field along torus main axis was investigated as in figure 6.20. Monte-carlo simulations were performed under an increase followed by a decrease and an increase of homogeneous electric field to obtain loops. Several features of coupling between electric field excitation and switching between two stable states have appeared: two values of hypertoroidal moment existed without external excitation and a reversible jump in hypertoroidal moment occurred on cycling electric field. However, on applying finite electric field, two different total energy values for the two different hypertoroidal moment states were not observed so the observation of switching can also be a spurious effect due to the use of a Monte-Carlo simulation on probing the evolution of the system: only the result of a Molecular Dynamics simulation can unambiguously confirm the modification of hypertoroidal moment by homogeneous electric field.

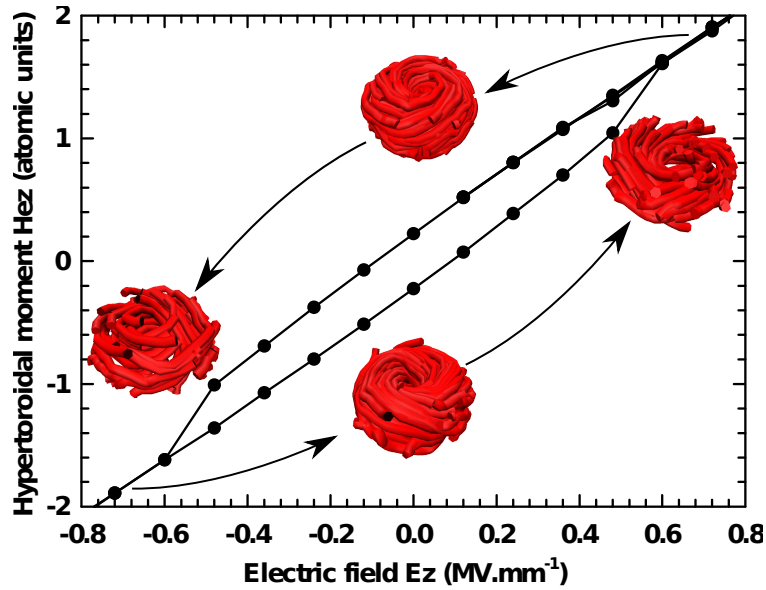


FIGURE 6.20: Hypertoroidal moment along z-axis recorded under various applied electric fields.

6.4 Conclusion

Modeling nanotori can be done in several ways, depending on the crystal structure of the particles. Atomic planes can form concentric structures but this causes significant strain. Consequently, a parallelepipedic simulation cell was used and sites in which local dipole moment arise remained on a cubic grid. Inside the simulation cell, some sites location coordinates satisfied an inequation that ensured they were inside the ferroelectric torus and, as such, they were assigned the effective Hamiltonian description of Barium Titanate. Other sites were outside the torus and were modeled by vacuum through setting inhomogeneous strain and local polarization to zero. However, the problem of boundary conditions was different from the case of a hollow cube. In particular, Short-Circuit boundary conditions require free charges to compensate the normal electric field due to bound charges at the surface of the torus. The computed dipole-dipole expression in Short-Circuit conditions rather describes charge compensation occurring on the surface of the parallelepiped inside which the torus is simulated. Consequently, all simulations performed in this part had Open-Circuit boundary conditions. A summary about simulations performed with three types of geometries keeping total number of dipole sites constant but altering ratio between torus minor and major radius was provided first. If minor radius is greatly smaller than major radius, a vortex along the torus main axis is observed at low temperatures. A description of an additional ordering was provided afterwards: if minor radius is slightly smaller than major radius, the vortex coexists with a polarization that is along a poloidal direction and can be described in terms of hypertoroidal moment. In between, a phase exhibiting spatial oscillations of this new order parameter was numerically evidenced. External excitation interplay with hypertoroidal moment were considered.

Conclusion and prospects

IN this thesis, Barium Titanate nanostructures have been studied from a polarization point of view. We combined numerous experimental syntheses with numerical simulations of as-obtained shapes.

Transitions in ferroelectric perovskites Ferroelectric materials represent an intriguing topic due to their ability to retain a spontaneous polarization even in the absence of externally applied electric field below Curie temperature. More specifically, crystalline solids can be classified according to the structure of the elements of symmetry that leave primitive cell invariant combined with translation-associated operations into 230 symmetry groups. Among all the point groups that are compatible with translations, ten of them are polar. The microscopic mechanism of onset of the transition can be displacive or order-disorder. Several possible directions of spontaneous polarization in a three-dimensional material allow observation of a sequence of several structural phase transitions. Coefficients of a polynomial describing Landau-Devonshire free energy at any temperature can be extracted from experimental data and its minimization reproduces the experimentally observed transitions. Depending of the presence or absence of a coexistence of phases, the transitions are of first or second order. However, this theory is phenomenological and, as such, non predictive. A predictive method has to solve the electronic problem after decoupling it from nuclei positional degrees of freedom through Born-Oppenheimer approximation. A method of choice is Density Functional Theory, in which computation of ground state energy deal with the electronic density rather than all the electron wavefunctions. This method allows insight into the stable structure at zero temperature and additional steps are required to obtain finite temperature properties. Namely, an expansion is performed around a cubic structure and coefficients representing derivatives of energy with regard to atomic displacements are derived. This effective Hamiltonian is then used in Metropolis simulations to provide observables estimations at finite temperatures. Short-range interactions usually require the values of parameters at neighbouring crystal lattice sites and this poses the problem of boundary conditions on surfaces. Moreover, dipole-dipole interaction can be computed in the periodic case, which happens, for a cube, to correspond to Short-Circuit boundary condition or in the isolated particle one for Open-Circuit boundary conditions. Literature review then continued with simulations performed in composites or isolated particles using this effective Hamiltonian and the complex dipole pattern of ordering that emerged in them.

Solvothermal syntheses Soft chemistry routes able to produce ternary oxide particles were described. Experimentally, Barium Titanate is a mixed oxide which can be synthesized in several ways. Solid state reaction between Titanium Dioxide and Barium Oxide represents the most common route. However, this method requires long reaction times and high synthesis temperature for interdiffusion of ions to take place and this does not allow formation of nanostructures due to grain growth. Synthesis in a solvent offers an alternative, but it is often limited by solvent boiling point. Through use of a pressure vessel, reagents can be heated significantly above the solvent boiling temperature and nanometric particles of Barium Titanate are grown. A two-step route was preferred: $\text{Na}_2\text{Ti}_3\text{O}_7$, $\alpha - \text{K}_2\text{Ti}_6\text{O}_{13}$ and $\text{H}_2\text{Ti}_3\text{O}_7$ are the three types of titanium precursor nanorods or nanotubes that were produced during the first step. The nature of the intermediate product was evidenced as being of interest in order to tune the Barium Titanate obtained particle geometry after a second solvothermal step was conducted and allowed topotactical replacement of a cation by Barium: agglomerated nanospheres, individual nanospheres, individual nanocubes, mixing of nanospheres and nanotori and individual nanotori were obtained and X-Ray diffraction confirmed that all these products were Barium Titanate. The precursor was not the only tunable parameter and influence of reaction temperature or concentration of $\text{Ba}(\text{OH})_2$ was also considered.

Morphogenesis processes at play As various different single crystalline Barium Titanate nanoshapes were obtained, growth mechanisms involved were investigated. In particular, it was shown that products shapes are not necessarily related to that of reagents, even though characteristic sizes remain of the same order of magnitude. In the case of nanospheres, an evolution from products aggregated on the precursor overall shape at low temperature to growth of individual particles at high temperatures was observed. Diffusion processes of species along a precursor particle lead to a toy model inspired from Turing reaction-diffusion adapted to a nanotube precursor so as to justify production of nanotori. Additional observation of nanotori through Transmission Electron Microscopy gave insight in the organisation of atomic planes: these are not concentric. Production of a mix of nanospheres and nanotori was achieved and growth of nanocubes was also reported. The Transmission Electron Microscopy observation of these nanocubes revealed that some of them were hollow. Factors influencing product shape were shown to be not only precursor type but also temperature and Ba/Ti molar ratio. Ostwald ripening favours large spherically shaped particles so as to minimize surface tension and was invoked as a growth mechanism. Faster outward migration of an exiting cation than inward diffusion of Barium is called Kirkendall effect. It results in production of vacancies that merge at the core of a nanorod and transform it into a nanotube. Further shape change leading to solid or hollow cubes was assumed to come from self-rebuilding and merging-rebuilding processes.

On the parameters describing a distribution of charge and the case of inhomogeneous permittivity To begin with, a decomposition in moments of charge was introduced. Multipolar

expansion represents a framework describing distribution of charges and additional terms were observed to arise in numerical simulations of isolated ferroelectric particles: the special case of an ensemble of dipoles located on a cubic grid can give rise to toroidal or even hypertoroidal moments. In an attempt to present all the possible order parameters constructed from $(n-1)$ -th power of position-polarization, we showed that this object had the properties of a tensor. Linear combinations of components can form sets that are invariant under a rotation of the coordinate system and it was shown the components of toroidal and hypertoroidal moments are some of those. Moreover, observation of hollow cubes let us think that high-permittivity solvent could be trapped in the inclusion. It lead to an investigation of whether it was possible to compute dipole-dipole interaction in a medium that had inhomogeneous permittivity. There was no analytical expression for the case of a non-periodic simulation cell. The intersite interaction term can be derived but the interaction between a dipole and its own copies cannot be obtained in the case of a periodic simulation cell with inhomogeneous permittivity.

Hollow nanodots and consequences of the presence of a cavity Effective Hamiltonian provides a first-principles derived expression of energy as a function of distortions that can be used in a Metropolis simulation to get temperature-related properties. A sequence of phase transitions on cooling from cubic to tetragonal followed by tetragonal to orthorhombic and orthorhombic to rhombohedral is simulated on using periodic boundary conditions to reproduce the experimentally characterized bulk. Presence of surfaces can modify the result: in this work, the effective Hamiltonian of bulk was used again with modified boundary conditions. Linear combinations between Open-Circuit and Short-Circuit boundary conditions were used for electrostatic interaction. A layer of sites in which inhomogeneous strain and local polarization are set to zero was added on the surfaces in order to remove any effect of periodic boundary conditions from the computation of short-ranged energy interactions. This provided a way to replace some sites by a medium resembling vacuum and was subsequently used as a method to simulate the hollow cubes that had been synthesized. Thus, simulations were conducted on $15 \times 15 \times 15$ sites including a surrounding layer representing vacuum and a cubic inclusion at the center that also used this vacuum model.

Larger hole size was expected to give rise to a transition from homogeneous polarization to a vortex state in intermediate boundary conditions. The hollow and solid cubes gave completely similar results in the case of completely Open-Circuit or Short-Circuit boundary conditions: a vortex for Open-Circuit boundary conditions and homogeneous polarization for Short-Circuit boundary condition. Transition from one type of behavior to the other occurred under intermediate boundary conditions at a critical depolarization coefficient. The value of this critical depolarization coefficient was changed for hollow cubes: the larger the inclusion, the smaller the critical depolarization coefficient, which is a very counterintuitive result and represents the opposite of what was expected. However, as many experimentally produced nanocubes apart from those of

this work are possibly also hollow, the fact that a hole tends to favour a homogeneously polarized state is in agreement with experimental difficulties to observe vortices.

Ferroelectric nanotori and solenoidal polarization field lines The crystal structure of the nanotorus represents a significant part of the modeling. If a symmetrical strained structure is produced, these atomic planes appear as concentric lines. This was ruled out by experimental observation on obtained ferroelectric tori. As a result, the sites that carry the local dipole moments are still placed on a cubic grid and a parallelepipedic simulation cell is used. Inside the simulation box, some sites coordinates satisfy an inequation that ensures they are inside the ferroelectric torus and were simulated with the full effective Hamiltonian whereas others are outside and were simulated by setting inhomogeneous strain and local polarization to zero. Contrary to the case of a hollow cube, periodic boundary condition no longer correspond to short-circuiting the surfaces of the particle. Thus, Open-circuit boundary conditions were used for all the simulations performed in this part. Keeping the number of dipole sites constant but changing the ratio between torus minor and major radius gives mainly three types of result at low temperature. If minor radius is greatly smaller than major radius, a vortex occurs along the torus main axis. If minor radius is just slightly smaller than major radius, the vortex coexists with a polarization that is along poloidal direction, called hypertoroidal moment. The intermediate state gave rise to a vortex and overall hypertoroidal moment being zero. However, this cancellation on average is due to spatial oscillations of hypertoroidal moment. In the case of homogeneous hypertoroidal moment, the first steps in order to study its interaction with a homogeneous electric field were conducted.

General prospects

Work performed during this PhD aimed at understanding how new shapes made of a ferroelectric material could be obtained and simulating resulting polarization field lines at low temperature. Nanometric hollow nanodots and tori were obtained and stimulated interest in numerical simulations of exotic geometries. But, apart from temperature and precursor chemical nature, the set of other relevant tunable parameters offered by solvothermal synthesis is enormous. The nature of the solvent can be changed and affect the solvothermal process through modification of the internal autogenous pressure and of the permittivity of the solvent. Concentration of reagents can also be changed. In fact, the obtained nanotori and hollow nanodots probably represent only a fraction of what could be achieved as other reports mentioned corral-like, starfish-like or sword-like particles. Beyond the toy model that has been proposed for nanotori, the rich literature about phase field modeling possibly represents another path in the numerical study of morphogenesis mechanisms at play during the syntheses. Even though a risk of overpressure can lead to safety concerns, adding an appropriate amount of liquid nitrogen inside the autoclave represents a possible way to perform syntheses under high pressure below solvent boiling temperature, that is to say in conditions that have never been reached before. Numerical simulations were performed

with Barium Titanate as the ferroelectric material of interest and, in the case of nanotori, we observed a phase in which average hypertoroidal moment remained zero whereas local values were finite due to oscillations. A new set of linear combinations of products between dipole position coordinates and local polarization that has been derived in the manuscript and similar sets having higher order can be monitored to see if any of them becomes finite at the transition. Regarding the case of a torus having finite hypertoroidal moment, a Molecular Dynamics study is the best way to confirm or reject the possibility of switching this hypertoroidal moment with homogeneous electric field. As the phase that is switched is chiral, conducting a numerical study of its interaction with a polarized electromagnetic radiation represents a step in possible fabrication of a new type of optical modulator. Memory application provide a driving force to similar studies with lead zirconate titanate. Lastly, studying an isolated nanotorus constituted the core of this thesis but an ordered superlattice made of ferroelectric nanotori regularly dispersed inside a filler material can be of interest in the study of interactions and can even give rise to problems of frustrated ordering.

Chapter 7

Summary in french

LE rôle relatif du volume d'un matériau par rapport à celui de ses surfaces est de l'ordre de sa taille caractéristique. Lorsque cette dimension caractéristique se compte en milliardième de mètre, on peut utiliser le terme de nanomatériau. De telles structures de petite taille sont, dans des domaines aussi variés que peuvent l'être les constituants utilisés, l'objet d'études récentes visant à comprendre comment des propriétés physiques connues peuvent se trouver modifiées dans un tel cadre.

Les matériaux ferroélectriques suscitent un vif intérêt de par leurs propriétés remarquables: au-dessous d'une température dite critique, ils peuvent posséder une polarisation spontanée se traduisant au niveau microscopique par la présence de dipôles tous orientés dans une direction semblable, même en l'absence d'application d'un champ extérieur, deux sens étant possibles. De tels matériaux possèdent également la propriété d'être piezoélectriques, au sens où la valeur de ladite polarisation spontanée peut se trouver affectée par une sollicitation mécanique, et pyroélectriques, cette même polarisation spontanée dépendant également de la température. Parmi l'ensemble des associations de composés chimiques susceptibles de former des arrangements spatialement ordonnés, certaines sont constituées majoritairement d'anions et de cations répartis au sein d'un motif appelé maille élémentaire qui se trouve reproduit en chaque point d'un réseau. Les opérations de symétries laissant cette maille élémentaire invariante forment un groupe et la combinaison de ces éléments avec d'autres transformations comportant des translations entre points du réseau doit également en être un, ce qui classifie les structures cristallines possibles en deux cent trente groupes de symétrie.

Lorsque, par suite de déplacements relatifs des ions, à l'équilibre, le barycentre des charges positives de la structure se trouve devenir disjoint du barycentre des charges négatives, le matériau passe d'une phase dite paraélectrique à une phase ferroélectrique. Le caractère tridimensionnel d'un matériau se traduit par la possibilité d'obtenir une polarisation spontanée de manière équivalente selon plusieurs directions. En moyenne, l'absence de polarisation spontanée dans la phase paraélectrique peut provenir de deux phénomènes distincts: une absence totale de polarisation dans chacune des mailles, auquel cas la transition est dite displacive ou bien une présence de polarisation dont l'orientation variable se traduit par une compensation au niveau de la valeur moyenne, cas dans lequel la transition est dite ordre-désordre. De manière plus détaillée, au

voisinage d'une transition, l'état d'équilibre d'un système peut être trouvé en minimisant une énergie libre dite de Landau qui, dans un cas symétrique et unidimensionnel s'exprime comme un polynôme ne contenant que des puissances paires et faisant porter la dépendance en température uniquement sur le terme parabolique. Selon le signe du terme d'ordre quatre, la transition peut impliquer une coexistence de deux phases s'il s'agit d'une transition du premier ordre ou aucune coexistence s'il s'agit d'une transition du second ordre. Une expression de l'énergie de Landau faisant intervenir l'existence de directions spatialement équivalentes, un paramètre supplémentaire traduisant des déformations élastiques en plus des déformations polaires et un grand nombre de termes ajustés expérimentalement peut permettre de reproduire la majorité des caractéristiques des transitions connues dans un type particulier de cristaux ferroélectriques appelés perovskites. Cependant, cette méthode a l'inconvénient d'être une théorie purement phénoménologique: elle peut rendre fidèlement compte des mesures expérimentales mais elle n'est pas prédictive.

Une méthode prédictive repose d'abord et avant tout sur la possibilité de calculer une énergie associée à une configuration parmi toutes celles permises par les degrés de liberté concernant les positions des noyaux, traités classiquement avec une approximation de Born-Oppenheimer, et ceux liés aux fonctions d'onde des électrons. Après reformulation du problème comme une minimisation de l'énergie associée à une densité électronique donnée, le caractère indiscernable des électrons et la difficulté que représente l'expression d'un terme d'énergie d'interaction entre ces électrons conduit à l'ajout d'un terme dit d'échange-corrélation permettant de travailler avec un système fictif d'électrons indépendants pour lesquels il est possible de résoudre l'équation de Schrödinger. Une minimisation globale de l'énergie donne des informations sur la configuration d'équilibre à température nulle mais pas sur le comportement à température finie. Pour ce faire, un développement perturbatif est conduit autour de la structure la plus symétrique et ses coefficients sont obtenus par la méthode précédente. Un algorithme de Métropolis permet alors de retrouver les valeurs moyennes d'observables à toute température de manière prédictive. Une polarisation se traduisant par la présence de plans de charges liées aux extrémités du matériau, le choix des conditions aux limites peut avoir une importance déterminante sur l'état du système: lorsque des charges libres compensent exactement le champ dû à la présence des charges liées, on parle de condition de circuit fermé, tandis que le cas où aucune charge ne vient compenser ce champ correspond à des conditions de type circuit ouvert. Dans ce dernier cas, de nouvelles configurations de polarisation sont prévues par les simulations, et elles ne sont pas toujours en accord avec les résultats expérimentaux.

Expérimentalement, le Titanate de Baryum est un oxyde dit mixte dont la synthèse peut être réalisée de plusieurs manières. La plus répandue exploite une réaction en phase solide entre le dioxyde de Titane et l'oxyde de Baryum. L'interdiffusion des ions dans ces phases solides requérant des énergies d'activation extrêmement importantes, les temps de réaction sont longs et les températures auxquelles sont réalisées ces synthèses sont telles qu'il y a coalescence des grains au sein des poudres de réactifs. La température à laquelle on peut envisager des réactions en solution est souvent fondamentalement limitée par la température d'ébullition du solvant. Dans le cadre

des méthodes solvothermales qui ont été employées au cours de ce travail, une enceinte capable de supporter de fortes pressions, dite autoclave, permet de porter le milieu réactionnel à une température excédant cette température d'ébullition. Une réaction chimique produisant du Titanate de Baryum peut alors avoir lieu sans que les produits ne perdent leur dimension nanométrique. La synthèse proprement dite se fait en deux étapes: la première aboutit à la formation de nanostructures allongées d'un oxyde mixte contenant du Titane. Les trois oxydes mixtes produits au cours de ce travail furent respectivement $\text{Na}_2\text{Ti}_3\text{O}_7$, $\alpha - \text{K}_2\text{Ti}_6\text{O}_{13}$ et $\text{H}_2\text{Ti}_3\text{O}_7$. Le Titanate de Baryum proprement dit est ensuite obtenu par une seconde synthèse en conditions solvothermales au cours de laquelle le cation associé au Titane diffuse hors de la structure cristalline et se trouve topotactiquement remplacé par le cation Barium. L'analyse des données obtenues par diffraction des rayons X sur le solide obtenu permet directement de constater la nature de ce changement de composition chimique.

De manière peu intuitive, bien que les tailles caractéristiques restent du même ordre de grandeur, la morphologie des particules obtenues après échange topotactique est parfois sans rapport avec les formes allongée des précurseurs. De manière plus précise, une observation au microscope électronique à balayage montre un rôle clé de la température de synthèse: aux basses températures, de nouvelles particules plus petites apparaissent sur la surface des précurseurs et pour des températures plus élevées, ces particules se sont individualisées. Les formes extérieures des particules obtenues sont extrêmement variées, allant des cubes aux sphères en passant par des tores. En examinant au microscope électronique à transmission ces particules individuelles, des informations supplémentaires apparaissent: des particules cubiques peuvent se révéler creuses. Les plans atomiques peuvent également apparaître et confirmer, dans le cas des particules de forme torique, que la structure cristalline n'est pas sous contrainte, et que les plans atomiques ne sont pas concentriques. De nombreux mécanismes peuvent être invoqués pour justifier la plupart des morphologies obtenues. Parmi ceux-ci, le mûrissement d'Ostwald tend à favoriser des particules de forme sphérique et de taille la plus importante possible afin de minimiser la tension de surface. Pour les particules pleines et de forme allongée, l'effet Kirkendall se traduit par une diffusion vers l'extérieur plus rapide du cation sortant que ne l'est la diffusion vers l'intérieur des ions Barium, ce qui se traduit par la formation de lacunes qui, ultimement, se condensent au coeur de la particule allongée pour lui faire adopter une géométrie tubulaire. En revanche, le passage d'un tube constitué d'un agglomérat de particules sphériques à des nanotubes impose l'existence d'un mécanisme de morphogénèse différent. Ce travail propose donc une modélisation de chacun des tubes par un système d'équations de réaction-diffusion.

De nouvelles formes de nanoparticules de matériau ferroélectrique ayant été obtenues, la suite de ce travail a consisté à étudier quelle pouvait être l'organisation de la polarisation en leur sein. Pour tout ensemble de dipôles, il est possible de reproduire exactement la distribution de charges qu'ils représentent avec chacun des coefficients faisant intervenir la somme sur les dipôles du produit entre une composante du moment dipolaire et un nombre arbitraire de coordonnées de la position du dipôle concerné. Des ensembles de combinaisons linéaires de ces types de coefficients

peuvent être formés de sorte que le résultat d'un changement de coordonnées correspondant à une rotation appliqué à un de ces ensembles de coefficients puisse s'exprimer en fonction des valeurs initiales. D'autre part, il a été tenté d'estimer l'influence de la permittivité électronique sur l'expression de l'interaction dipôle-dipôle. Aussi bien dans le cas de conditions limites de type court-circuit que dans le cas de conditions limites de type circuit ouvert, il a été constaté qu'aucune expression ne pouvait plus être obtenue dans le cas général où la permittivité varie spatialement.

Plusieurs simulations minimisant l'énergie totale ont été conduites dans une perovskite appelée le Titanate de Baryum, un des matériaux ferroélectriques les plus étudiés et le produit final obtenu lors des synthèses conduites dans la partie expérimentale. En modifiant les positions atomiques, les coefficients d'un développement perturbatif de l'énergie autour de la structure cubique ont ensuite été extraits et baptisés Hamiltonien effectif. Plus l'énergie minimisée décrit précisément le système électronique, plus les coefficients calculés rendent fidèlement compte des transitions de phase se produisant dans le matériau. En particulier, dans le cas de la modélisation des propriétés de volume du matériau, en abaissant la température il y a successivement passage d'une phase cubique paraélectrique à une phase tetragonale ferroélectrique puis à des phases ferroélectriques rhomboédrique voire orthorhombique, ce qui reproduit exactement les observations expérimentales. Cependant, ces simulations en volume ont pour caractéristique d'utiliser complètement des conditions limites périodiques et de négliger complètement le rôle des surfaces. Comme fait dans la littérature, il est alors possible de conserver les mêmes coefficients pour le Hamiltonien effectif, mais de changer les conditions aux bords. Du point de vue de l'interaction électrostatique, une combinaison linéaire entre les cas type circuit ouvert et circuit fermé est réalisée et, en bordure du matériau, une couche où les paramètres d'ordre locaux représentant la contrainte et le moment dipolaire s'annulent est ajoutée, de manière à supprimer l'effet des conditions limites périodiques au niveau des sites situés en bordure de cellule de simulation. Concernant les simulations numériques proprement dites, le choix fait au cours de ce travail fut de se concentrer sur la simulation de nouvelles formes non étudiées par le passé mais en se restreignant à celles qu'il était effectivement possible d'obtenir au cours de la partie expérimentale de cette thèse: deux types de géométries, à savoir des cubes creux et des tores, seront par conséquent l'objet du reste du manuscrit. Dans ces deux cas, il était nécessaire d'établir une distinction entre les sites modélisant du matériau ferroélectrique et des sites situés ailleurs, qui devaient modéliser un milieu aussi proche que possible du vide. Dans le cadre du cube creux, tous les sites situés dans le cube intérieur, qui devaient donc modéliser une absence de matériau ferroélectrique ont donc été simulés en annulant les paramètres d'ordre locaux représentant la contrainte et le moment dipolaire, exactement comme dans la couche externe de la cellule de simulation. De cette manière, il a été possible d'ajouter des inclusions centrées de taille variable dans une cellule de simulation contenant $15 \times 15 \times 15$ sites dont une couche externe modélisant du vide. Les simulations ont d'abord été conduites dans le cas de conditions limites de type court-circuit puis circuit ouvert. Dans le premier cas, l'état stable à basse température était à chaque fois une phase rhomboédrique, avec

trois composantes de polarisation spontanée devenant non nulles à la même température, et cela quelle que soit la taille de l'inclusion représentant un vide. Avec des conditions limites de type circuit ouvert, l'état stable à basse température était à chaque fois une phase contenant un vortex de polarisation spontanée avec trois composantes du moment toroïdal devenant non nulles à la même température, pour toutes les tailles de l'inclusion représentant un vide. Une étude supplémentaire de la polarisation spontanée et du moment toroïdal a ensuite été conduite pour chaque inclusion possible dans des conditions limites correspondant à une combinaison entre le cas de court-circuit et le cas de circuit ouvert dont les poids respectifs sont déterminés par un coefficient d'écrantage. Il est alors apparu que la transition entre un état stable à basse température de type polarisation homogène et un état stable à basse température de type vortex se faisait de manière adrupte à un coefficient d'écrantage critique dont la valeur dépendait de la taille de l'inclusion.

La modélisation de tores pouvait être envisagée de diverses manières, selon la structure cristalline adoptée par les particules. Une possibilité aurait été d'envisager que les plans atomiques forment des structures concentriques mais la contrainte associée aurait été importante. Par conséquent, une cellule de simulation de forme parallélépipédique a été utilisée et les sites où pouvait apparaître un moment dipolaire sont restés répartis sur une structure de type cubique: au sein de la cellule de simulation certains sites vérifiaient une inégalité et se trouvaient donc situés à l'intérieur du tore tandis que tous les autres sites reprenaient la modélisation des sites vides introduite pour la cavité des cubes creux. De véritables conditions limites de type court-circuit auraient consisté à introduire des charges libres venant compenser le champ dû aux charges liées en surface du tore alors que l'expression de l'interaction dipôle-dipôle calculée correspond à une compensation en surface du parallélépipède: par conséquent, seules des conditions de type circuit ouvert ont été simulées dans cette partie. D'autre part, à nombre de sites ferroélectriques constant, un tore est caractérisé par le rapport entre son petit rayon et son grand rayon. Lorsque ce rapport est très faible, l'état stable à basse température est un vortex orienté selon l'axe de révolution du tore. Pour des valeurs nettement plus importante du même rapport, proches de l'unité, on observe une coexistence d'un vortex avec une polarisation suivant une direction poloïdale, pouvant se trouver décrite par un autre paramètre appelé moment hypertoroïdal. Dans une situation intermédiaire entre les deux cas précédents, on observe une valeur moyenne nulle de ce moment hypertoroïdal, qui est causée par des oscillations de ce paramètre le long de la direction azimutale.

En conclusion, des nanoparticules de Titanate de Baryum possédant une grande variété de formes ont été produites par une voie solvothermale et les mécanismes y conduisant ont été étudiés. Parmi ces formes, les cubes creux et les nanotores représentaient des géométries peu étudiées dans les simulations de matériaux ferroélectriques. Pour les cubes creux, une étude complète de l'effet du coefficient d'écrantage pour des cubes possédant une cavité de taille croissante a été conduite tandis que, pour les nanotores, à coefficient d'écrantage constamment nul et volume de matériau ferroélectrique constant, une étude de l'influence du rapport entre petit rayon et grand rayon du tore sur la phase stable à basse température a été conduite.

Bibliography

- [1] W. Eerenstein, N. D. Mathur, and J. F. Scott. "Multiferroic and magnetoelectric materials". In: *Nature* 442.7104 (Aug. 2006), pp. 759–765. ISSN: 0028-0836, 1476-4687.
- [2] Ivan I. Naumov, L. Bellaiche, and Huaxiang Fu. "Unusual phase transitions in ferroelectric nanodisks and nanorods". In: *Nature* 432.7018 (Dec. 2004), pp. 737–740. ISSN: 0028-0836, 1476-4679.
- [3] Hellmut J. Juretschke. *Crystal physics: macroscopic physics of anisotropic solids*. anglais. aReading, Mass., Etats-Unis d'Amérique, Royaume-Uni de Grande-Bretagne et d'Irlande du Nord, Pays-Bas, 1974. ISBN: 978-0-8053-5102-6.
- [4] W. D Kingery et al., eds. *High technology ceramics: past, present, and future : the nature of innovation and change in ceramic technology*. English. OCLC: 15016691. Westerville, OH: American Ceramic Society, 1986. ISBN: 978-0-916094-88-1.
- [5] John Frederick Nye. *Propriétés physiques des cristaux: leur représentation par des tenseurs et des matrices*. French. Paris: Dunod, 1961.
- [6] Shan Lin et al. "Size effect on the dielectric properties of BaTiO_3 nanoceramics in a modified Ginsburg-Landau-Devonshire thermodynamic theory". In: *Physical Review B* 74.13 (Oct. 2006), p. 134115.
- [7] W. Zhong, David Vanderbilt, and K. M. Rabe. "First-principles theory of ferroelectric phase transitions for perovskites: The case of BaTiO_3 ". en. In: *Physical Review B* 52.9 (Sept. 1995), pp. 6301–6312. ISSN: 0163-1829, 1095-3795.
- [8] P. Hohenberg and W. Kohn. "Inhomogeneous Electron Gas". In: *Physical Review* 136.3B (Nov. 1964), B864–B871.
- [9] W. Kohn and L. J. Sham. "Self-Consistent Equations Including Exchange and Correlation Effects". In: *Physical Review* 140.4A (Nov. 1965), A1133–A1138.
- [10] Philippe Ghosez and Javier Junquera. "First-Principles Modeling of Ferroelectric Oxide Nanostructures". In: *arXiv:cond-mat/0605299* (May 2006). arXiv: cond-mat/0605299.
- [11] Nicholas Metropolis et al. "Equation of State Calculations by Fast Computing Machines". In: *The Journal of Chemical Physics* 21.6 (June 1953), pp. 1087–1092. ISSN: 0021-9606, 1089-7690.
- [12] S. Prosandeev et al. "Original properties of dipole vortices in zero-dimensional ferroelectrics". en. In: *Journal of Physics: Condensed Matter* 20.19 (2008), p. 193201. ISSN: 0953-8984.
- [13] Mark J. Polking et al. "Ferroelectric order in individual nanometre-scale crystals". In: *Nature Materials* 11.8 (July 2012), pp. 700–709. ISSN: 1476-1122, 1476-4660.

- [14] Lydie Louis. "Multiscale Study of Barium Titanate Nanostructures and Nanocomposites". In: *Ph.D. Thesis* (2013). ISSN: 9781303254369.
- [15] Mickaël Anoufa. "Nanocomposites et effet de dimensionnalité pour le stockage de l'énergie". fr. PhD thesis. Ecole Centrale Paris, Dec. 2012.
- [16] Charles Kittel. "Theory of the Structure of Ferromagnetic Domains in Films and Small Particles". en. In: *Physical Review* 70.11-12 (Dec. 1946), pp. 965–971. ISSN: 0031-899X.
- [17] Bas B. Van Aken et al. "Observation of ferrotoroidic domains". In: *Nature* 449.7163 (Oct. 2007), pp. 702–705. ISSN: 0028-0836, 1476-4687.
- [18] A. Wachowiak. "Direct Observation of Internal Spin Structure of Magnetic Vortex Cores". In: *Science* 298.5593 (Oct. 2002), pp. 577–580. ISSN: 00368075, 10959203.
- [19] T. Shinjo. "Magnetic Vortex Core Observation in Circular Dots of Permalloy". In: *Science* 289.5481 (Aug. 2000), pp. 930–932. ISSN: 00368075, 10959203.
- [20] Kyoichi Kinoshita. "Grain-size effects on dielectric properties in barium titanate ceramics". en. In: *Journal of Applied Physics* 47.1 (1976), p. 371. ISSN: 00218979.
- [21] A. K. Yadav et al. "Observation of polar vortices in oxide superlattices". en. In: *Nature* 530.7589 (Feb. 2016), pp. 198–201. ISSN: 0028-0836.
- [22] M. Anoufa et al. "Vortices of polarization in BaTiO₃ core-shell nanoceramics: Calculations based on *ab initio* derived Hamiltonian versus Landau theory". en. In: *Physical Review B* 88.14 (Oct. 2013). ISSN: 1098-0121, 1550-235X.
- [23] S. Prosandeev and L. Bellaïche. "Hypertoroidal moment in complex dipolar structures". en. In: *Journal of Materials Science* 44.19 (Apr. 2009), pp. 5235–5248. ISSN: 0022-2461, 1573-4803.
- [24] Albert Fert, Vincent Cros, and João Sampaio. "Skyrmions on the track". en. In: *Nature Nanotechnology* 8.3 (Mar. 2013), pp. 152–156. ISSN: 1748-3387.
- [25] J. F. Scott. "Applications of Modern Ferroelectrics". en. In: *Science* 315.5814 (Feb. 2007), pp. 954–959. ISSN: 0036-8075, 1095-9203.
- [26] Y. Nahas et al. "Discovery of stable skyrmionic state in ferroelectric nanocomposites". en. In: *Nature Communications* 6 (Oct. 2015), p. 8542.
- [27] M. Anoufa et al. "Energy harvesting in core-shell ferroelectric ceramics: Theoretical approach and practical conclusions". en. In: *Journal of Applied Physics* 113.5 (2013), p. 054104. ISSN: 00218979.
- [28] J. M. Kiat et al. "Low-symmetry phases and loss of relaxation in nanosized lead scandium niobate". In: *Physical Review B* 81.14 (Apr. 2010), p. 144122.
- [29] S. Prosandeev and L. Bellaïche. "Controlling Double Vortex States in Low-Dimensional Dipolar Systems". In: *Physical Review Letters* 101.9 (Aug. 2008), p. 097203.

- [30] Gentien Thorner et al. "Axial hypertoroidal moment in a ferroelectric nanotorus: A way to switch local polarization". en. In: *Physical Review B* 89.22 (June 2014). ISSN: 1098-0121, 1550-235X.
- [31] S. Prosandeev et al. "Control of Vortices by Homogeneous Fields in Asymmetric Ferroelectric and Ferromagnetic Rings". en. In: *Physical Review Letters* 100.4 (Jan. 2008). ISSN: 0031-9007, 1079-7114.
- [32] Christine Bogicevic et al. "Morphogenesis mechanisms in the solvothermal synthesis of BaTiO₃ from titanate nanorods and nanotubes". en. In: *Nanoscale* 7.8 (2015), pp. 3594–3603. ISSN: 2040-3364, 2040-3372.
- [33] C. Bogicevic et al. "Synthesis of Nanometric Cubic BaTiO₃ by Using an Original Chemical Route: Freeze-Drying Method". In: *Ferroelectrics* 270.1 (Jan. 2002), pp. 57–62. ISSN: 0015-0193.
- [34] J. M. Kiat et al. "Structural investigation of strontium titanate nanoparticles and the core-shell model". In: *Physical Review B* 87.2 (Jan. 2013), p. 024106.
- [35] Deena R. Modeshia and Richard I. Walton. "Solvothermal synthesis of perovskites and pyrochlores: crystallisation of functional oxides under mild conditions". en. In: *Chemical Society Reviews* 39.11 (2010), p. 4303. ISSN: 0306-0012, 1460-4744.
- [36] C. B. Ponton. *Third Euro-Ceramics; Volume 1: Processing of Ceramics*. First Edition edition. Faenza Editrice Iberica, 1993. ISBN: 978-84-87683-06-0.
- [37] Richard I. Walton. "Subcritical solvothermal synthesis of condensed inorganic materials". en. In: *Chemical Society Reviews* 31.4 (June 2002), pp. 230–238. ISSN: 1460-4744.
- [38] Ningzhong Bao et al. "Shape-Controlled Monocrystalline Ferroelectric Barium Titanate Nanostructures: From Nanotubes and Nanowires to Ordered Nanostructures". In: *The Journal of Physical Chemistry C* 112.23 (June 2008), pp. 8634–8642. ISSN: 1932-7447.
- [39] Jie Yang et al. "Stick-like titania precursor route to MTiO₃ (M = Sr, Ba, and Ca) polyhedra". en. In: *CrystEngComm* 14.8 (Mar. 2012), pp. 2959–2965. ISSN: 1466-8033.
- [40] P. C. Kesavan, G. J. Sharma, and S. M. J. Afzal. "Differential Modification of Oxidic and Anoxic Radiation Damage by Chemicals: I. Simulation of the Action of Caffeine by Certain Inorganic Radical Scavengers". In: *Radiation Research* 75.1 (1978), pp. 18–30. ISSN: 0033-7587.
- [41] Ningzhong Bao et al. "Size-controlled one-dimensional monocrystalline BaTiO₃ nanostructures". en. In: *Applied Physics Letters* 94.25 (2009), p. 253109. ISSN: 00036951.
- [42] Qi Feng, Manabu Hirasawa, and Kazumichi Yanagisawa. "Synthesis of Crystal-Axis-Oriented BaTiO₃ and Anatase Plate-like Particles by a Hydrothermal Soft Chemical Process". In: *Chemistry of Materials* 13.2 (Feb. 2001), pp. 290–296. ISSN: 0897-4756.
- [43] Andrea Lamberti et al. "Synthesis of ferroelectric BaTiO₃ tube-like arrays by hydrothermal conversion of a vertically aligned TiO₂ nanotube carpet". en. In: *New Journal of Chemistry* 38.5 (Apr. 2014), pp. 2024–2030. ISSN: 1369-9261.

- [44] Aneesh Koka et al. "Controlled synthesis of ultra-long vertically aligned BaTiO₃ nanowire arrays for sensing and energy harvesting applications". en. In: *Nanotechnology* 25.37 (2014), p. 375603. ISSN: 0957-4484.
- [45] Er-Wei Shi et al. "Crystallographic Properties of Hydrothermal Barium Titanate Crystallites". en. In: *Journal of the American Ceramic Society* 80.6 (Jan. 2005), pp. 1567–1572. ISSN: 00027820, 15512916.
- [46] W. Ostwald. "Studien Äijber die Bildung und Umwandlung fester KÄúrper". In: *Zeitschrift fÄijr Physikalische Chemie* (1897), pp. 289–330.
- [47] A. D. Smigelskas and E. O. Kirkendall. "Zinc Diffusion in Alpha Brass". In: *Trans. AIME* (1947), pp. 130–142.
- [48] Qiao Zhang et al. "Self-templated synthesis of hollow nanostructures". In: *Nano Today* 4.6 (Dec. 2009), pp. 494–507. ISSN: 1748-0132.
- [49] S. Ding et al. "Formation of tubular BaTiO₃ nanoparticle assembly through the Kirkendall effect using Na₂Ti₃O₇ nanowires as template". In: *Materials Research Bulletin* 48.11 (Nov. 2013), pp. 4565–4569. ISSN: 0025-5408.
- [50] Yadong Yin et al. "Formation of Hollow Nanocrystals Through the Nanoscale Kirkendall Effect". en. In: *Science* 304.5671 (Apr. 2004), pp. 711–714. ISSN: 0036-8075, 1095-9203.
- [51] Ming Huang et al. "Merging of Kirkendall Growth and Ostwald Ripening: CuO@MnO₂ Core-shell Architectures for Asymmetric Supercapacitors". In: *Scientific Reports* 4 (Mar. 2014). ISSN: 2045-2322.
- [52] Hong Jin Fan, Ulrich GÄúsele, and Margit Zacharias. "Formation of Nanotubes and Hollow Nanoparticles Based on Kirkendall and Diffusion Processes: A Review". en. In: *Small* 3.10 (Oct. 2007), pp. 1660–1671. ISSN: 1613-6829.
- [53] A. Habib, R. Haubner, and N. Stelzer. "Effect of temperature, time and particle size of Ti precursor on hydrothermal synthesis of barium titanate". In: *Materials Science and Engineering: B. 4th International Workshop on Nanosciences and Nanotechnologies (NN07)* 152.1ÄŒ3 (Aug. 2008), pp. 60–65. ISSN: 0921-5107.
- [54] Zhao Deng et al. "Synthesis and Characterization of Bowl-Like Single-Crystalline BaTiO₃ Nanoparticles". en. In: *Nanoscale Research Letters* 5.7 (May 2010), p. 1217. ISSN: 1556-276X.
- [55] Feng Xia et al. "Microwave absorption enhancement and electron microscopy characterization of BaTiO₃ nano-torus". en. In: *Nanoscale* 3.9 (Sept. 2011), pp. 3860–3867. ISSN: 2040-3372.
- [56] Meng-Fang Lin et al. "Dopant induced hollow BaTiO₃ nanostructures for application in high performance capacitors". en. In: *Journal of Materials Chemistry* 21.41 (Oct. 2011), pp. 16500–16504. ISSN: 1364-5501.
- [57] Xin Yang et al. "Monodisperse hollow perovskite BaTiO₃ nanostructures prepared by a solÄŒgelÄŒhydrothermal method". In: *Ceramics International* 40.7, Part A (Aug. 2014), pp. 9663–9670. ISSN: 0272-8842.

- [58] Florentina Maxim et al. "Barium Titanate Torus-Like Particles: Low-Temperature Synthesis and Formation Mechanism". en. In: *European Journal of Inorganic Chemistry* 2014.30 (Oct. 2014), pp. 5160–5167. ISSN: 1099-0682.
- [59] Wenjun Dong et al. "General Approach to Well-Defined Perovskite MTiO_3 (M = Ba, Sr, Ca, and Mg) Nanostructures". In: *The Journal of Physical Chemistry C* 115.10 (Mar. 2011), pp. 3918–3925. ISSN: 1932-7447.
- [60] A. M. Turing. "The Chemical Basis of Morphogenesis". en. In: *Philosophical Transactions of the Royal Society of London B: Biological Sciences* 237.641 (Aug. 1952), pp. 37–72. ISSN: 0962-8436, 1471-2970.
- [61] J. D. Murray. *Mathematical biology*. English. Berlin ; New York: Springer-Verlag, 1989. ISBN: 978-0-387-19460-8.
- [62] Shigeru Kondo and Takashi Miura. "Reaction-Diffusion Model as a Framework for Understanding Biological Pattern Formation". en. In: *Science* 329.5999 (Sept. 2010), pp. 1616–1620. ISSN: 0036-8075, 1095-9203.
- [63] Wuzong Zhou. "Reversed Crystal Growth: Implications for Crystal Engineering". en. In: *Advanced Materials* 22.28 (Apr. 2010), pp. 3086–3092. ISSN: 09359648, 15214095.
- [64] Xianfeng Yang et al. "Formation Mechanism of CaTiO_3 Hollow Crystals with Different Microstructures". In: *Journal of the American Chemical Society* 132.40 (Oct. 2010), pp. 14279–14287. ISSN: 0002-7863.
- [65] V.M. Dubovik and V.V. Tugushev. "Toroid moments in electrodynamics and solid-state physics". en. In: *Physics Reports* 187.4 (Mar. 1990), pp. 145–202. ISSN: 03701573.
- [66] Ia. B. Zel'Dovich. "Electromagnetic Interaction with Parity Violation". In: *Soviet Journal of Experimental and Theoretical Physics* 6 (1958), p. 1184. ISSN: 1063-7761.
- [67] Julius Adams Stratton. *Electromagnetic Theory*. en. John Wiley & Sons, Jan. 2007. ISBN: 978-0-470-13153-4.
- [68] J C TolÁ'dano and P TolÁ'dano. *The Landau Theory of Phase Transitions: Application to Structural, Incommensurate, Magnetic and Liquid Crystal Systems*. en. Vol. 3. World Scientific Lecture Notes in Physics. WORLD SCIENTIFIC, Aug. 1987. ISBN: 978-9971-5-0025-2 978-981-279-939-5.
- [69] Laura Walizer, Sergey Lisenkov, and L. Bellaiche. "Finite-temperature properties of $(\text{Ba}, \text{Mg})\text{TiO}_3$ systems from atomistic simulations". In: *Physical Review B* 73.14 (Apr. 2006), p. 144105.
- [70] Jorge Áñíguez and David Vanderbilt. "First-Principles Study of the Temperature-Pressure Phase Diagram of $\text{B}\text{a}\text{T}\text{i}\text{O}_3$ ". In: *Physical Review Letters* 89.11 (Aug. 2002), p. 115503.
- [71] S. Bin-Omran. "Phase-transition character in $(\text{Ba}_{0.50}\text{Sr}_{0.50})\text{TiO}_3$ nanodots from first principles". In: *Journal of Alloys and Compounds* 674 (July 2016), pp. 82–88. ISSN: 0925-8388.

- [72] L. Louis et al. "Low-Symmetry Phases in Ferroelectric Nanowires". In: *Nano Letters* 10.4 (Apr. 2010), pp. 1177–1183. ISSN: 1530-6984.
- [73] Lydie Louis et al. "Novel complex phenomena in ferroelectric nanocomposites". en. In: *Journal of Physics: Condensed Matter* 24.40 (2012), p. 402201. ISSN: 0953-8984.
- [74] Bo-Kuai Lai et al. "Domain evolution of Ba Ti O 3 ultrathin films under an electric field: A first-principles study". en. In: *Physical Review B* 75.8 (Feb. 2007). ISSN: 1098-0121, 1550-235X.
- [75] Ivan Naumov and Alexander M. Bratkovsky. "Unusual Polarization Patterns in Flat Epitaxial Ferroelectric Nanoparticles". en. In: *Physical Review Letters* 101.10 (Sept. 2008). ISSN: 0031-9007, 1079-7114.
- [76] M. G. Stachiotti and M. Sepiarsky. "Toroidal Ferroelectricity in PbTiO 3 Nanoparticles". en. In: *Physical Review Letters* 106.13 (Mar. 2011). ISSN: 0031-9007, 1079-7114.
- [77] N. D. Mermin. "The topological theory of defects in ordered media". en. In: *Reviews of Modern Physics* 51.3 (July 1979), pp. 591–648. ISSN: 0034-6861.
- [78] D. Byrne et al. "Ordered arrays of lead zirconium titanate nanorings". en. In: *Nanotechnology* 19.16 (2008), p. 165608. ISSN: 0957-4484.
- [79] S. Prosandeev and L. Bellaiche. "Characteristics and signatures of dipole vortices in ferroelectric nanodots: First-principles-based simulations and analytical expressions". In: *Physical Review B* 75.9 (Mar. 2007), p. 094102.
- [80] I. Hasegawa, Y. Sakaniwa, and H. Shima. "Novel scaling behavior of the Ising model on curved surfaces". In: *Surface Science. Proceedings of the 10th ISSP International Symposium on Nanoscience at Surfaces* 601.22 (Nov. 2007), pp. 5232–5236. ISSN: 0039-6028.
- [81] S. Zhang et al. "Formation Mechanism of $\text{H}_2\text{T}_i\text{O}_3$ Nanotubes". In: *Physical Review Letters* 91.25 (Dec. 2003), p. 256103.
- [82] Huaxiang Fu and L. Bellaiche. "Ferroelectricity in Barium Titanate Quantum Dots and Wires". en. In: *Physical Review Letters* 91.25 (Dec. 2003). ISSN: 0031-9007, 1079-7114.
- [83] S. Prosandeev and L. Bellaiche. "Order parameter in complex dipolar structures: Microscopic modeling". In: *Physical Review B* 77.6 (Feb. 2008), p. 060101.
- [84] A. A. Gorbatsevich and Yu. V. Kopaev. "Toroidal order in crystals". en. In: *Ferroelectrics* 161.1 (Nov. 1994), pp. 321–334. ISSN: 0015-0193, 1563-5112.
- [85] J. F. Scott. "Ferroelectrics: Novel geometric ordering of ferroelectricity". In: *Nature Materials* 4.1 (Jan. 2005), pp. 13–14. ISSN: 1476-1122, 1476-4660.
- [86] X. H. Zhu et al. "Perovskite lead zirconium titanate nanorings: Towards nanoscale ferroelectric solenoids?" In: *Applied Physics Letters* 89.12 (Sept. 2006), p. 122913. ISSN: 0003-6951, 1077-3118.

-
- [87] Sergey Prosandeev et al. "Natural optical activity and its control by electric field in electro-toroidic systems". In: *Physical Review B* 87.19 (May 2013), p. 195111.

Titre : NANOSTRUCTURES DE TITANATE DE BARYUM : modélisation, simulations numériques et étude expérimentale

Mots clés : Titanate de Baryum, nanostructures, simulations

Résumé : Des simulations numériques conduites sur un ferroélectrique, le Titanate de Baryum, permettent d'extraire les températures où se produisent les transitions pour chacune des composantes et elles utilisent le plus souvent des conditions limites périodiques. Cependant, il est possible de modifier la simulation de manière à rendre compte d'une particule isolée, et les conditions limites électriques de type court-circuit ou bien circuit ouvert affectent alors le résultat. Réduire la taille accorde encore davantage d'importance à de tels effets de surface par rapport aux effets de volume. Expérimentalement, la formation de nanocubes creux ou de nanotubes a été observée lors de synthèses solvothermales. De possibles mécanismes de morphogénèse sont évoqués.

Dans ce travail, les simulations ont ensuite été conduites sur des particules nanométriques, dont les formes avaient été obtenues expérimentalement. Pour des cubes creux, il a été constaté que la taille de l'inclusion vide modifiait la valeur du coefficient d'écrantage critique à partir duquel le comportement de la polarisation passe d'une configuration de type court-circuit à une configuration de type circuit fermé. Pour des nanotubes aux basses températures, une modification du rapport entre petit et grand rayon donne lieu à des configurations possédant un moment toroïdal seul ou accompagné d'un moment hypertoroïdal voire d'oscillations de ce dernier.

Title : BARIUM TITANATE NANOSTRUCTURES : modeling, numerical simulations and experiments

Keywords : Barium Titanate, nanostructures, simulations

Abstract : Numerical simulations performed on a ferroelectric, Barium Titanate, yield all the transition temperatures under periodic boundary conditions. However, the same simulation can be modified to model an isolated particle under short-circuit or open-circuit electrical boundary conditions. Reducing size makes these surface effects even more important with regard to volume effects. From an experimental point of view, solvothermal synthesis of hollow nanocubes and nanotubes is reported and various morphogenesis mechanisms are listed.

In this work, simulations were performed on nanometric particles that had experimentally obtained shapes. In hollow cubes, it was shown that the hole size changed the numerical value of the critical screening coefficient at which the system changes its behavior from a configuration that is short-circuit like to another one that is open-circuit like. For nanotubes at low temperatures, a modification of the ratio between torus minor and major radius gives either configurations with only toroidal moment or configurations in which it coexists with homogeneous or oscillating hypertoroïdal moment.

